A COMPUTATIONAL STUDY OF MICROWAVE-INDUCED THERMO-ACOUSTIC TOMOGRAPHY BY TIME-DOMAIN FINITE ELEMENT METHOD

By

PONLAKIT JARIYATANTIWAIT

Bachelor of Engineering in Telecommunication Engineering
King Mongkut Institute of Technology Ladkrabang
Bangkok, Thailand
1998

Master of Engineering in Electrical Engineering
King Mongkut University of Technology Thonburi
Bangkok, Thailand
2000

Submitted to the Faculty of the
Graduate College of
Oklahoma State University
in partial fulfillment of
the requirements for
the Degree of
DOCTOR OF PHILOSOPHY
July, 2015

A COMPUTATIONAL STUDY OF MICROWAVE-INDUCED THERMO-ACOUSTIC TOMOGRAPHY BY TIME-DOMAIN FINITE ELEMENT METHOD

Dissertation Approved:

Dr.Charles F. Bunting

Dissertation Advisor

Dr.James C. West

Dr.Keith A. Teague

Dr.Paul Weckler

ACKNOWLEDGEMENTS

First of all, I would like to take this opportunity to express my appreciation and to gratefully thank my dissertation adviser Dr.Charles Bunting for his guidance, mentorship, and invaluable help throughout this work. His dedication has helped me stay on track with this research. His vision and experience has helped in refining my attitude toward this research and in future works. Without his help, I could never have come this far. I can truly say that I am indebted to him forever.

I would like to thank Dr.James West for his valuable suggestions in the field of radar and electromagnetics. I would like to thank Dr.Keith Teaque for his comments and guidance. I am also grateful to Dr.Paul Weckler for his valuable comments. I would like to thank Dr.Daqing Piao for all the valuable suggestions in the field of biomedical engineering that helped me understand the concepts of thermo-acoustic tomography and the guidance on excitation pulse waveforms for thermo-acoustic application. I am also grateful to Dr.Sovanlal Mukherjee, Dr.Vignesh Rajamani, and Rahul Bakore for discussions during this research.

Last but not least, I would like to thank my parent and my parent-in-law who always encourage and support me everyday in every way. I also thank my elder brother, brother-in-law, sister-in-law who take care of everything for me at Thailand during my graduate work here. I would like to thanks my wife and my daughter for their love and patience. I also would like to thank the ministry of science and technology, Royal Thai Government for all the supports during this study.

Acknowledgements reflect the views of the author and are not endorsed by committee members or Oklahoma State University.

Name: PONLAKIT JARIYATANTIWAIT

Date of Degree: July, 2015

Title of Study: A COMPUTATIONAL STUDY OF MICROWAVE-INDUCED THERMO-ACOUSTIC TOMOGRAPHY BY TIME-DOMAIN FINITE ELEMENT METHOD

Major Field: ELECTRICAL ENGINEERING

Abstract: This work presents a time-domain finite element method (TDFEM) for simulation of thermo-acoustic (TA) signal generation in biological tissue for the application of microwave-induced thermo-acoustic tomography (MITAT). This time-domain numerical technique is useful in the analysis of time-varying electric and pressure field generation while a non-conventional microwave pulse excitation in non-homogeneous medium of complex biological tissue structure is applied in this application. In this work, an intensity-modulated chirp pulse at microwave frequency is first applied as an alternative microwave pulse excitation for MITAT. The results of applying the modulated chirp pulse show that the peak-power of microwave pulse can be reduced compared with that of using the conventional modulated Gaussian pulse excitation. In this work, two configurations of acoustic detector array for TA signal detection are considered: concave and convex array, which is a suitable configuration for the application of breast cancer and prostate cancer detection, respectively. The detected TA signal by the array of acoustic detector is processed using a cross-correlation detection in which the propagation (delay) time characteristic of captured TA signal is extracted. This delay time characteristic carries information of the electromagnetic absorption distribution of the tissue in which the back-projection is applied for an image reconstruction. The numerical results of induced TA signal from conventional and modulated chirp pulse are shown. The reconstructed images are compared on the different cases of microwave pulses, detector arrays, tissue properties and geometries.

TABLE OF CONTENTS

LIST OF TABLES

LIST OF FIGURES

CHAPTER 1

INTRODUCTION

1.1 The Important of Medical Imaging

Cancer remains a leading cause of death worldwide. The number of incidents and mortality of cancer diseases in 2012 are approximately 14.1 million and 8.2 million cases, respectively, as reported in 2014 by International Agency for Research on Cancer (IARC), World Health Organization (WHO) [1]. Moreover, the number of new cases of cancer is expected to increase by 75% [1] over the next 2 decades which will bring it close to 25 million by 2034. Within the numbers of incidents and mortality of cancers in 2012, the five most common sites of cancer found in men were: lung 16.7%; prostate 15.0%; colorectum 10%; stomach 8.5%; liver 7.5%, while the five most common sites of cancer in women were: breast 25.2%; colorectum 9.2%; lung 8.7%; cervix 7.9%; stomach 4.8% [2] which can be presented in Figure 1.1.

Many efforts have been made on the diagnosis and treatment of cancer. The major techniques that are generally used in treatment of cancers include surgery, chemotherapy, and radiation therapy, however, treatment in early stages are key to achieving high successful cure rates.

A technology that can help physicians in visualizing the internal structures of human bodies for the diagnosis of diseases without penetration of the body is medical imaging technology. The field of medical imaging is undergoing significant devel-

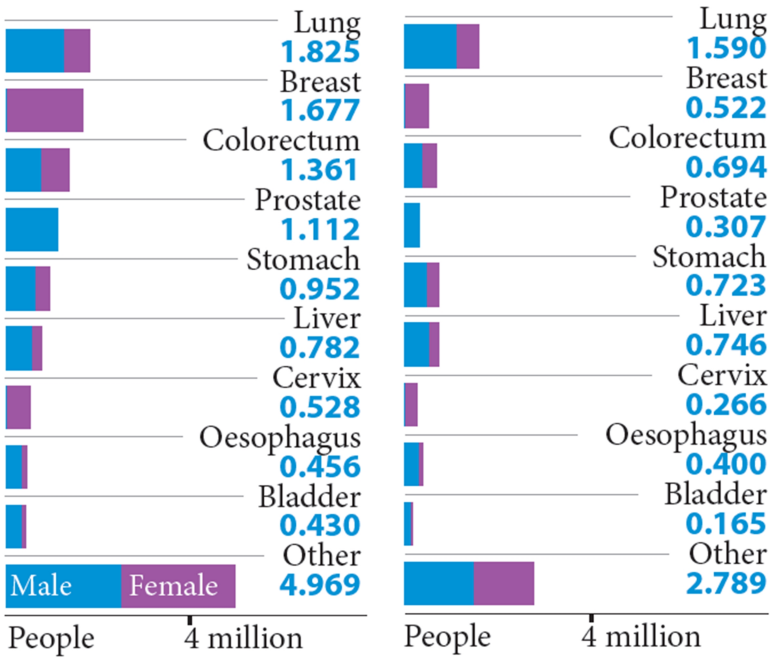

Figure 1.1: World incidence and mortality of cancers in difference locations of men and women in 2012 [2], (a) incidence cases, (b) mortality cases.

opment and still an area of active research. The advancement in medical imaging technologies [3, 4] such as ultrasonic imaging (UI or ultrasonography), X-Ray computed tomography (CT) scan, magnetic resonance imaging (MRI), positron emission tomography (PET) have enhanced doctors' abilities to see internal structures of human body in order to diagnose patients non-invasively. This technology can increase confidence of diagnoses and reduce a number of surgeries to patients. Other medical imaging modalities include microwave imaging (MI) [5], diffuse optical tomography (DOT) [6], thermo-acoustic tomography (TAT) [7] have been emerging and seen increasing attention as alternative medical imaging tools. From a survey of medical imaging modality, a comparison of various non-invasive medical imaging modalities on resolution, contrast, processing time, ionizing radiation and cost can be shown in Table 1.1.

Table 1.1: Qualitative characteristics of non-invasive medical imaging modalities.

Medical Imaging Modalities	Characteristics				
	Image Resolution	Image Contrast	Processing Time	Ionizing Radiation	Cost
MRI	High	High	Slow	No	High
X-RAY CT	Medium	Medium	Medium	Yes	Medium
PET	High	High	Medium	Yes	High
UI	High	Low	Fast	No	Low
MI	Low	High	Fast	No	Low
DOT	Low	High	Fast	No	Low
TAT	High	High	Fast	No	Low

1.2 Overview of Thermo-Acoustic Tomography

The qualitative characteristics of medical imaging modalities presented in Table 1.1 shows that TAT has the attractive characteristics of high image resolution, high contrast ratio, non-ionizing radiation, fast processing time, and low cost. These attractive characteristics have led to a number of studies and research by several research groups. This section describes an overview of TAT with the forward step of TA signal generation in biological tissue and the inverse step of acoustic signal detection and image reconstruction to form the TAT imaging modality.

1.2.1 Basic operation of thermo-acoustic tomography

TAT is a novel hybrid medical imaging modality that takes advantage of thermal and acoustic energy conversion termed the thermo-acoustic effect. This imaging technique has been applied for non-invasive biological tissue imaging *in vivo*. TAT modality can be divided into two steps: forward and inverse step. In the forward step, a very short

pulse of electromagnetic (EM) field is applied to deliver EM energy into an imaging domain which is normally a biological tissue. This electromagnetic pulse is normally a narrow-width pulse in order to achieve high resolution of reconstructed image. A portion of the EM field is absorbed by the biological tissue and the local absorption of the EM field generates thermal energy inside the tissue as a result of Joule heating effect. After the tissue gets heated up as a process of thermal energy conversion, a pressure field is then generated as a consequence of thermo-elastic expansion. This generated pressure field will propagate outwardly from the local heat sources and it is normally called the thermo-acoustic (TA) signal, or more generally, acoustic signal.

In the inverse step, scanning of a single acoustic detector or an array of acoustic detector will be applied for capturing this generated TA signal along the external boundary of the imaging domain for an image reconstruction. This reconstructed image represents the local absorption distribution properties of the imaging domain.

Generally, there are two regions of EM spectrum that have been applied in the TAT system. The first one is near-infrared (NIR) or visible laser light which leads to photo-acoustic tomography (PAT) [8]. Another region is radio frequency (RF), usually microwave frequency, which can be termed microwave-induced thermo-acoustic tomography (MITAT) [9]. The penetration depth in tissue using RF band illumination into the tissue is deeper than that of using the visible light band, and then MITAT has clearly more imaging depth than PAT.

The major advantages of this novel hybridized imaging modality is that its reconstructed image has both high contrast as a result of EM absorption and high resolution as a result of ultrasonic wavelength inside biological tissues. It also does not expose patients to ionizing radiation.

1.2.2 Biological tissue modeling

As the generation of TA signals in a biological tissue described in Subsection 1.2.1, the absorption of EM field and the thermo-elastic properties of the biological tissue contribute in the generation of TA signal. This subsection presents a model of biological tissue for TA signal generation in which the model combines the dielectric and acoustic properties of tissue and can be shown in Figure 1.2(a). A diagram of TA signal generation on the tissue model can be depicted in Figure 1.2(b). The operation of thermo-acoustic signal generation and its image reconstruction in forming an MITAT will be described in detail in Chapter 2.

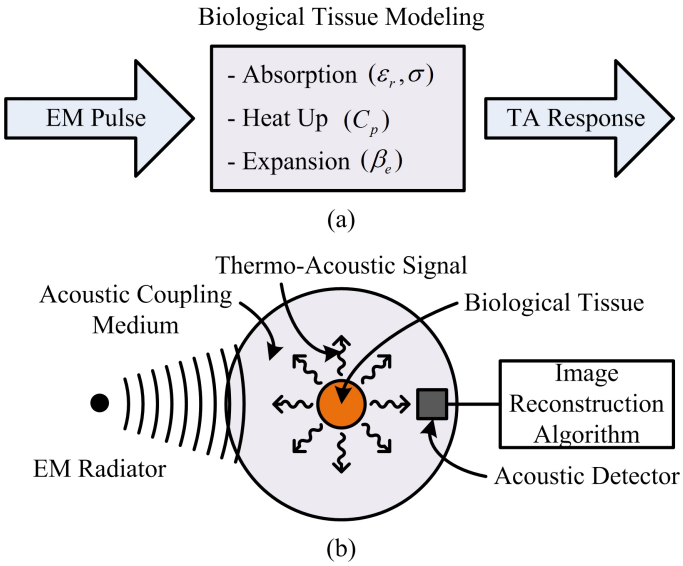

Figure 1.2: Concept of thermo-acoustic signal generation for biological tissue: (a) Biological tissue model, (b) TA signal generation diagram.

1.2.3 Configuration of detector array

The configuration of detector arrays for acoustic scanning for receiving TA signal in TAT can be categorized into two different configurations which can be shown in Figure 1.3. The first one is a concave detection array which is normally applied for breast or brain imaging [10, 7, 11, 12, 13]. The second one is a convex detection array

[14] which is along an internal boundary inside the imaging domain. The convex detection array is a candidate for a prostate or trans-rectal imaging applicator.

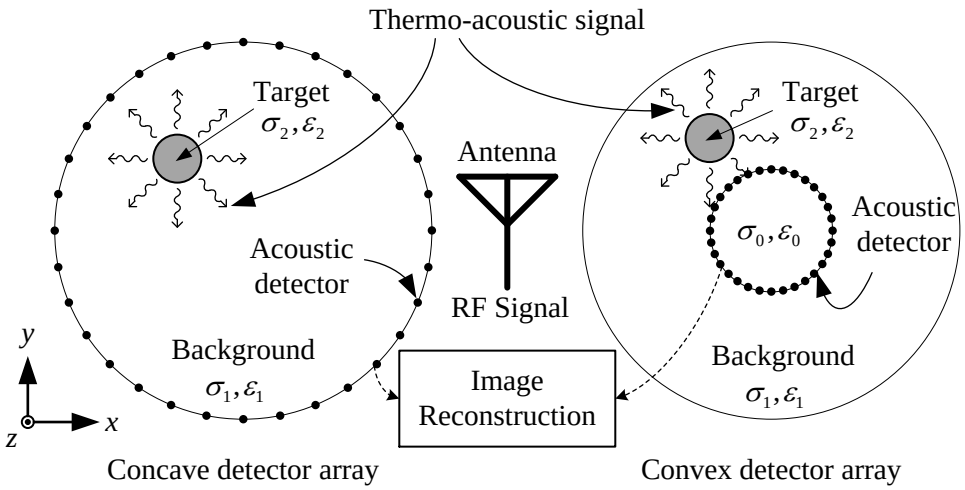

Figure 1.3: Thermo-acoustic tomography with concave and convex detector array geometry.

Because of the difference in dielectric properties between normal and malignant human tissues as reported in [15, 16] in which the electrical conductivity of malignant tissues is higher than that of healthy tissues, TAT shows a feasibility to detect and distinguish malignant tissues from healthy tissues. Resent research indicates that TAT has its ability to detect cancer in early stage [17, 18, 19, 20]. It also can image various parts of body such as breast [20, 21], brain [22, 23], prostate (trans-rectal geometry) [14, 24], or even a whole body of small animal [25, 26]. Briefly, TAT reveals internal structures of human or animal body non-invasively based on the difference in EM absorption properties of biological tissues.

1.3 Review of Literatures

The thermo-acoustic effect and its application for thermo-acoustic imaging have been discovered and developed over a long time. In 1880, Alexander Graham Bell discovered the thermo-acoustic effect. He found that an audible acoustic wave can be

produced on a thin disk of rubber when it was exposed to mechanically chopped light [27]. Almost a century later, J. C. Lin [28] reported that auditory activities can be evoked by irradiating the head of laboratory animals and human with pulsed microwave. In 1981, T. Bowen [29] reported a generation of thermo-acoustic signal by electromagnetic illumination in soft tissue and indicated the feasibility of thermo-acoustic imaging of soft tissue. An experiment on thermo-acoustic imaging of tissue phantom was also reported by Bowen *et al.* [30].

In 1987, R. Pethig [15] reported the dielectric properties of various mammalian tissues and biological fluids at 1 Hz to 10 GHz and indicated the differences of dielectric properties between normal and cancerous tissue. These differences may be due to the fact that cancer cells have the different electrochemical properties of their cell membranes and cancer cells have a higher water content and sodium concentrate than normal cells. In 1996, C. Gabriels *et al.* [31, 32, 33] reported the collection, measurement, and modeling of dielectric properties of the biological tissue at 10 Hz to 20 GHz. In 1994, W. T. Joines *et al.* [16] measured the electrical properties of normal and malignant human tissues from 50 MHz to 900 MHz. The studies of dielectric properties and their differences between normal and cancerous tissues had a valuable contribution to the investigation of the microwave imaging and microwave-induced thermo-acoustic tomography for biological tissue imaging.

The exploration, invention, and development of MITAT for biological tissue imaging had been emerged and reported extensively. In 1999, R. A. Kruger *et al.* [34] introduced a first prototype of thermo-acoustic tomography as an imaging modality for biological tissue imaging. He also invented thermo-acoustic computed tomography [35, 10] for *in vivo* breast cancer imaging at the operating frequency of 434 MHz. L. V. Wang [36] presented a tomographic imaging of biological tissues by use of microwave-induced acoustic signal at 9.4 GHz in 1999. He demonstrated the proportion of intensity between induced thermo-acoustic signal and incident microwave

energy. This proportion of intensity was related by the absorption properties of microwave in medium.

Various geometries of detector array for receiving TA signal in MITAT had been analyzed [37, 38, 39] including planar, cylindrical, and spherical geometries. The cylindrical and spherical geometries of detector arrays can be viewed as a concave array because the imaging domain is inside the closed contour of detector array while the planar geometry is the opened contour of detector array. This concave array was applied to the imaging of breast [20, 21] and brain [22, 23]. In thermo-acoustic tomography for brain imaging, P. Stevanov *et al.* [40] considered the effect of skull and modeled the changes of sound speed of skull for human brain imaging. Pulsed microwave at 3 GHz was used to excited a biological tissue to generate a TA signal and filtered back-projection algorithm was used to reconstruct an image in circular detection of 2-D geometry [9]. Another type of geometry that the imaging domain is outside the closed contour of detector array is called the convex array detection. In application of convex array in MITAT, S. Mukherjee *et al.* investigated a MITAT with an internal imaging for prostate (trans-rectal geometry) imaging [14, 24].

In numerical simulation of TA signal generation for MITAT application, G. Zhu *et al.* [41] and X. Wang *et al.* [42, 21] explored a finite-difference time-domain (FDTD) method for a calculation of TA signal. L. Yao *et al.* [43] presented a finite element method (FEM) solution for a calculation of TA signal for MITAT application. In the generation of TA signal using the FEM, L. Yao *et al.* calculated an electric field distribution in tissue using frequency-domain FEM while a TA signal was calculated by time-domain FEM. This technique can be applied in the case that the microwave pulse was considered very narrow. The generated TA signal was captured in external geometry (concave array) to reconstruct an image using the Levenberg-Marquardt algorithm. S. Mukherjee *et al.* [14, 24] modified Yao's technique to the internal geometry (concave geometry) for trans-rectal imaging.

In consideration of microwave pulse excitation, X. Wang *et al.* [42] presented an analytically study of a TA signal generation by tumor target with different sizes subjected to various widths and waveforms including square pulse, Gaussian pulse, sinusoidal pulse, and triangular pulse. They concluded that the shorter pulse width of all waveforms leads to a better reconstructed image resolution. N. A. Rejesh *et al.* [44] also studied the effect of TA response to various types of EM excitation waveform in which they concluded that higher EM pulse width will reduced the bandwidth of TA signal response. S. Telenkov and A. Mandelis [45, 46] first introduced a novel frequency-swept (chirped) intensity-modulated laser source for photoacoustic imaging and its application of frequency-domain photoacoustic imaging (FD-PTA) for turbid phantoms and chicken breast imaging in 2006. They introduced that this technique can improve the signal-to-noise ratio of TA signal response suggesting that the peak-power of laser source can be reduced. They also suggested that the imaging depth would be confined only 20 mm due to the rapidly decreasing of the measured PTA signal-to-noise ratio. In 2014, H. Nan *et al.* [47] applied an intensity modulation sinusoidal pulse train instead of a single pulse as an alternative microwave pulse excitation in MITAT application in which they suggested that using this technique can reduce the peak power requirement for the system and improve the signal-to-noise ratio of the measured TA signal.

1.4 Problem Statement

Based on the operation mechanism of TAT presented in Section 1.2, the generation of TA signal is basically excited by the EM pulse illumination. Because of the good characteristic of penetration depth of microwave frequency compared to visible laser light into biological tissue, this dissertation focuses on the microwave frequency based TAT which can be termed microwave-induced thermo-acoustic tomography (MITAT). Basically, a microwave pulse is required to be very short due to the requirement of high

resolution of reconstructed image which is reconstructed by the generated TA signal response captured by the detector array. Then the peak-power of the microwave pulse is needed to be very high in order to transfer enough energy for acoustic detection. This section describes the problems and the limitations of MITAT for biological tissue imaging.

In TA signal generation, the energy conversion happens in two steps: the first step is that the EM energy is converted into thermal energy, the second step is that the thermal energy is converted into mechanical energy in the form of a pressure or acoustic wave. In consideration of microwave pulse excitation in MITAT system, the pulse width of microwave pulse is required to be as short as possible in order to obtain a high resolution of reconstructed image [48, 42]. This requirement causes the need of a high peak-power microwave pulse transmitter in order to transmit enough energy into the imaging domain to generating a TA signal, generally in the order of 10 mJ/pulse [49].

In experimental MITAT, the peak-power of microwave transmitters are in the range of 5 kW with 0.4 μs pulse width[50] to 40 MW with 10 ns pulse width [51]. Various research groups [19, 48, 51] adopted a commercial high power microwave pulse transmitter to do MITAT experiments. Some research groups built custom-made microwave pulse transmitters from a magnetron tube [52, 53, 54]. A technique of using high peak-power impulse of nanosecond duration generated by a sparking gap for MITAT was introduced by S. Kellnberger *et al.* [55]. This impulse is coupled to an EM radiator at resonant frequency for a near field radiation to the biological tissue. Another technique for generating high peak-power impulse is to use a transmission line as an energy storage device with a high power switch [56]. C. Lou *et al.* [51] also introduced a breakthrough technique of using an ultra-short microwave pulse by a nitrogen spark gap which can increase image resolution and increase the excitation efficiency.

Even though MITAT has significant benefits of high contrast ratio, high resolution, non-ionizing radiation, and cost effectiveness, the need of high peak-power short microwave pulse transmitter adds significantly to instrument size and cost. This study applied a time-domain finite element method focuses on reducing the high peak-power of microwave transmitter for MITAT system. The necessity of using time-domain numerical method comes from the applying of modulated chirp pulse as an alternative microwave pulse excitation instead of using the modulated Gaussian pulse. Moreover, TDFEM can handle complex geometries of biological tissue.

1.5 Motivation of the Work

One drawback of requiring a microwave pulse transmitter with high peak-power output in MITAT system is that the MITAT system is too bulky [54]. The existing experimental MITAT systems by several research groups [12, 20, 54] adopted a commercial high-power microwave pulse generator with a waveguide system as a source of EM pulse. This drawback could be overcome by reducing the peak-power of microwave pulse transmitter in the MITAT system. This improvement can make an MITAT system more efficient and would be clinically operated as an alternative and effective medical imaging modality.

In this study, we proposes a technique of applying a modulated chirp pulse to be a microwave pulse excitation instead of a conventional modulated Gaussian pulse [57]. This method is based on the assumption that the more pulse width the more energy can be transmitted which lowers the peak power of the microwave transmitter. However the resolution of reconstructed image can still be obtained by the result of applying a cross-correlation detection as a receiving process that correlates signals between the chirp reference and the chirped TA response in image reconstruction process. In this numerical simulation, a novel application of TDFEM in both the electric field and pressure field generation will be applied to examine the TA signal

generation in biological tissue excited by the modulated chirp pulse. The analysis of the peak-power reduction and range resolution will be included. The analysis of reconstruction artifacts in convex geometry will also be introduced.

1.6 Organization of the Thesis

In this Thesis, the detail of microwave-induced thermo-acoustic tomography is presented in Chapter 2 including the forward step of TA signal generation and the inverse step of TA signal detection and image reconstruction. The dielectric and acoustic properties of biological tissues are included in this chapter. This chapter also describes two types of microwave pulse excitations for MITAT systems. An applying of a modulated chirp pulse as a microwave pulse excitation for lowering the high peak-power required for TA signal generation is also presented in this chapter.

A time-domain finite element method (TDFEM) for a simulation of TA signal generation in biological tissue model is presented in Chapter 3. This chapter describes the FEM formulation for the time-varying electric field equation and time-varying pressure field equation. A domain truncation using Bayliss-Turkel radiation boundary condition and Newmark's method for time discretization will incorporate with the FEM formulations to form a numerical solution for TA signal generation is described. Chapter 4 presents the solutions of TA wave equation excited by the conventional modulated Gaussian pulse and their reconstructed images while Chapter 5 shows solutions of TA wave equation excited by the modulated chirp pulse and their reconstructed images. Chapter 6 presents the analysis of this study including the peak-power reduction, range resolution, reconstruction artifacts, and mechanical delay for TA signal generation. The conclusion of this numerical study, the contributions of this study, and the future directions will be described in Chapter 7.

CHAPTER 2

MICROWAVE-INDUCED THERMO-ACOUSTIC TOMOGRAPHY

2.1 Introduction

This chapter describes modeling of thermo-acoustic tomography (TAT). In terms of TAT, it can be referred to as microwave-induced thermo-acoustic tomography (MITAT) or photo-acoustic tomography (PAT) depending on the frequency band of electromagnetic excitation. This chapter will focus on MITAT for biological tissue imaging. The excitation pulse of current density is in microwave frequency and microwave absorption properties of biological tissues will be considered as the contribution in TA signal generation. The modeling of this imaging modality can be divided into two steps: a forward step and an inverse step. In the forward step, a generation of the pressure field by a pulsed electric field excitation will be described. The pulsed electric field excitation will be categorized into two pulse shapes: the modulated Gaussian pulse, and the proposed modulated chirp pulse. In the inverse step, detection of TA signal by acoustic transducer, a correlation detection, and a reconstruction of image will be described.

2.2 Dielectric and Acoustic Properties of Biological Tissues

In an analysis of electric field interaction with a biological tissue and a thermo-acoustic signal generation by electric field absorption in the tissue, the dielectric and acoustic properties of biological tissue is necessary. Gabrial *et al.* collected [31], measured [32], and modeled [33] the dielectric properties of biological tissues in the frequency range of 10 Hz to 20 GHz. The basic dielectric and acoustic properties of selected biological tissues are shown in Table 2.1 and 2.2, respectively. The dielectric properties of biological tissue will be shown only the relative permittivity (ε_r) and the electrical conductivity (σ). This is because the relative permeability (μ_r) is considered as a constant in biological tissue [19] and is approximately equal to the relative permeability of free space. The expansion coefficient, heat capacity, mass density, and speed of the pressure field are presented as the acoustic properties of the biological tissues. The acoustic properties of biological tissue can be represented with the thermal expansion coefficient (β_e), heat capacity (C_p), mass density (ρ), and acoustic velocity (v_s).

Table 2.1: Dielectric properties of healthy biological tissues at 915 MHz.

Biological tissues	Relativy Permittivity, $\varepsilon_r(\cdot)$	Electrical Conductivity, σ(S/m)
Breast [58]	80	0.1, 0.3*
Prostate [24]	60.5	1.216, 0.608*

* cancerous cells

2.3 Forward Step: Thermo-Acoustic Signal Generation

A principle of TA signal generation is based on a physical phenomenon in which a thermal energy in the material can be converted into acoustic energy or vice versa. In this section, a scalar wave equation of EM field is described for the step 1 of the

Table 2.2: Acoustic properties of biological tissues.

Biological Tissue	Expansion Coefficient, β_e(1/K)	Heat Capacity, C_p(J/kg/K)	Mass Density, ρ(kg/m^3)	Acoustic Velocity, v_s(m/s)
Breast [17]	3×10^{-4}	3550	1020	1510
Breast [24]	4×10^{-4}	4000	1000	1500
Skin [17]	3×10^{-4}	3500	1100	1537
Muscle [17]	3×10^{-4}	3510	1041	1580
Tumor [17]	3×10^{-4}	3510	1041	1580

forward step. The current density in the scalar wave equation represents a source of electric field generation which is a function of position and time. In this study, two kinds of temporal current density functions will be described: one is a modulated Gaussian pulse and another is a modulated chirp pulse. Step 2 of the forward step is the generation of pressure field at which the source of this pressure field generation is from the power loss density which is in the form of EM field absorption in the tissue.

2.3.1 Scalar electromagnetic wave equation

In an excitation for a generation of TA signal in biological tissues, the electromagnetic field is applied to convey energy into the biological tissues. For a 2-D problem geometry, the scalar form of the EM wave equation can be applied. In this study, the scalar wave equation (Helmholtz equation) of electric field in TM^z mode, which is derived from Maxwell's equation, is adopted as a model of EM field interaction with the biological tissue. The time-varying electric field wave equation can be written as

$$\frac{1}{\mu_r}\nabla^2 E_z(\mathbf{r},t) - \mu_0\sigma\frac{\partial}{\partial t}E_z(\mathbf{r},t) - \frac{\varepsilon_r}{c^2}\frac{\partial^2}{\partial t^2}E_z(\mathbf{r},t) = \mu_0\frac{\partial}{\partial t}J(\mathbf{r},t), \tag{2.1}$$

where $E_z(\mathbf{r}, t)$ is the z-component of electric field ($\mathrm{V{\cdot}m^{-1}}$) which is the function of spatial position $\mathbf{r}$ and time t, μ_r is the relative permeability, $\mu_0 = 4\pi \times 10^{-7}$ $\mathrm{H{\cdot}m^{-1}}$ is the permeability of free space, $\varepsilon_0 = 8.854 \times 10^{-12}$ $\mathrm{F{\cdot}m^{-1}}$ is the permittivity of free space, ε_r is the relative permittivity, $c = 1/\sqrt{\mu_0 \varepsilon_0}$ is the speed of electromagnetic wave in free space ($\mathrm{m{\cdot}s^{-1}}$), σ is the electric conductivity ($\mathrm{S{\cdot}m^{-1}}$), and $J(\mathbf{r}, t)$ is the impressed current density ($\mathrm{A{\cdot}m^{-2}}$). The current density in Eq.(2.1) can be considered as a source for electric field generation which can be written as

$$J(\mathbf{r}, t) = A(\mathbf{r}) f_s(t), \tag{2.2}$$

where $A(\mathbf{r})$ is the spatial function represents the source location for the electric field distribution on the imaging domain, $f_s(t)$ is the temporal function of the current density represents the shape of microwave pulse. In general, the temporal function of the current density is modeled as the modulated Gaussian pulse for conventional TAT system. This study presents a modulated chirp pulse as an alternative temporal function of current density.

Modulated Gaussian pulse

A Gaussian function $G(t)$ is normally represented an envelope of short microwave pulse for MITAT simulation which can be written as

$$G(t) = A_g \exp\left(-\frac{(t - t_d)^2}{2\sigma_g^2}\right), \tag{2.3}$$

where A_g is the amplitude of Gaussian pulse, t_d is the delay time that represents the position of peak amplitude of the pulse, and σ_g is the standard deviation of the pulse. The full-width at half-maximum (FWHM) of the Gaussian pulse can be written in

the form of

$$\text{FWHM} = 2\sqrt{2\ln 2} \times \sigma_g. \tag{2.4}$$

The modulated Gaussian pulse $f_{s1}(t)$ is a result of an intensity modulation between the Gaussian function $G(t)$ and a sinusoidal carrier of frequency f_c which can be written in Eq.(2.5). An example of a modulated Gaussian pulse with an FWHM of 0.5 μs, a peak delay of 1 μs, and a carrier frequency of 915 MHz within the pulse period duration T can be shown in Figure 2.1.

$$f_{s1}(t) = A_g \exp\left(-\frac{(t-t_d)^2}{2\sigma_g^2}\right) \sin(2\pi f_c t) \quad ; 0 \leq t \leq T. \tag{2.5}$$

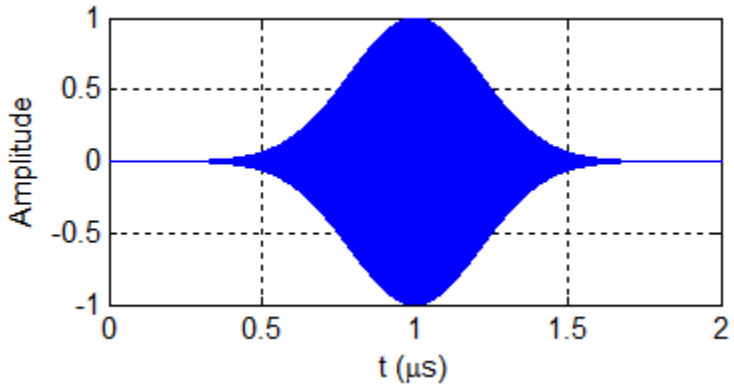

Figure 2.1: Modulated Gaussian pulse with FWHM of 0.5 μs, peak amplitude delay of 1 μs, and carrier frequency of 915 MHz.

Modulated chirp pulse

A technique of applying a modulated chirp pulse as a microwave pulse excitation in MITAT initially came from a discussion with Dr.Piao, a faculty member of School of Electrical and Computer Engineering, Oklahoma State University. He suggested alternative microwave pulses that can probably be applied as a pulse excitation

in thermo-acoustic tomography including conventional Gaussian pulse, chirped microwave pulse, intensity-modulated chirp pulse, and modulated Gaussian pulse at the position of chirp peak. After an initial testing, the modulated chirp pulse showed the potential to be applied as a microwave pulse in microwave-induced thermo-acoustic tomography with the ability to reduce the microwave peak power.

The modulated chirp pulse is proposed and described in this section. The purpose of this technique is to reduce the high peak-power of the microwave transmitter of MITAT. The idea behind this is that the energy can be more transfer if the pulse width is wider. This technique can reduce the need of high peak transmitting power of microwave transmitter. The resolution of a reconstructed image by using the chirp responses can still be obtained at high resolution by using a correlation detector which will correlate the TA chirp response from tissue sample and the chirp reference. A modulated chirp pulse $f_{s2}(t)$ with the pulse period duration T can be written as

$$f_{s2}(t) = \begin{cases} A_c \sin\left(2\pi\left[f_a t + \frac{(f_b - f_a)}{2T_c} t^2\right]\right) \sin\left(2\pi f_c t\right) & ; 0 \leq t \leq T_c \\ 0 & ; T_c < t \leq T \end{cases}, \tag{2.6}$$

where A_c is the peak amplitude of the chirp, f_a and f_b are the starting and stopping frequency of the chirp signal, respectively, T_c is the chirp duration that takes between the sweeping of starting and stopping frequencies, and f_c is the carrier frequency. A modulated chirp pulse with $f_a = 20$ kHz, $f_b = 100$ kHz, $f_c = 915$ MHz, $T_c = 100$ μs can be shown in Figure 2.2

2.3.2 Thermo-acoustic wave equation

The thermo-acoustic wave equation is a second order partial differential equation which can be written as [43]

$$\nabla^2 p(\mathbf{r}, t) - \frac{1}{v_s^2} \frac{\partial^2}{\partial t^2} p(\mathbf{r}, t) = -\frac{\beta_e}{C_p} \frac{\partial}{\partial t} \left\{\sigma(\mathbf{r}) \left|E_z(\mathbf{r}, t)\right|^2\right\}, \tag{2.7}$$

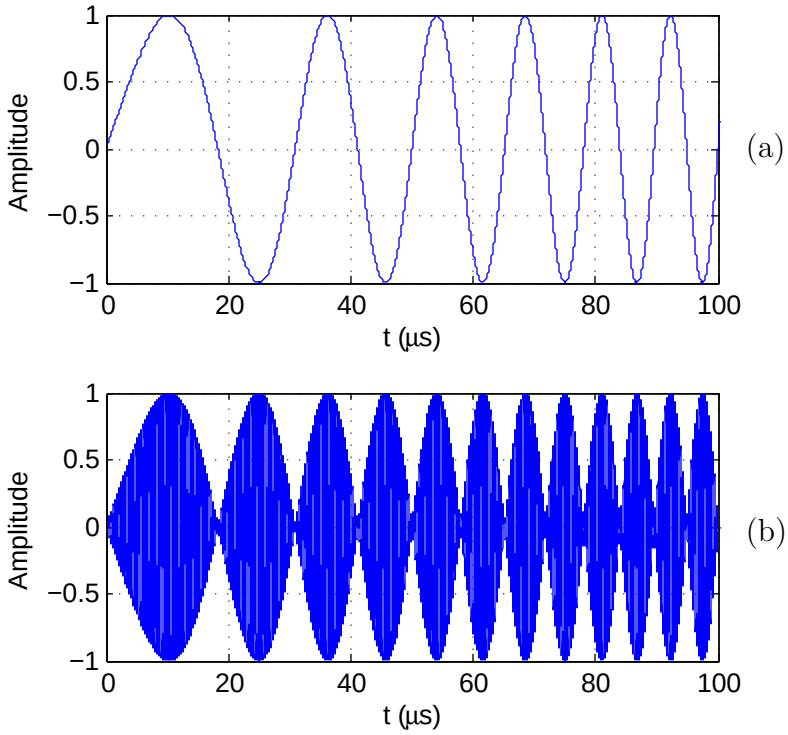

Figure 2.2: (a) A chirp pulse with the starting frequency of 20 kHz, stopping frequency of 100 kHz, chirp duration of 100 μs, and (b) an intensity modulation of chirp pulse with the carrier frequency of 915 MHz.

where $p(\mathbf{r}, t)$ is the pressure field (Pascal(Pa) or kg·m^{-1}·s^{-2}), which can be called thermo-acoustic wave, which is the function of spatial position $\mathbf{r}$ and time t , β_e is the isobaric temperature coefficient of volume expansion (K^{-1}), C_p is the specific heat capacity (J·kg^{-1}·K^{-1}) and v_s is the speed of pressure wave (m·s^{-1}) in material. The analytical solution to the thermo-acoustic wave equation in (2.7) can be shown as [37]

$$p(\mathbf{r}, t) = \frac{\beta_e}{4\pi C_p} \iint \sigma(\mathbf{r}') \frac{\partial |E_z(\mathbf{r}', t')|^2}{\partial t'} \frac{d\mathbf{r}'}{|\mathbf{r} - \mathbf{r}'|} \bigg|_{t'=t-\frac{|\mathbf{r}-\mathbf{r}'|}{v_s}} . \tag{2.8}$$

In the equation of thermo-acoustic wave shown in Eq.(2.7) with its solution shown in Eq.(2.8), it describes the generation of pressure field (TA wave) in medium which is excited by power loss density, $\sigma(\mathbf{r}')|E_z(\mathbf{r}', t')|^2$, generated in that medium. The power loss density is generated by the electrical conduction of the electric field absorption in the medium in which this electric field is the solution of the equation presented in Eq.(2.1). In Eq.(2.7), the ratio of β_e/C_p on the right-hand side of the equation can be considered as a coefficient of TA excitation source.

2.4 Inverse Step: Acoustic Detection and Image Reconstruction

In this section, an inverse step model is presented for microwave-induced thermo-acoustic tomography in which the modulated chirp pulse is used as the microwave pulse excitation. The diagram of the model can be depicted in Figure 2.3.

The diagram consists of three parts: the acoustic detector, the correlation detection, and the image reconstruction. Each part of this inverse step model will be described in the following subsections.

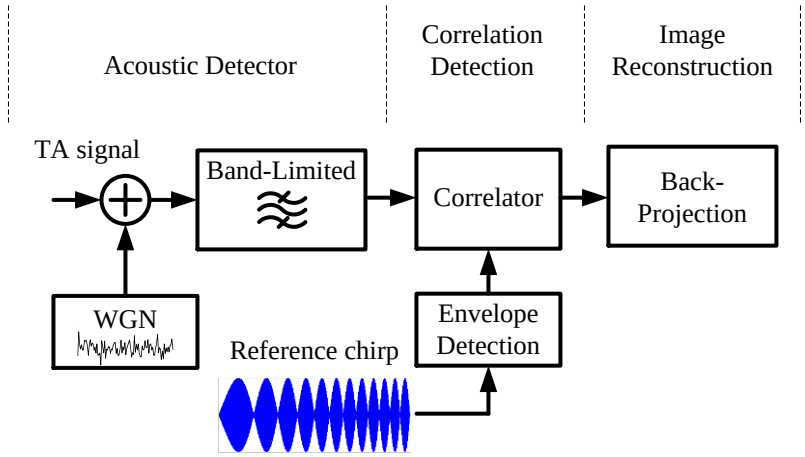

Figure 2.3: An inverse step model for microwave-induced thermo-acoustic tomography with a modulated chirp pulse excitation.

2.4.1 Acoustic detector and array

In acoustic detector modeling, the white Gaussian noise (WGN) is taken into account in order to consider the noise generated in biological tissue and in acoustic detector itself while receiving via the acoustic detector. The WGN is added into the numerically generated TA signal that is captured on the detector along the concave and convex detector array, as shown in Figure 1.3(a) and (b), to form the noisy TA signal.

Then the noisy TA signal is passed through a band-pass filter according to the finite bandwidth characteristic of acoustic detector. The TA signal response from the microwave pulse excitation on biological tissue falls in the ultrasonic band suggesting that it is a longitudinal acoustic wave and that the frequency is greater than the upper limit of human hearing range (20 kHz). An ultrasonic transducer or sensor will be applied as an acoustic detector. Because of the finite bandwidth of the ultrasonic sensor, it can be modeled as a band-pass filter. In this study, a 2^{nd} order Butterworth band-pass filter of the bandwidth of 20 kHz to 2 MHz is applied as a finite bandwidth acoustic detector model.

2.4.2 Cross-correlation detection

After the noisy TA signal is filtered in the previous subsection, the finite bandwidth of the noisy TA signal is correlated with the reference chirp pulse in order to determine a delay time between the TA signal and the reference. This delay time will correspond with the velocity of the TA signal in biological tissue and the distance between target and the detector. This delay time is necessary in the time domain reconstruction algorithm using back-projection. The delay time detected by each detector is projected back into the imaging domain to reconstruct an image representing the local EM absorption. The process of extracting the delay time between the TA chirp response and the chirp reference is the cross-correlation detection which can be shown as

$$(f_s \star g)(\tau) = \int_{-\infty}^{\infty} f_s^*(t) g(t+\tau) dt, \tag{2.9}$$

where f_s denotes the function of chirp reference, g is the TA response that is captured from the acoustic detector, and the superscript * denotes the complex conjugate.

2.4.3 Back-projection algorithm for image reconstruction

In the reconstruction of the image representing the microwave absorption distribution inside the imaging domain in this study, the back-projection is selected as an image reconstruction algorithm for TAT because it is the most common algorithm for TAT. With the back-projection method, it is based on the restriction that the velocity of the TA wave traveling across the imaging domain is needed to be constant. The back-projection algorithm can be written as [9]

$$D(\rho, \varphi, z) = \frac{1}{2\pi v_s^2} \iint_{\mathbf{r}} d\mathbf{r} [\mathbf{n} \cdot \mathbf{n}_0] \frac{1}{t} \frac{\partial p(\mathbf{r}_0, t)}{\partial t} \bigg|_{t=\frac{|\mathbf{r}-\mathbf{r}_0|}{v_s}}, \tag{2.10}$$

where

$$[\mathbf{n}\cdot\mathbf{n}_0]=\frac{|\rho-\rho_0|}{|\mathbf{r}-\mathbf{r}_0|}=\sqrt{\frac{\rho^2+\rho_0^2-2\rho\rho_0\cos(\varphi-\varphi_0)}{|\mathbf{r}-\mathbf{r}_0|^2}}=\sqrt{1-\frac{(z-z_0)^2}{|\mathbf{r}-\mathbf{r}_0|^2}}, \tag{2.11}$$

where D is the spatial region represents the reconstructed image, $\mathbf{r}_0$ represents the spatial position of line that TA signal is captured, and $[\mathbf{n}\cdot\mathbf{n}_0]$ denotes the weighting factor which it is equal to 1 in our case because we are using 2-D geometry where $z=z_0=0$.

2.5 Summary

In this chapter, the model of TAT had been presented in forward step and inverse step. In the forward step, the electric field wave equation and the thermo-acoustic wave equation were formed as the governing equation for the generation of TA signal in biological tissue medium. The temporal function of current pulse source was used to determine the time-varying electric field deposited in biological tissue and this time-varying electric field was used as a time-varying source function for the TA signal generation. The generated TA signal was captured to perform an image reconstruction based on the inverse step model. The dielectric and acoustic properties of biological tissue were also presented.

CHAPTER 3

TIME-DOMAIN FINITE ELEMENT METHOD FOR THERMO-ACOUSTIC SIGNAL GENERATION

3.1 Introduction

In a simulation of TA signal generation in biological tissue where the excitation pulse of current density is the modulated chirp pulse as described in Chapter 2, a time-domain numerical method is necessary. This chapter presents a novel time-domain numerical procedure using the time-domain finite element method (TDFEM) for the simulation of TA signal generation in complex biological tissue structure. In applying of TDFEM to this problem, this chapter describes the FEM formulations of both time-varying electric field equation and time-varying pressure field equations, Bayliss-Turkel radiation boundary condition (RBC) for domain truncation, and Newmark's method for time discretization.

The computational domain is truncated and the Bayliss-Turkel RBC is applied as a boundary condition to suppress reflected wave at the boundary. This truncation of the computational domain is to limit the computational cost for numerical computation of open area problems. Newmarks method will be applied in the formulation of time stepping scheme. In this study, we applied the time-domain finite element method (TDFEM) for the calculations of both electric field and pressure field because of its flexibility in geometrical and material modeling. The result of the calculated time-

varying electric field will become a source for a generation of time-varying pressure field (thermo-acoustic signal).

3.2 FEM Formulation for Electric Field Equation

This section describes an FEM formulation for the electric field wave equation in the time domain [59]. From the electric field wave equation in Eq.(2.1) and its boundary condition for the domain truncation which will be shown in Eq.(3.17), it can be written in the form of time-dependent ordinary differential equation as

$$[M]\frac{d^2\{E_z\}}{dt^2} + [P]\frac{d\{E_z\}}{dt} + [S]\{E_z\} = \{f\}, \tag{3.1}$$

where the element of coefficient matrices $[M]$, $[P]$, $[S]$, and vector $\{f\}$ can be written as

$$M_{ij} = \frac{1}{c^2}\iint_s \varepsilon_r N_i N_j ds, \tag{3.2}$$

$$P_{ij} = \mu_0 \iint_s \sigma N_i N_j ds, \tag{3.3}$$

$$S_{ij} = \iint_s \frac{1}{\mu_r}\nabla N_i \cdot \nabla N_j ds - \oint_l \frac{1}{\mu_r} N_i \frac{\partial N_j}{\partial n} dl, \tag{3.4}$$

$$f_i = -\mu_0 \iint_s N_i \frac{\partial J}{\partial t} ds, \tag{3.5}$$

where N_i is the linear basis function or interpolation function at global node i of the FEM mesh. At element e of the mesh, local basis function at node i for triangular element can be written as

$$N_i^e(x,y) = \frac{1}{2\Delta^e}\left(a_i^e + b_i^e x + c_i^e y\right), \tag{3.6}$$

where Δ^e is the area of triangle element e and a_i^e, b_i^e , and c_i^e are the coefficients of basis function at local node i which can be written as

$$a_i = x_{i+1}y_{i+2} - x_{i+2}y_{i+1}, \tag{3.7}$$

$$b_i = y_{i+1} - y_{i-1}, \tag{3.8}$$

$$c_i = x_{i-1} - x_{i+1}. \tag{3.9}$$

The index i assumes to be 1, 2, and 3 cyclically. Because there are 3 local nodes for each triangular element, the unknown E_z^e the node e can be obtained at any position on the node by

$$E_z^e(x, y; t) = \sum_{i=1}^{3} N_i^e(x, y) E_{z,i}^e(t), \tag{3.10}$$

where, $E_{z,i}^e$ is the solution of z-component electric field at local node i on the element e. The global approximate solution can be obtained by superposition of all N elements on the mesh which can be written as

$$E_z(x, y; t) \approx \sum_{e=1}^{N} E_z^e(x, y; t). \tag{3.11}$$

3.3 FEM Formulation for Pressure Field Equation

From the thermo-acoustic wave equation as shown in Eq.(2.7) and its boundary condition of the 1$^{\text{st}}$order Bayliss-Turkel radiation boundary condition for domain truncation which will be shown in Eq.(3.20), the FEM formulation of the thermo-acoustic wave equation can be written in the form of time-dependent ordinary differential equation

as [43]

$$[T]\frac{d^2\{p\}}{dt^2} + [C]\frac{d\{p\}}{dt} + [K]\{p\} = \{B\}, \tag{3.12}$$

where the element of coefficient matrices $[T]$, $[C]$, $[K]$, and vector $\{B\}$ can be written as

$$T_{ij} = \frac{1}{v_s^2}\iint_s N_i N_j ds, \tag{3.13}$$

$$C_{ij} = \frac{1}{v_s^2}\oint_l N_i N_j dl, \tag{3.14}$$

$$K_{ij} = \iint_s \nabla N_i \cdot \nabla N_j ds + \frac{1}{2r}\oint_l N_i N_j dl, \tag{3.15}$$

$$B_i = \frac{\beta_e}{C_p}\iint_s N_i \left(\sum_k N_k \left(\sigma |E_z|^2\right)\right) ds. \tag{3.16}$$

By the same procedure that is described in the previous section, this formulation will be used to approximately calculate the TA signal on FEM mesh. The reason of applying TDFEM for modeling this problem in both electric field and pressure field calculation is because the modulated chirp pulse is applied as the microwave pulse excitation to the biological tissue material and TDFEM is also flexible in both geometrical and material modeling.

3.4 Domain Truncation

The spatial domain of PDE-based radiation problem must be truncated in numerical computation in order to limit the computational cost. In this study, the 2$^{\text{nd}}$ order Bayliss-Turkel RBC [60] is applied on the outer boundary of circular imaging domain as an absorption boundary at near field for the calculation of electric field. The

Bayliss-Turkel RBC can be written as

$$\frac{\partial E_z^s}{\partial \rho} = \tilde{\alpha} E_z^s + \tilde{\beta} \frac{\partial^2 E_z^s}{\partial \phi^2}, \tag{3.17}$$

where E_z^s is the scattering electric field of z component, ρ is the radius of computation region, $\tilde{\alpha}$ and $\tilde{\beta}$ are the coefficients which can be written as

$$\tilde{\alpha}(\rho) = \frac{-jk - 3/(2\rho) + 3j/(8k\rho^2)}{1 - j/(k\rho)}, \tag{3.18}$$

$$\tilde{\beta}(\rho) = -\frac{j/(2k\rho^2)}{1 - j/(k\rho)}. \tag{3.19}$$

To truncate the computation domain for calculating the time-varying electric field, Eq.(2.1) is substituted by Bayliss-Turkel RBC of Eq.(3.17) with the relation between total, incident, and scattering electric field which can be written as $E_z = E_z^s + E_z^{inc}$ where E_z^{inc} denotes the incident electric field. In formulation for the numerical implementation, this substitution can be done by replacing the $\partial N_j / \partial n$ term in the second term of the right hand side of Eq.(3.4) with Eq.(3.17). The first order Bayliss-Turkel RBC which can be written as [43]

$$\nabla p \cdot \hat{n} = -\frac{1}{v_s} \frac{\partial p}{\partial t} - \frac{p}{2r}, \tag{3.20}$$

where $\hat{n}$ is the normal unit vector and r is the radius of the computational region. Equation (3.20) is adopted as a near field RBC for the calculation of pressure field in Eq.(2.7). The substitution of this RBC into the pressure field equation in Eq.(2.7) is performed in the coefficient matrices in Eq.(3.14) and in the second term on the right hand side of Eq.(3.15).

3.5 Newmark's Method

The system of time varying equations shown in Eq.(3.1) and Eq.(3.12) present the generation of electric field and thermo-acoustic field, respectively. These system of equations are used to describe the behavior of electric field and TA field in biological tissue in space and time domain. For numerical simulation of the time-varying of 2D, there are two type of discretization: space and time discretization. In space discretization, the FEM mesh and the coefficient matrices in the FEM formulations are used to calculate the solution of unknown on all non-prescribed nodes of the mesh by solving of the system of linear equations *i.e.* $[A]\{x\} = \{b\}$. While the discretization of time for the calculation of unknown that varying in time is performed using Newmark method. The equations of Newmark algorithm, which is derived from Taylor series and the forward difference approximation $\dddot{u}_t = (\ddot{u}_{t+\Delta t} - \ddot{u}_t)/\Delta t$, can be written as

$$u_{t+\Delta t} = u_t + \Delta t \dot{u}_t + (0.5 - \beta)\Delta t^2 \ddot{u}_t + \beta \Delta t^2 \ddot{u}_{t+\Delta t}, \tag{3.21}$$

$$\dot{u}_{t+\Delta t} = \dot{u}_t + (1 + \gamma)\Delta t \ddot{u}_t + \gamma \Delta t \ddot{u}_{t+\Delta t}, \tag{3.22}$$

$$\ddot{u}_{t+\Delta t} = \frac{1}{\beta \Delta t^2}(u_{t+\Delta t} - u_t) - \frac{1}{\beta \Delta t}\dot{u}_t - \left(\frac{1}{2\beta} - 1\right)\ddot{u}_t, \tag{3.23}$$

where u_t, $\dot{u}_t$, and $\ddot{u}_t$ are the unknowns, and the first derivative and second derivative of the unknowns at time t, respectively, $u_{t+\Delta t}$, $\dot{u}_{t+\Delta t}$, and $\ddot{u}_{t+\Delta t}$ are the unknowns, and the first derivative and second derivative of the unknowns at time $t+\Delta t$, respectively, Δt is the time increment step, β and γ is the Newmarks parameter which $\beta = 1/4$ and $\gamma = 0.5$ for average acceleration method. Substitution of equation (3.21)-(3.23)

into (3.1) and (3.12) yields

$$
\begin{aligned}
E_{t+\Delta t} = & \left\{ \frac{1}{\beta \Delta t^2} E_t + \frac{1}{\beta \Delta t} \dot{E}_t + \left(\frac{1}{2\beta} - 1 \right) \ddot{E}_t \right\} \left[\frac{1}{\beta \Delta t^2} M + \frac{\gamma}{\beta \Delta t} P + S \right]^{-1} M \\
& + \left\{ \frac{\gamma}{\beta \Delta t} E_t + \left(\frac{\gamma}{\beta} - 1 \right) \dot{E}_t + \left(\frac{\gamma}{2\beta} - 1 \right) \Delta t \ddot{E}_t \right\} \left[\frac{1}{\beta \Delta t^2} M + \frac{\gamma}{\beta \Delta t} P + S \right]^{-1} P \\
& + \left[\frac{1}{\beta \Delta t^2} M + \frac{\gamma}{\beta \Delta t} P + S \right]^{-1} \{f\}_{t+\Delta t}
\end{aligned}
\tag{3.24}
$$

for electric field calculation and

$$
\begin{aligned}
p_{t+\Delta t} = & \left\{ \frac{1}{\beta \Delta t^2} p_t + \frac{1}{\beta \Delta t} \dot{p}_t + \left(\frac{1}{2\beta} - 1 \right) \ddot{p}_t \right\} \left[\frac{1}{\beta \Delta t^2} T + \frac{\gamma}{\beta \Delta t} C + K \right]^{-1} T \\
& + \left\{ \frac{\gamma}{\beta \Delta t} p_t + \left(\frac{\gamma}{\beta} - 1 \right) \dot{p}_t + \left(\frac{\gamma}{2\beta} - 1 \right) \Delta t \ddot{p}_t \right\} \left[\frac{1}{\beta \Delta t^2} T + \frac{\gamma}{\beta \Delta t} C + K \right]^{-1} C \\
& + \left[\frac{1}{\beta \Delta t^2} T + \frac{\gamma}{\beta \Delta t} C + K \right]^{-1} \{B\}_{t+\Delta t}
\end{aligned}
\tag{3.25}
$$

for pressure field calculation, respectively. Equation (3.24) describes the generation of E-field at each time step Δt. The generation of pressure field (thermo-acoustic signal) at each time step can be described in Eq.(3.25). The diagram of the numerical simulation of MITAT system can be shown in Figure 3.1.

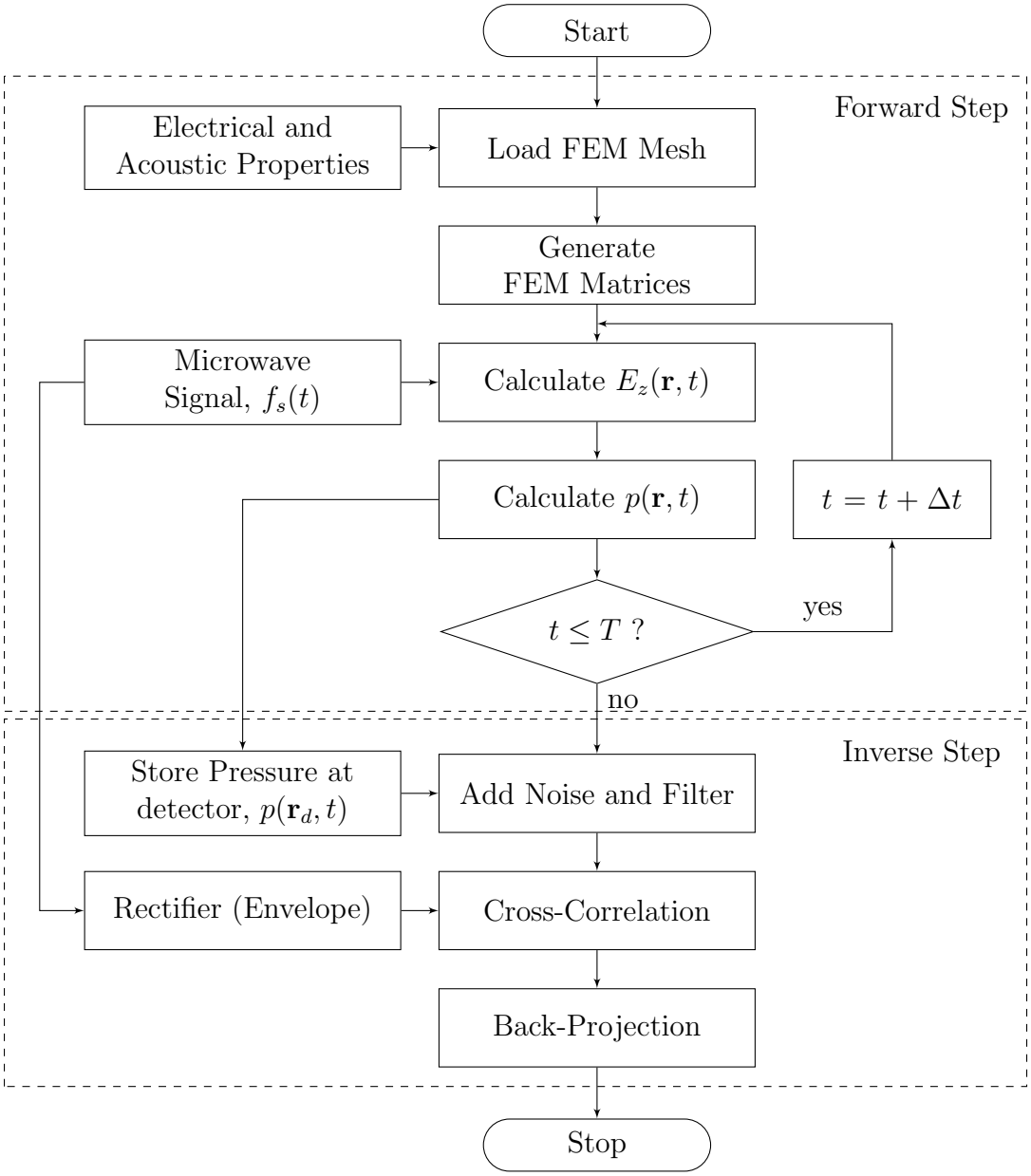

Figure 3.1: Flow chart for a simulation of time-domain thermo-acoustic tomography

3.6 Summary

This chapter described the spatial discretization using the finite element method and time discretization using the Newmark's method for the calculation of time-varying TA signal and time-varying electric field which forms the thermo-acoustic signal gen-

eration. The time-varying electric field equation was written in the form of ordinary differential equation with the FEM coefficient matrices. The time-varying pressure field equation was written in the form of ordinary differential equation with the FEM coefficient matrices. The domain truncation for the limitation of the computation cost utilized the Bayliss-Turkel RBC which incorporated with the FEM formulation for both the electric field equation and the pressure field equation to absorb the reflected electric field and pressure field on the outer boundary of the computational domain. The Newmark's algorithm was described and formulate the time-domain finite element formulation for the electric field and the pressure field. With this numerical formulation for the generation of TA signal in time domain that described in this chapter and the inverse step that described in Chapter 2, the time domain numerical modeling of MITAT system was established. By using this time domain numerical procedure as shown in Figure 3.1, the numerical results of TA signal generations and image reconstructions for an MITAT system using the modulated Gaussian pulse excitation can be presented in Chapter 4 while the numerical results using the modulated chirp pulse excitation can be presented in Chapter 5.

CHAPTER 4

THERMO-ACOUSTIC SIGNAL GENERATION AND IMAGE RECONSTRUCTION USING MODULATED GAUSSIAN PULSE

4.1 Introduction

This chapter describes the numerical solutions of TA signal generation and their reconstructed images of biological tissue using the step described in Chapter 2, the TDFEM described in Chapter 3 and the flowchart in Figure 3.1. In this numerical simulation, the TDFEM formulation that was described in Chapter 3 is applied to calculate the TA signal response where the conventional modulated Gaussian pulse is adopted as an EM pulse excitation. When the TA signal is numerically generated, it is captured with either a concave or convex array along each detector location represented which can be shown in Figure 1.3. The imaging domain is inside the array contour in the concave case while the imaging domain is outside the array contour for the convex case. After the captured TA signal at each detector position is stored, it is used to reconstruct the image represented the EM absorption distribution by using the back-projection algorithm described in Chapter 2.

A normalized Gaussian pulse, shown in Figure 4.1(a), with the pulse period of 200 μs, FWHM of 0.5 μs and peak position occurs at 1 μs is modulated with a carrier frequency of 915 MHz to form a modulated Gaussian pulse as shown in Figure 4.1(b). This modulated Gaussian pulse is the microwave pulse excitation for TA

signal generation in this chapter. The simulation will be performed in concave and convex array cases. Each case will be divided into different geometries of various target positions, target dimensions and target numbers.

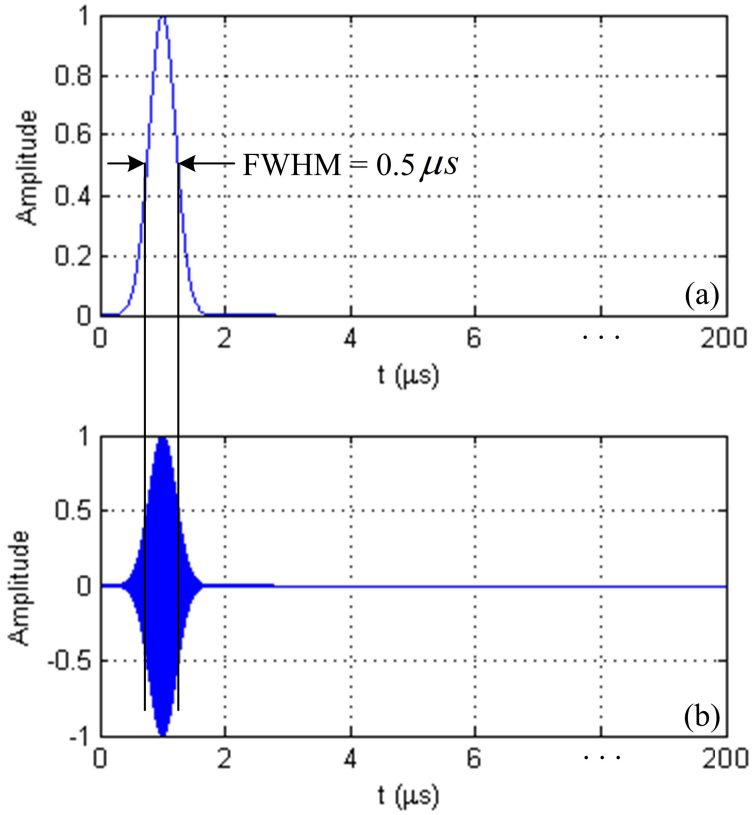

Figure 4.1: (a) Gaussian pulse and (b) modulated Gaussian pulse.

4.2 Thermo-Acoustic Signal Generation and Image Reconstruction in Concave Array Case

In this study, a biological tissue mimicking material is assumed in which it is inhomogeneous in dielectric property (for microwave absorption) but homogeneous in acoustic property (for TA field generation and propagation). The dielectric properties for the simulation in concave case can be shown in Table 4.1 and the acoustic properties for all biological tissue regions can be shown in Table 4.2. The simulation

results for the generation of TA signal in various target positions, dimensions, and numbers are presented in the following subsections.

Table 4.1: Dielectric properties of biological tissue at 915 MHz for simulations in concave array case [24].

Dielectric Properties	Symbol	Value	Unit
Electrical Conductivity	σ	0.1, 0.3*	S/m
Relative Permittivity	ε_r	80	1

* for target region.

Table 4.2: Acoustic properties of biological tissue for simulations [24].

Acoustic Properties	Symbol	Value	Unit
Heat Capacity	C_p	4000	J/kg/K
Expansion Coefficient	β_e	4×10^{-4}	1/K
Speed of Acoustic Wave	v_s	1500	m/s

4.2.1 Variation of target positions

Figure. 4.2 shows the geometries and their corresponding FEM meshes for the simulations of TA signal generated by various target positions with concave array detector. The geometry of the biological tissue with a 5 mm radius target located at $x = 0$ cm, $y = 1.5$ cm and its corresponding FEM mesh can be shown in Figure 4.2(a) and (d), respectively. The geometry of the biological tissue with a 5 mm radius target located at $x = 0$ cm, $y = 2.0$ cm and its corresponding FEM mesh can be shown in Figure 4.2(b) and (e), respectively. The geometry of the biological tissue with a 5 mm radius target located at $x = 0$ cm, $y = 2.5$ cm and its corresponding FEM mesh can be shown in Figure 4.2(c) and (f), respectively.

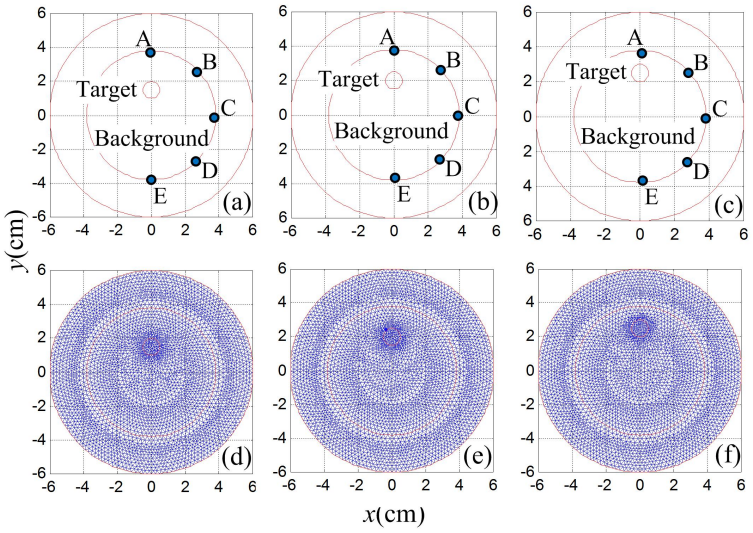

Figure 4.2: Geometries and FEM meshes of biological tissue with concave array detector and a target located at: (a) $y = 1.5$ cm, (b) $y = 2.0$ cm, (c) $y = 2.5$ cm. (d),(e), and (f) show the corresponding FEM meshes of geometry in (a), (b), and (c), respectively.

The dielectric and acoustic properties of background and target of the biological tissues for the simulation is presented in Table 4.1 and Table 4.2, respectively. The microwave pulse excitation in each geometry is presented in Figure 4.1 and the microwave pulse is radiated by a point radiator located at $x = 0$ cm, $y = 5$ cm. When the TA signal is generated, it is captured on the FEM nodes along the concave contour. The captured TA signal is stored and processed as shown in the acoustic detector in Figure 2.3. The captured TA signal is added with white Gaussian noise, so that the signal-to-noise ratio equals 10 dB, then the noisy TA signal is filtered with a 2^{nd} order Butterworth bandpass filter between 20 kHz and 2 MHz.

Figure 4.3 shows the captured TA signal at 5 acoustic detector locations labeled A, B, C, D, and E of three target positions shown in Figure 4.2(a)-(c). The peaks of TA signal at the detector locations can be shown in Table 4.3. It can be seen that the peak positions of TA signal at different detector locations occur at the time that

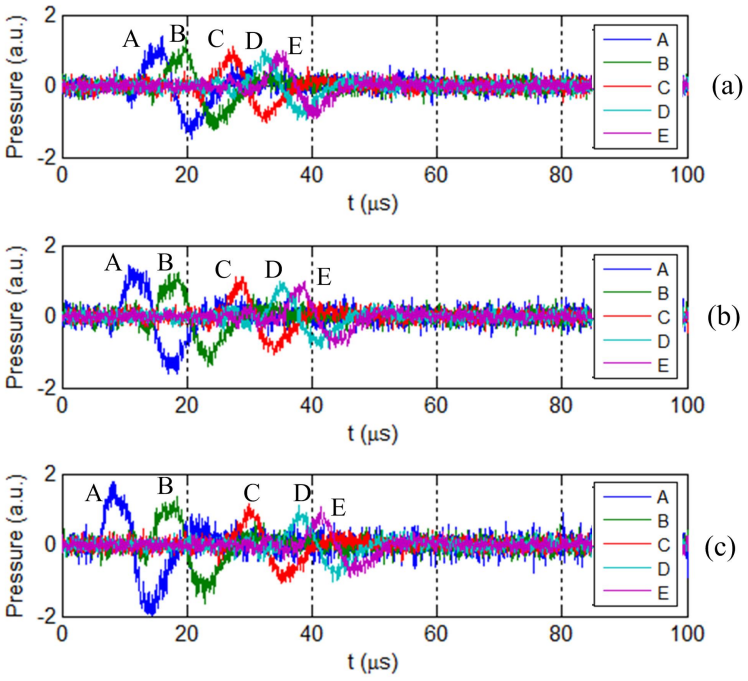

Figure 4.3: Thermo-acoustic signals of biological tissue excited by modulated Gaussian pulse and detected by concave array detector for a target located at: (a) $y = 1.5$ cm, (b) $y = 2.0$ cm, and (c) $y = 2.5$ cm.

Table 4.3: Peak positions of captured TA signals of biological tissue excited by modulated Gaussian pulse and detected by concave array detector with variation of target position.

	Peak position (μs) at detector				
Target position	A	B	C	D	E
$x = 0$ cm, $y = 1.5$ cm	14.92	19.80	27.00	32.32	34.48
$x = 0$ cm, $y = 2.0$ cm	11.64	18.64	28.36	36.12	38.12
$x = 0$ cm, $y = 2.5$ cm	8.32	18.00	30.90	37.80	41.40

agree to the time of TA signal propagation form target to detector. For example, the distances of the target located at $y = 1.5$ cm, 2.0 cm, and 2.5 cm to the detector A are 2.3 cm, 1.8 cm, and 1.3 cm, respectively. The corresponding calculated traveling

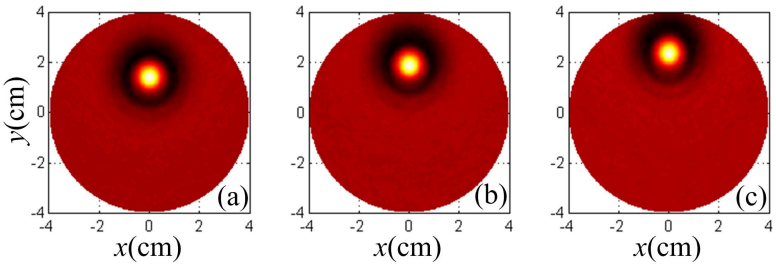

Figure 4.4: Reconstructed images of biological tissue excited by modulated Gaussian pulse and detected by concave array detector for a target located at: (a) $y = 1.5$ cm, (b) $y = 2.0$ cm, and (c) $y = 2.5$ cm.

time are 15.33 μs, 12.00 μs, and 8.67 μs while the captured TA signal occurred their peak at 14.92 μs, 11.64 μs, 8.92 μs, respectively. The relative peak level of TA signal shown in Figure 4.3(a)-(c) is a little different because the target dimension is the same at 5 mm radius. However, the difference can be noticeable on the captured TA signal at detector A because the closer distance produces a stronger signal. Figure 4.4(a)-(c) shows the reconstructed images for different target positions at $y = 1.5$ cm, 2.0 cm, and 2.5 cm, respectively. The images show the correct target position corresponding to the original tissue structure.

4.2.2 Variation of target dimensions

Figure 4.5 shows the geometries and their corresponding FEM meshes for the simulations of TA signal generated by various target dimensions with concave array detector. The geometry of the biological tissue with a target radius of 3 mm located at $x = 0$ cm, $y = 2$ cm and its corresponding FEM mesh can be shown in Figure 4.5(a) and (d), respectively. The geometry of the biological tissue with a target radius of 5 mm located at $x = 0$ cm, $y = 2$ cm and its corresponding FEM mesh can be shown in Figure 4.5(b) and (e), respectively. The geometry of the biological tissue with target radius of 7 mm located at $x = 0$ cm, $y = 2$ cm and its corresponding FEM mesh can be shown in Figure 4.5(c) and (f), respectively.

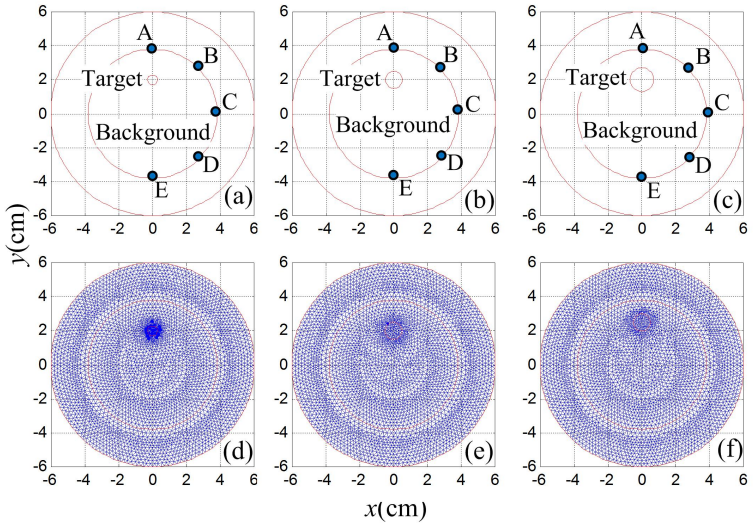

Figure 4.5: Geometries and FEM meshes of biological tissue with concave array detector and a target radius of: (a) 3 mm, (b) 5 mm, (c) 7 mm. (d),(e), and (f) show the corresponding FEM meshes of geometry in (a), (b), and (c), respectively.

The dielectric and acoustic properties of each region in the biological tissues for the simulation is presented in Table 4.1 and Table 4.2, respectively. The microwave pulse excitation in each geometry is presented in Figure 4.1 in which the point for the pulse radiation is located at $x = 0$ cm, $y = 5$ cm. When the TA signal is generated, it is captured on the FEM nodes along the concave contour. The captured TA signal is stored and processed as shown in the acoustic detector in Figure 2.3. The captured TA signal is added with white Gaussian noise, so that the signal-to-noise ratio equals 10 dB, then the noisy TA signal is filtered with a 2^{nd} order Butterworth bandpass filter between 20 kHz and 2 MHz.

Figure 4.6 shows the captured TA signal at 5 acoustic detector locations labeled A, B, C, D, and E of three target radius shown in Figure 4.5(a)-(c). The peaks of TA signal at the detector locations can be shown in Table 4.4. It can be seen that the peak position of TA signal at different detector locations occur at the time that agree to the time of TA signal propagation from target to detector. In this case, the target

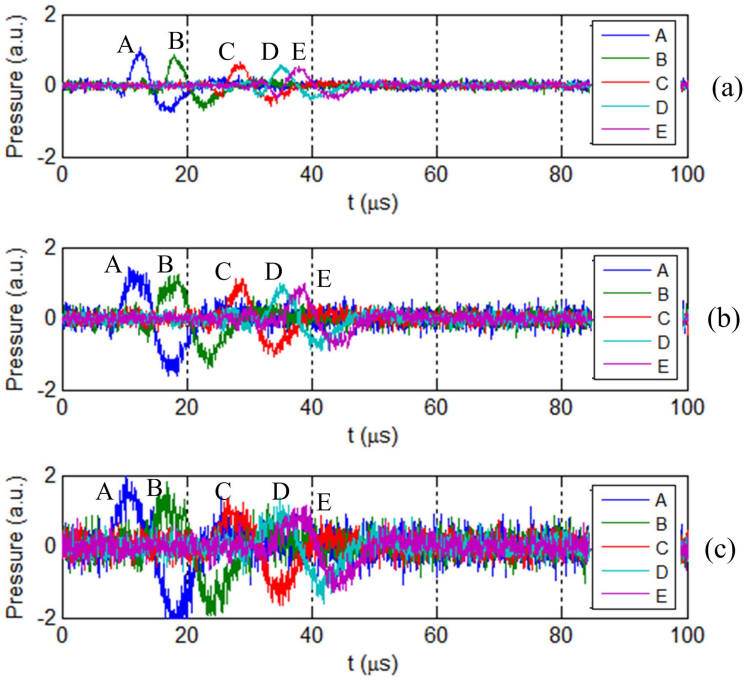

Figure 4.6: Thermo-acoustic signals of biological tissue excited by modulated Gaussian pulse and detected by concave array detector for a target radius of: (a) 3 mm, (b) 5 mm, and (c) 7 mm.

Table 4.4: Peak positions of captured TA signals of biological tissue excited by modulated Gaussian pulse and detected by concave array detector with variation of target dimension.

	Peak position (μs) at detector				
Target radius	A	B	C	D	E
3 mm	12.91	17.84	28.28	35.42	37.88
5 mm	11.64	18.64	28.36	36.12	38.12
7 mm	11.44	15.76	26.28	33.48	38.28

dimension is varied while the position of target is fixed at $x = 0$ cm, $y = 2.0$ cm. The peak positions of TA signal for three dimension cases occur at about the same position. The peak level of captured TA signal is clearly seen that it is proportional

to the dimension of target. The small target produced smaller amplitude of TA signal than the bigger target. Figure 4.7(a)-(c) show the reconstructed image for different target dimensions of radius of 3 mm, 5 mm, and 7 mm, respectively. The images show their corresponding target dimension to the original structure.

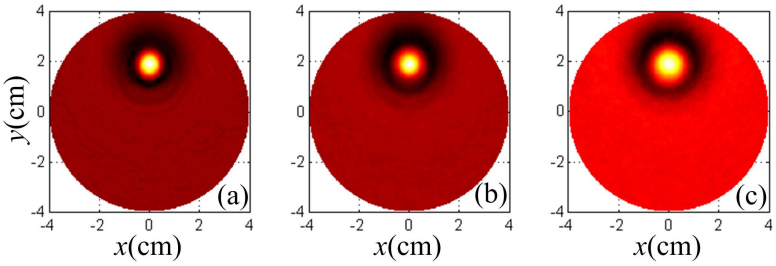

Figure 4.7: Reconstructed images of biological tissue excited by modulated Gaussian pulse and detected by concave array detector for a target radius of: (a) 3 mm, (b) 5 mm, and (c) 7 mm.

4.2.3 Variation of target numbers

Figure. 4.8 shows the geometries and their corresponding FEM meshes for the simulations of TA signal generated by various target numbers with concave array detector. The geometry of the biological tissue with one target and its corresponding FEM mesh can be shown in Figure 4.8(a) and (d), respectively. The geometry of the biological tissue with two targets and its corresponding FEM mesh can be shown in Figure 4.8(b) and (e), respectively. The geometry of the biological tissue with three targets and its corresponding FEM mesh can be shown in Figure 4.8(c) and (f), respectively.

The dielectric and acoustic properties of each region in the biological tissues for the simulation is presented in Table 4.1 and Table 4.2, respectively. The microwave pulse excitation in each geometry is presented in Figure 4.1 in which the point for the pulse radiation is located at $x = 0$ cm, $y = 5$ cm. When the TA signal is generated, it is captured on the FEM nodes along the concave contour. The captured TA signal

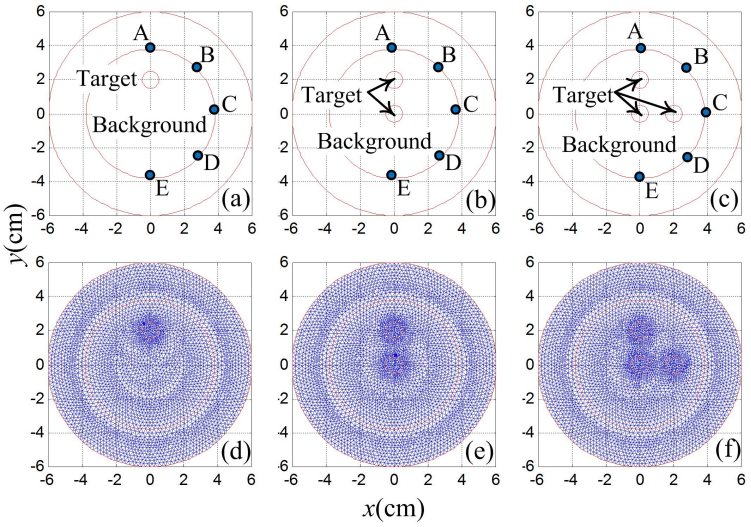

Figure 4.8: Geometries and FEM meshes of biological tissue with concave array detector and: (a) one target, (b) two targets, (c) three targets. (d),(e), and (f) show the corresponding FEM meshes of geometry in (a), (b), and (c), respectively.

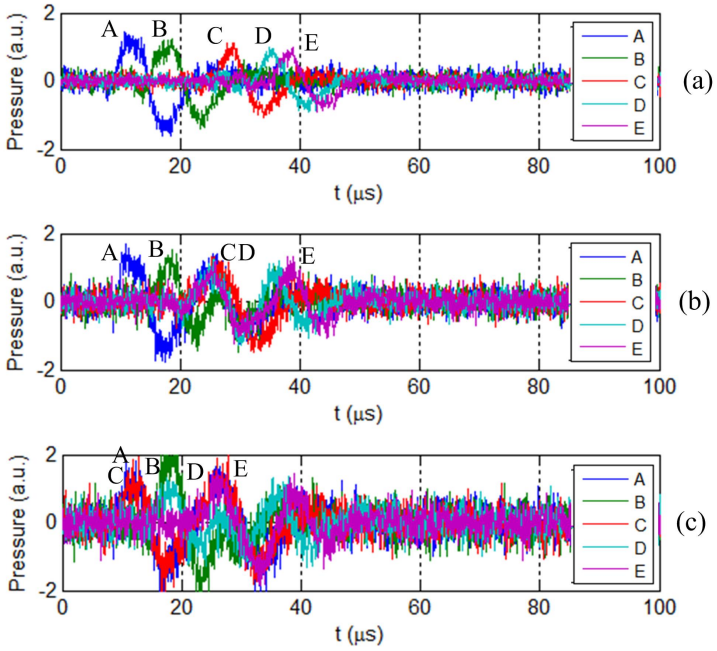

Figure 4.9: Thermo-acoustic signals of biological tissue excited by modulated Gaussian pulse and detected by concave array detector for: (a) one target, (b) two targets, and (c) three targets.

is stored and processed as shown in the acoustic detector in Figure 2.3. The captured TA signal is added with white Gaussian noise, so that the signal-to-noise ratio equals 10 dB, then the noisy TA signal is filtered with a 2nd order Butterworth bandpass filter between 20 kHz and 2 MHz.

Table 4.5: Peak positions of captured TA signals of biological tissue excited by modulated Gaussian pulse and detected by concave array detector with variation of target number.

	Peak position (μs) at detector				
Target number	A	B	C	D	E
one target	11.64	18.64	28.36	36.12	38.12
two targets	13.04	18.12	25.28	25.32	38.24
three targets	10.56	18.36	12.34	18.76	26.92

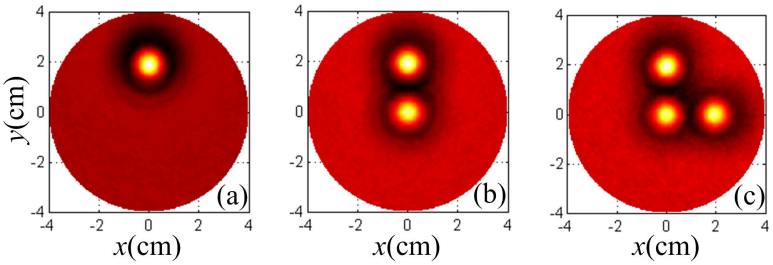

Figure 4.10: Reconstructed images of biological tissue excited by modulated Gaussian pulse and detected by concave array detector for: (a) one target, (b) two targets, and (c) three targets.

Figure 4.9 shows the captured TA signal at 5 acoustic detector locations labeled A, B, C, D, and E of three geometries of different target number shown in Figure 4.8(a)-(c). The peaks of TA signal at the detector locations can be shown in Table 4.5. It can be assumed that TA signal generated by two or three targets is the superposition between TA signal generated by each target. The peak position of TA signal is

then the peak of the summation of TA signal generated by each target. The level of TA signal in Figure 4.9(c) is bigger than the signal in (b) and (a) because there are more targets in which the electric field energy is absorbed more energy in the tissue. Figure 4.10(a)-(c) show the reconstructed image for different target number with one target, two targets and three targets, respectively. The images show the reconstructed targets that agrees in both number and position of the target in the original geometries.

4.3 Thermo-Acoustic Signal Generation and Image Reconstruction in Convex Array Case

This section describes the solution of TA signal generated in the biological tissue with a convex array detector. The dielectric properties for the simulation in convex case can be shown in Table 4.6 and the acoustic properties for all biological tissue regions can be shown in Table 4.2. The simulation results for the generation of TA signal in various target positions, dimensions, and numbers are presented in the following subsections.

Table 4.6: Dielectric properties of biological tissue at 915 MHz for simulations in convex array case [24].

Dielectric Properties	Symbol	Value	Unit
Electrical Conductivity	σ	1.216, 0.608*	S/m
Relative Permittivity	ε_r	60.5	1

* for target region

4.3.1 Variation of target positions

Figure. 4.11 shows the geometries and their corresponding FEM meshes for the simulations of TA signal generated by various target positions with convex array detector.

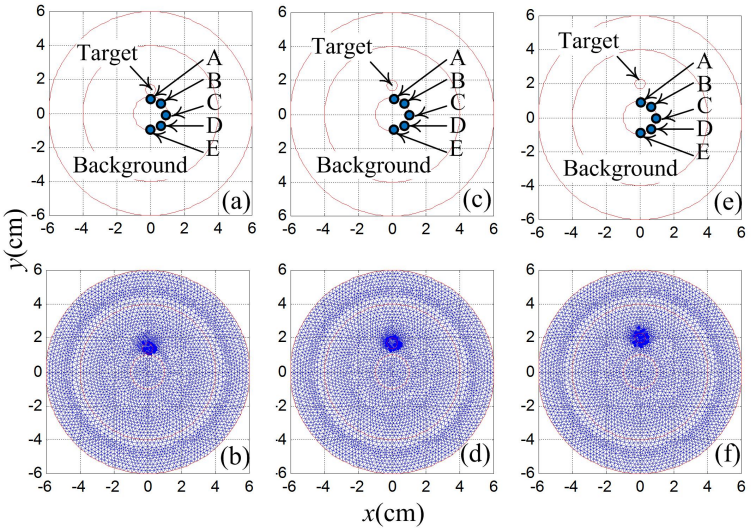

Figure 4.11: Geometries and FEM meshes of biological tissue with convex array detector and a target located at: (a) $y = 1.4$ cm, (b) $y = 1.7$ cm, (c) $y = 2.0$ cm. (d),(e), and (f) show the corresponding FEM meshes of geometry in (a), (b), and (c), respectively.

The geometry of the biological tissue with a 3 mm radius target located at $x = 0$ cm, $y = 1.4$ cm and its corresponding FEM mesh can be shown in Figure 4.11(a) and (d), respectively. The geometry of the biological tissue with a 3 mm radius target located at $x = 0$ cm, $y = 1.7$ cm and its corresponding FEM mesh can be shown in Figure 4.11(b) and (e), respectively. The geometry of the biological tissue with a 3 mm radius target located at $x = 0$ cm, $y = 2.0$ cm and its corresponding FEM mesh can be shown in Figure 4.11(c) and (f), respectively.

The dielectric and acoustic properties of each region in the biological tissues for the simulation is presented in Table 4.6 and Table 4.2, respectively. The microwave pulse excitation in each geometry is presented in Figure 4.1 in which the point for the pulse radiation is located at $x = 0$ cm, $y = 0$ cm. When the TA signal is generated, it is captured on the FEM nodes along the convex contour. The captured TA signal is stored and processed as shown in the acoustic detector in Figure 2.3. The captured

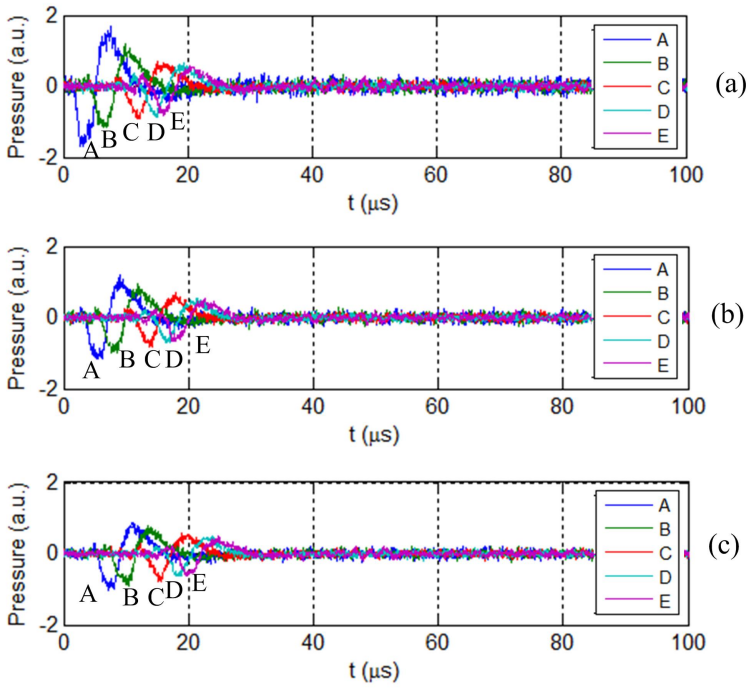

Figure 4.12: Thermo-acoustic signals of biological tissue excited by modulated Gaussian pulse and detected by convex array detector for a target located at: (a) y = 1.4 cm, (b) y = 1.7 cm, and (c) y = 2.0 cm.

Table 4.7: Negative peak positions of captured TA signals of biological tissue excited by modulated Gaussian pulse and detected by convex array detector with variation of target position.

	Negative peak position (μs) at detector				
Target position	A	B	C	D	E
x = 0 cm, y = 1.4 cm	2.88	7.04	12.24	14.88	16.00
x = 0 cm, y = 1.7 cm	6.00	8.36	14.32	16.40	17.92
x = 0 cm, y = 2.0 cm	7.84	10.12	15.56	18.52	19.64

TA signal is added with white Gaussian noise, so that the signal-to-noise ratio equals 10 dB, then the noisy TA signal is filtered with a 2^{nd} order Butterworth bandpass filter between 20 kHz and 2 MHz.

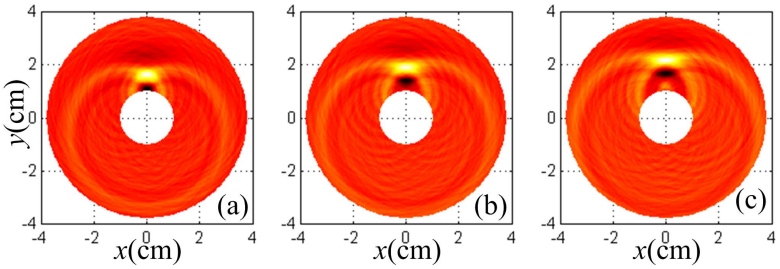

Figure 4.13: Reconstructed images of biological tissue excited by modulated Gaussian pulse and detected by convex array detector for a target located at: (a) $y = 1.4$ cm, (b) $y = 1.7$ cm, and (c) $y = 2.0$ cm.

Figure 4.12 shows the captured TA signal at 5 acoustic detector locations labeled A, B, C, D, and E of three target positions shown in Figure 4.11(a)-(c). In convex case, the electrical conductivity of target is lower than the conductivity of background as shown in Table 4.6. This characteristic causes the generated TA signal to be out of phase compared with the concave case. The negative peaks of TA signal at the detector locations will be presented and can be shown in Table 4.7. It can be seen that the negative peak positions of TA signal at different detector locations occur at the time that agree to the time of TA signal propagation form target to detector. For example, the distances of the target located at $y = 1.4$ cm, 1.7 cm, and 2.0 cm to the detector A are 0.4 cm, 0.7 cm, and 1.0 cm, respectively. The corresponding calculated traveling time are 2.67 μs, 4.67 μs, and 6.67 μs while the captured TA signal occurred their negative peak at 2.88 μs, 6.00 μs, 7.84 μs, respectively. The relative negative peak level of TA signal shown in Figure 4.3(a)-(c) is different because the closer distance produces a stronger signal. Figure 4.13(a)-(c) show the reconstructed images for different target positions at $y = 1.4$ cm, 1.7 cm, and 2.0 cm, respectively. The images show the reconstructed target position that agrees with the original target position. However, there are artifacts of "spreading" and "wings" on reconstructed target. The artifact trends to have more spreading for longer target distance.

4.3.2 Variation of target dimensions

Figure. 4.14 shows the geometries and their corresponding FEM meshes for the simulations of TA signal generated by various target dimensions with convex array detector. The geometry of the biological tissue with a target radius of 3 mm located at $x = 0$ cm, $y = 1.7$ cm and its corresponding FEM mesh can be shown in Figure 4.14(a) and (d), respectively. The geometry of the biological tissue with a target radius of 4 mm located at $x = 0$ cm, $y = 1.7$ cm and its corresponding FEM mesh can be shown in Figure 4.14(b) and (e), respectively. The geometry of the biological tissue with a target radius of 5 mm located at $x = 0$ cm, $y = 1.7$ cm and its corresponding FEM mesh can be shown in Figure 4.5(c) and (f), respectively.

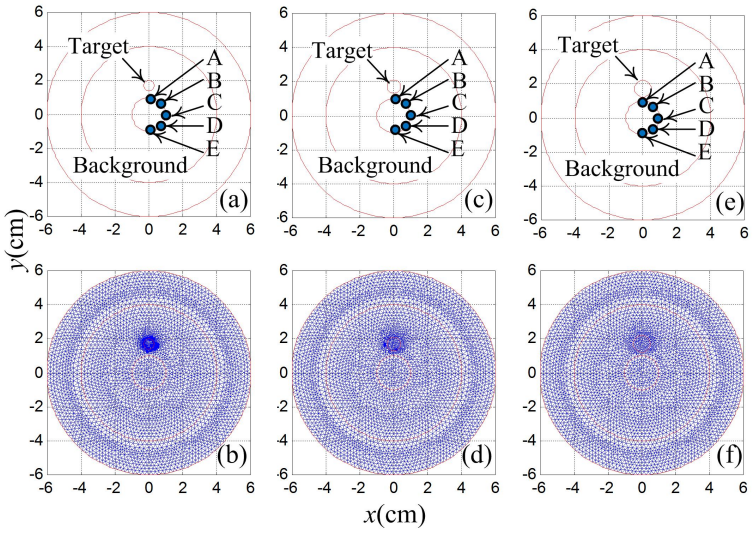

Figure 4.14: Geometries and FEM meshes of biological tissue with convex array detector and a target radius of: (a) 3 mm, (b) 4 mm, (c) 5 mm. (d),(e), and (f) show the corresponding FEM meshes of geometry in (a), (b), and (c), respectively.

The dielectric and acoustic properties of each region in the biological tissues for the simulation is presented in Table 4.6 and Table 4.2, respectively. The microwave pulse excitation in each geometry is presented in Figure 4.1 in which the point for the pulse radiation is located at $x = 0$ cm, $y = 0$ cm. When the TA signal is generated,

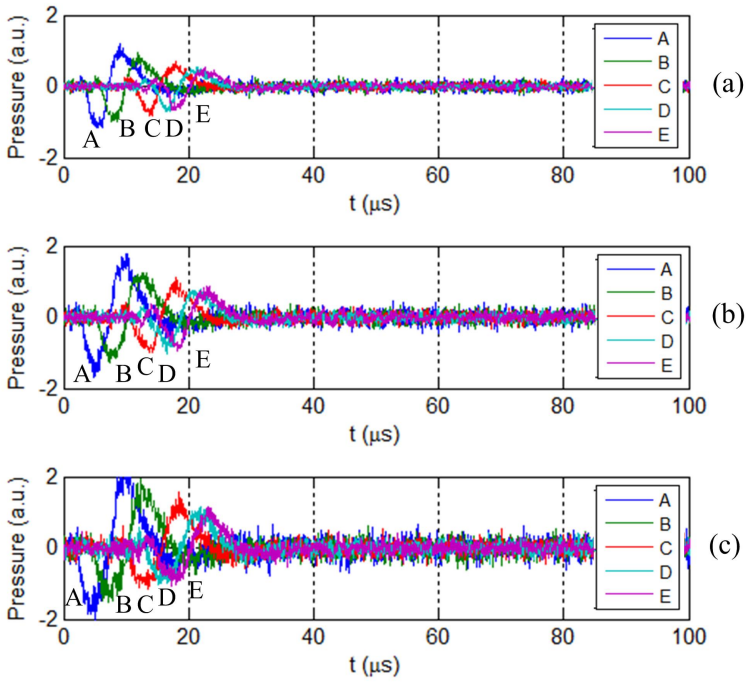

Figure 4.15: Thermo-acoustic signals of biological tissue excited by modulated Gaussian pulse and detected by convex array detector for a target radius of: (a) 3 mm, (b) 4 mm, and (c) 5 mm.

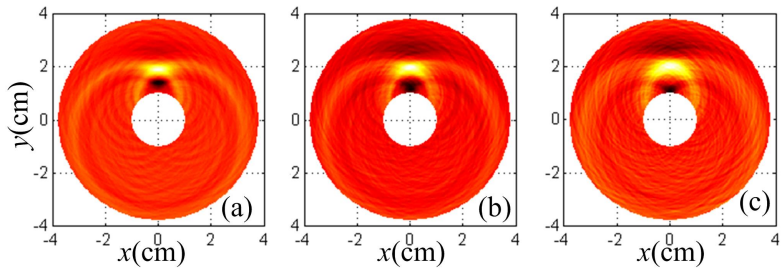

Figure 4.16: Reconstructed images of biological tissue excited by modulated Gaussian pulse and detected by convex array detector for a target radius of: (a) 3 mm, (b) 4 mm, and (c) 5 mm.

it is captured on the FEM nodes along the convex contour. The captured TA signal is stored and processed as shown in the acoustic detector in Figure 2.3. The captured TA signal is added with white Gaussian noise, so that the signal-to-noise ratio equals 10 dB, then the noisy TA signal is filtered with a 2^{nd} order Butterworth bandpass

Table 4.8: Negative peak positions of captured TA signals of biological tissue excited by modulated Gaussian pulse and detected by convex array detector with variation of target dimension.

	Negative peak position (μs) at detector				
Target radius	A	B	C	D	E
3 mm	6.00	8.36	14.32	16.40	17.92
4 mm	5.28	7.64	14.28	16.96	18.52
5 mm	3.52	6.52	11.72	15.48	18.04

filter between 20 kHz and 2 MHz.

Figure 4.15 shows the captured TA signal at 5 acoustic detector locations labeled A, B, C, D, and E of three target radius shown in Figure 4.14(a)-(c). The negative peak position on each detector can be shown in Table 4.8. In this case, the target position is fixed at $x = 0$ cm, $y = 1.7$ cm while the dimension is varied. It can be noticed that the larger target dimension produces the stronger TA signal level. Figure 4.16(a)-(c) shows the reconstructed image for different target dimensions of radius of 3 mm, 4 mm, and 5 mm, respectively. The shape and the dimension of target distorted from their original shape and dimension because of the effect of convex detection geometry. However, the reconstructed images show the correct position of the target position and the relative dimension agree with the original dimension.

4.3.3 Variation of target numbers

Figure. 4.17 shows the geometries and their corresponding FEM meshes for the simulations of TA signal generated by various target numbers with convex array detector. The geometry of the biological tissue with one target and its corresponding FEM mesh can be shown in Figure 4.17(a) and (d), respectively. The geometry of the biological tissue with two targets and its corresponding FEM mesh can be shown in

Figure 4.17(b) and (e), respectively. The geometry of the biological tissue with three targets and its corresponding FEM mesh can be shown in Figure 4.17(c) and (f), respectively.

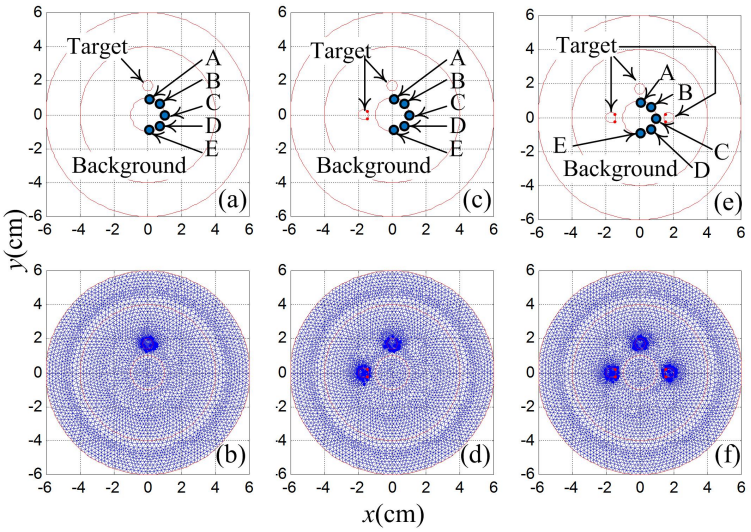

Figure 4.17: Geometries and FEM meshes of biological tissue with convex array detector and: (a) one target, (b) two targets, (c) three targets. (d),(e), and (f) show the corresponding FEM meshes of geometry in (a), (b), and (c), respectively.

Table 4.9: Negative peak positions of captured TA signals of biological tissue excited by modulated Gaussian pulse and detected by convex array detector with variation of target number.

	Negative peak position (μs) at detector				
Target number	A	B	C	D	E
one target	6.00	8.36	14.32	16.40	17.92
two targets	5.80	8.08	13.24	16.92	13.72
three targets	13.68	8.84	6.28	16.92	14.00

The dielectric and acoustic properties of each region in the biological tissues for the simulation is presented in Table 4.6 and Table 4.2, respectively. The microwave

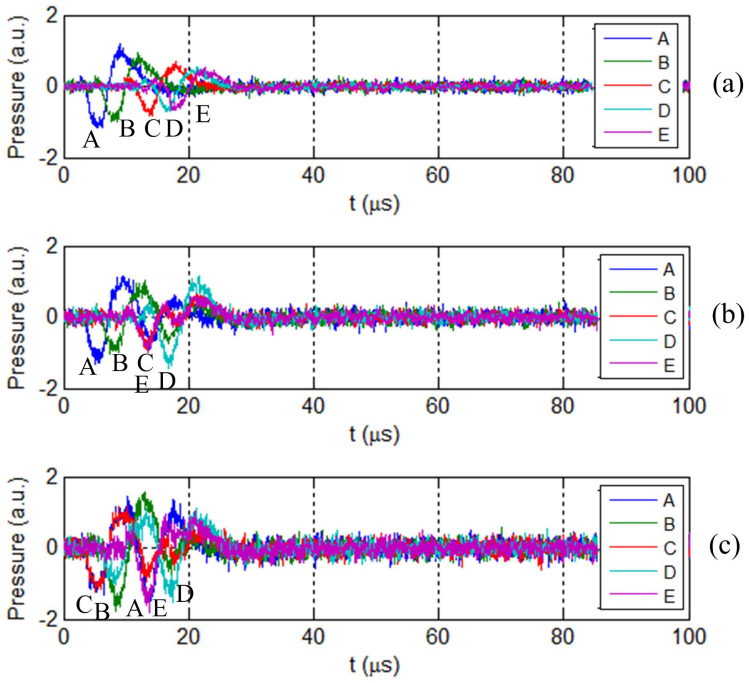

Figure 4.18: Thermo-acoustic signals of biological tissue excited by modulated Gaussian pulse and detected by convex array detector for: (a) one target, (b) two targets, and (c) three targets.

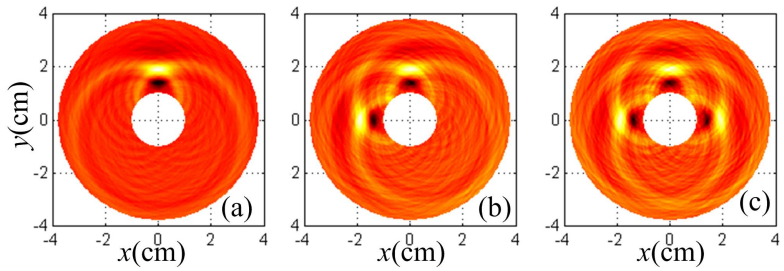

Figure 4.19: Reconstructed images of biological tissue excited by modulated Gaussian pulse and detected by convex array detector for: (a) one target, (b) two targets, and (c) three targets.

pulse excitation in each geometry is presented in Figure 4.1 in which the point for the pulse radiation is located at $x = 0$ cm, $y = 0$ cm. When the TA signal is generated, it is captured on the FEM nodes along the convex contour. The captured TA signal is stored and processed as shown in the acoustic detector in Figure 2.3. The captured

TA signal is added with white Gaussian noise, so that the signal-to-noise ratio equals 10 dB, then the noisy TA signal is filtered with a 2^{nd} order Butterworth bandpass filter between 20 kHz and 2 MHz.

Figure 4.18 shows the captured TA signal at 5 acoustic detector locations labeled A, B, C, D, and E of three geometries of different target number shown in Figure 4.17(a)-(c). The captured TA signal is the superposition between TA signal generated by each target. Then the peak position of TA signal is the peak of the summation of all TA signals. The peak level of TA signal in Figure 4.9(c) is bigger than the signal in (b) and (a) because there are more number of targets in Figure 4.9(c) in which the tissue absorbs more electric field energy. Figure 4.19(a)-(c) show the reconstructed image for different target number with one target, two targets and three targets, respectively.

4.4 Discussion

In this chapter, the modulated Gaussian pulse was used to excite the biological tissue to generate the TA signal in various geometries. For the concave case, the solutions of calculated TA signal were presented in Figure 4.3 for variation of target positions, Figure 4.6 for variation of target dimensions, and Figure 4.9 for variation of target numbers, in which the solutions of reconstructed images to each one were presented in Figure 4.4, Figure 4.7, and Figure 4.10, respectively. For the convex case, the solutions of calculated TA signal were presented in Figure 4.12 for variation of target positions, Figure 4.15 for variation of target dimensions, and Figure 4.18 for variation of target numbers, in which the solutions of reconstructed images to each one were presented in Figure 4.13, Figure 4.16, and Figure 4.19, respectively.

In concave case, the induced TA signals were reasonable agreed with the characteristic of acoustic propagation in the biological tissue. For example, Figure 4.3(c) showed the peak of TA signal at detector A in which the peak of the signal occurred

before those of the peaks of the signal detected at the same detector in Figure 4.3(b) and (a), respectively. The reason of this effect was that the position of the target associated the TA signal in Figure 4.3(c) was closer to the detector than the target associated the TA signal in Figure 4.3(b) and (a), respectively. Another example was that the TA signal can be compared in peak level which was shown in Figure 4.6(a)-(c). The TA signal generated in the geometry that has a bigger target dimension had higher peak amplitude than those for smaller targets. However, it can be noticed that the TA signal at detector A in Figure 4.6(c) was slightly happened before than those in Figure 4.6(b) and (a). This effect was because the slightly shorter distance from the edge of target to the detector A due to the bigger target radius.

In convex case, the induced TA signals shown in Figure 4.12, 4.15, and 4.18 were out of phase when were compared with the corresponding TA signals for concave case. This effect was reasonable and caused from the truth that the electrical conductivity σ of target was lower than that of background as shown in Table 4.6. Moreover, the TA signals were also reasonable agreed with the characteristic of acoustic propagation in biological tissue. The artifacts of reconstructed images can be noticed as shown in Figure 4.13, 4.16, and 4.19 for the convex case. These artifacts of "spreading" and "wings" happened on the reconstructed images around target will be discussed in detail in Chapter 6.

4.5 Summary

This chapter presented the numerical solutions for the generated TA signal when the conventional microwave pulse, a modulated Gaussian pulse, was applied as a microwave pulse excitation for microwave-induced thermo-acoustic tomography for biological tissue imaging in both concave and convex array detection and in various geometries of different target position, target dimensions, and target numbers. The corresponding reconstructed images using the back-projection algorithm were

depicted to show the ability of the time-domain numerical analysis for the problem of microwave-induced thermo-acoustic tomography with the modulated Gaussian pulse excitation. The results of generated TA signal reasonably agreed with the characteristic of acoustic propagation in the tissue.

CHAPTER 5

THERMO-ACOUSTIC SIGNAL GENERATION AND IMAGE RECONSTRUCTION USING MODULATED CHIRP PULSE

5.1 Introduction

This chapter describes the numerical solutions of TA signal generation in medium of biological tissue properties and their image reconstruction using the step depicted in Figure 3.1. In this numerical simulation, the TDFEM formulation that was described in Chapter 3 is applied to calculate the TA signal response where the proposed microwave pulse (modulated chirp pulse) is adopted as an alternative EM pulse excitation. When the TA signal is numerically generated, it is captured along the detector locations represented the concave and convex array which can be shown in Figure 1.3. The imaging domain is inside the contour of array in the concave case while the imaging domain is outside the contour of array for the convex case. After the captured TA signal at each position of detector is stored, it is used to reconstruct the image represented the EM absorption distribution using the inverse step described in Section 2.4.

A normalized chirp pulse, shown in Figure 5.1(a), with the pulse period of 200 μs, the chirp time of 100 μs, the starting and stopping frequencies of 20 kHz and 100 kHz, respectively, is modulated with a carrier frequency of 915 MHz to form a modulated chirp pulse as shown in Figure 5.1(b). This modulated chirp pulse is applied as the

microwave pulse excitation for TA signal generation. The simulation is performed in concave and convex array cases. Each case is divided into different geometries of various target positions, target dimensions and target numbers.

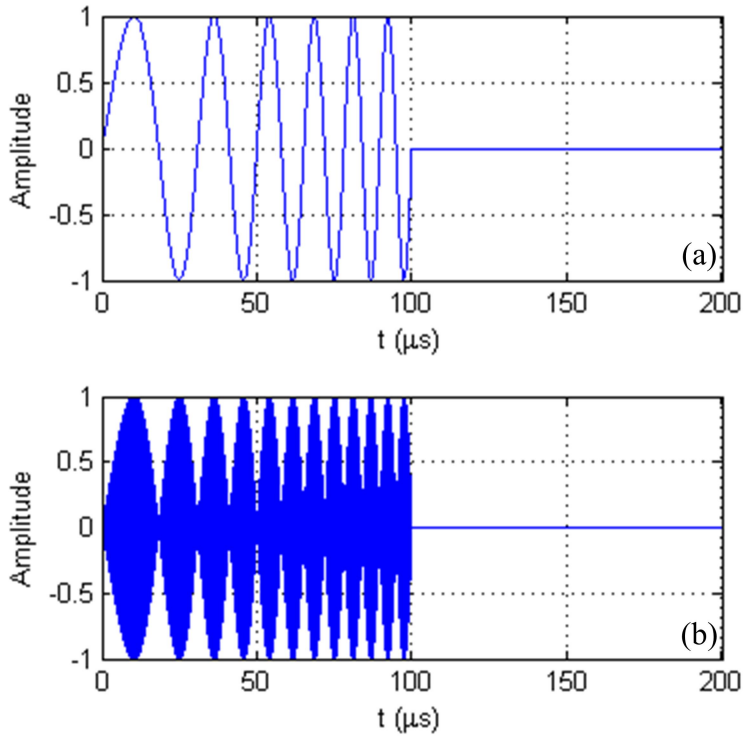

Figure 5.1: (a) Chirp pulse and (b) modulated chirp pulse.

5.2 Thermo-Acoustic Signal Generation and Image Reconstruction in Concave Array Case

5.2.1 Variation of target positions

In this subsection, the numerical solution of TA signal generation in biological tissue with the modulated chirp pulse, as shown in Figure 5.1, and with the concave array detection is described. The dielectric properties of the biological tissue for the concave array detection case are presented in Table 4.1 and the acoustic properties of the tissue are presented Table 4.2. In this simulation, the position of a 5 mm radius target is

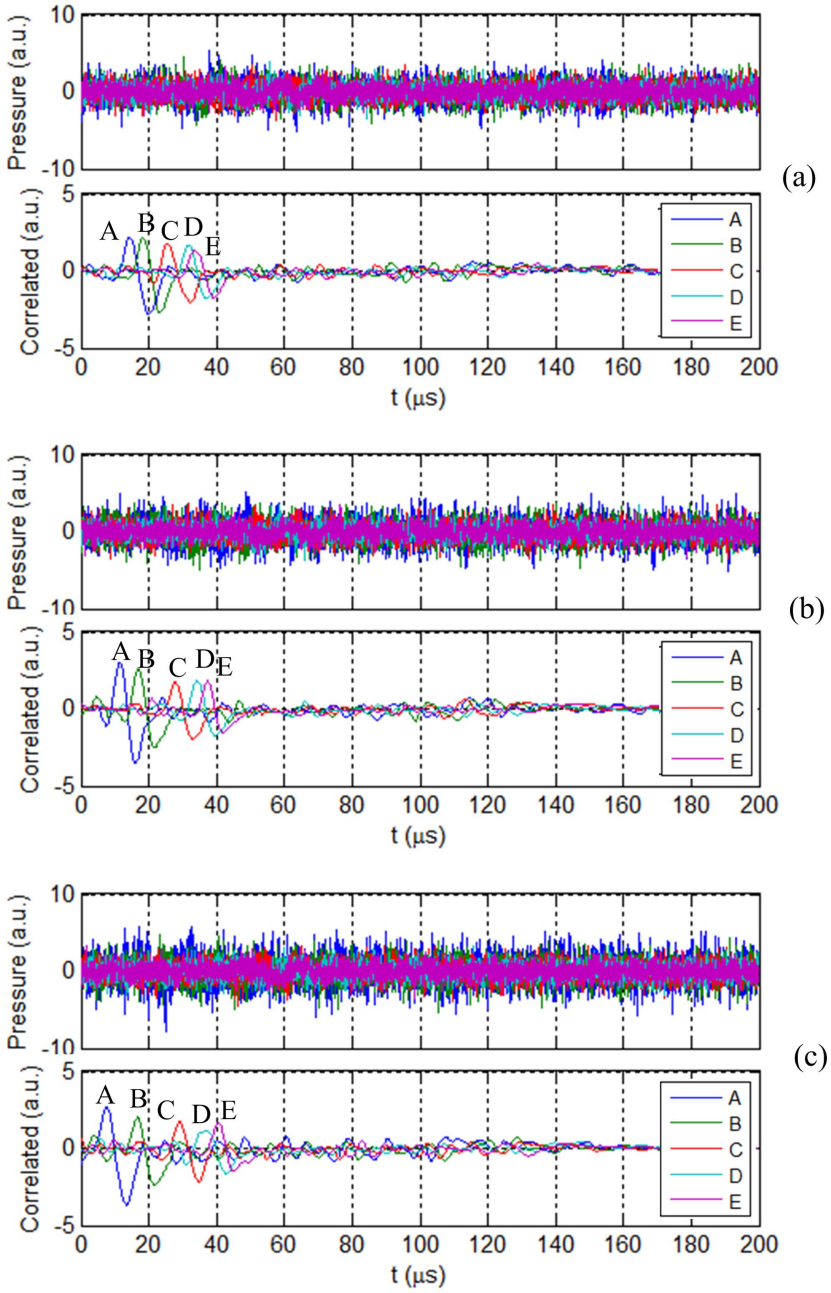

Figure 5.2: Thermo-acoustic signals and their corresponding correlated signals of biological tissue excited by modulated chirp pulse and detected by concave array detector for a target located at: (a) $y = 1.5$ cm, (b) $y = 2.0$ cm, and (c) $y = 2.5$ cm.

varied along the vertical axis at $y = 1.5$ cm, 2.0 cm, and 2.5 cm. The geometries and their corresponding FEM meshes for the simulation was illustrated in Figure 4.2. The location of a point radiation of the modulated chirp pulse is fixed and located at $x = 0$ cm, $y = 5$ cm. The results of captured TA signals and the correlated TA signals are presented in Figure 5.2 and their corresponding reconstructed images are presented in Figure 5.3.

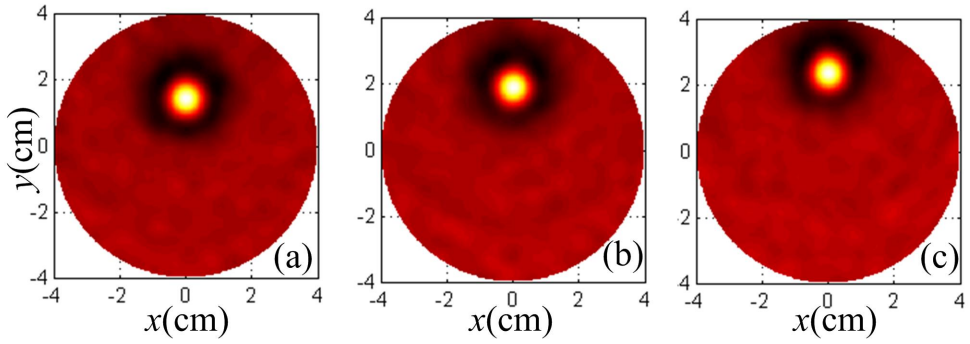

Figure 5.3: Reconstructed images of biological tissue excited by modulated chirp pulse and detected by concave array detector for a target located at: (a) $y = 1.5$ cm, (b) $y = 2.0$ cm, and (c) $y = 2.5$ cm.

Table 5.1: Peak positions of correlated TA signals of biological tissue excited by modulated chirp pulse and detected by concave array detector with variation of target position.

	Peak position (μs) at detector				
Target position	A	B	C	D	E
$x = 0$ cm, $y = 1.5$ cm	14.20	18.04	25.90	31.44	34.40
$x = 0$ cm, $y = 2.0$ cm	11.28	17.08	27.64	34.52	36.68
$x = 0$ cm, $y = 2.5$ cm	8.28	16.64	29.60	37.00	40.68

The peak positions of the correlated TA signals presented in Figure 5.2 at detector labeled A, B, C, D, and E for three target positions can be shown in Table 5.1. The peak of correlated signals agree with the peak of TA signals that generated using the modulated Gaussian pulse. The reconstructed images show the reconstructed target position and dimension that agree with their original geometries.

5.2.2 Variation of target dimensions

In this subsection, the numerical solution of TA signal generation in biological tissue with the modulated chirp pulse, as shown in Figure 5.1, and with the concave array detection is described. The dielectric and acoustic properties of the biological tissue for the concave array detection case are presented in Table 4.1 and Table 4.2, respectively. The radius of a target located at $x = 0$ cm, $y = 2$ cm is varied with three different radius of 3 mm, 5 mm, and 7 mm. The geometries and their corresponding FEM meshes for the simulation was illustrated in Figure 4.5. The location of a point radiation of the modulated chirp pulse is fixed and located at $x = 0$ cm, $y = 5$ cm. The results of captured TA signals and the correlated TA signals are presented in Figure 5.4 and their corresponding reconstructed images are presented in Figure 5.5.

Table 5.2: Peak positions of correlated TA signals of biological tissue excited by modulated chirp pulse and detected by concave array detector with variation of target dimension.

	Peak position (μs) at detector				
Target radius	A	B	C	D	E
3 mm	11.36	17.56	27.60	34.56	37.08
5 mm	11.28	17.08	27.64	34.52	36.68
7 mm	9.64	17.96	27.00	33.92	38.90

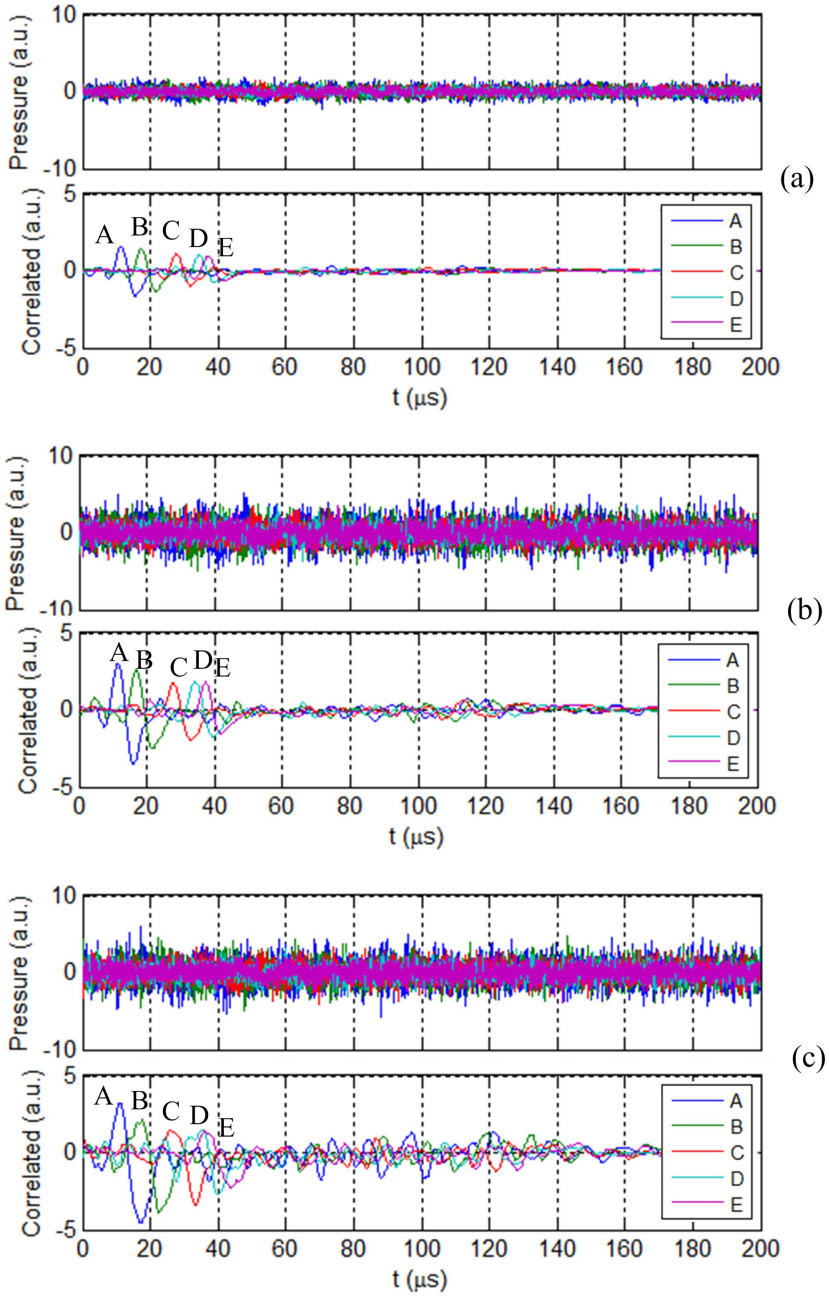

Figure 5.4: Thermo-acoustic signals and their corresponding correlated signals of biological tissue excited by modulated chirp pulse and detected by concave array detector for a target radius of: (a) 3 mm, (b) 5 mm, and (c) 7 mm.

The peak positions of the correlated TA signals presented in Figure 5.4 at detector labeled A, B, C, D, and E for three target positions can be shown in Table 5.2. Since all the targets located at the same position, the peak position of the correlated TA signals are also approximately occurred at same time. It can be noticed that the signal response from the bigger target has a larger amplitude than the smaller target. The reconstructed images show the target position and dimension that relatively agree with their original geometries.

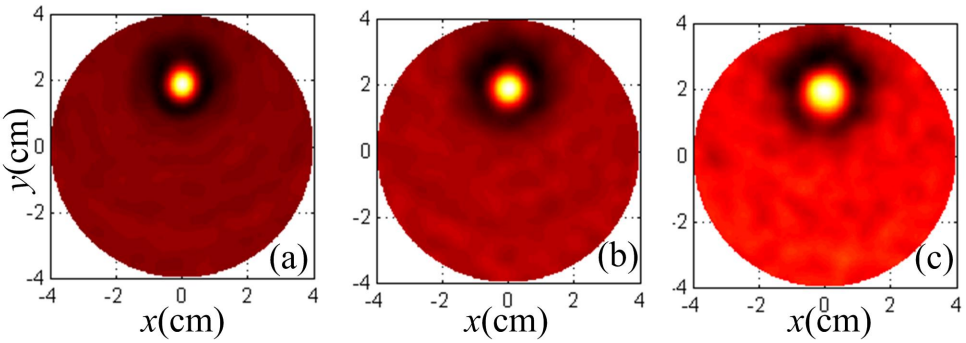

Figure 5.5: Reconstructed images of biological tissue excited by modulated chirp pulse and detected by concave array detector for a target radius of: (a) 3 mm, (b) 5 mm, and (c) 7 mm.

5.2.3 Variation of target numbers

In this subsection, the numerical solution of TA signal generation in biological tissue with the modulated chirp pulse, as shown in Figure 5.1, and with the concave array detection is described. The dielectric and acoustic properties of the biological tissue in concave case are presented in Table 4.1 and Table 4.2, respectively. In this simulation, the number of target is varied from one target to three targets. The location of a point radiation is located at $x = 0$ cm, $y = 5$ cm. The geometries and their corresponding FEM meshes for the simulation was illustrated in Figure 4.8. The results

of captured TA signals and the correlated TA signals are presented in Figure 5.6 and their corresponding reconstructed images are presented in Figure 5.7.

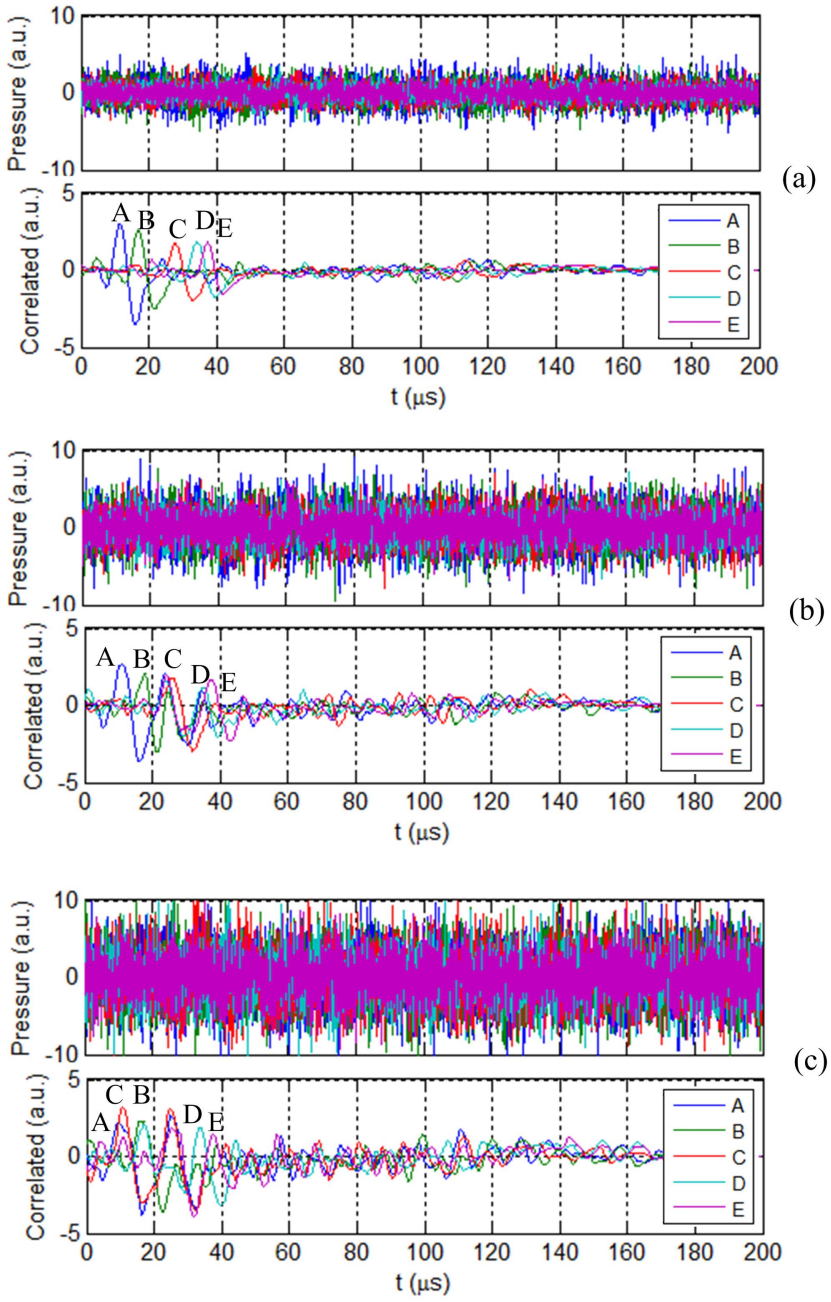

Figure 5.6: Thermo-acoustic signals and their corresponding correlated signals of biological tissue excited by modulated chirp pulse and detected by concave array detector for: (a) one target, (b) two targets, and (c) three targets.

Table 5.3: Peak positions of correlated TA signals of biological tissue excited by modulated chirp pulse and detected by concave array detector with variation of target number.

	Peak position (μs) at detector				
Target number	A	B	C	D	E
one target	11.28	17.08	27.64	34.52	36.68
two targets	11.12	16.96	25.44	24.32	36.24
three targets	10.84	17.16	11.36	16.76	24.08

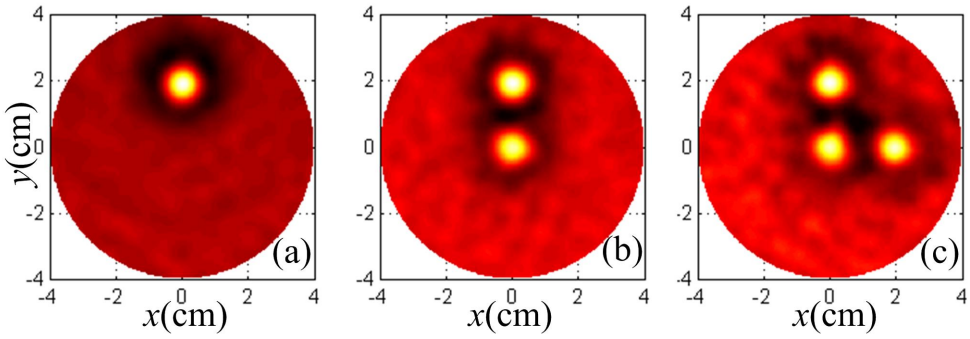

Figure 5.7: Reconstructed images of biological tissue excited by modulated chirp pulse and detected by concave array detector for: (a) one target, (b) two targets, and (c) three targets.

The peak positions of the correlated TA signals presented in Figure 5.6 at detector labeled A, B, C, D, and E for three target positions can be shown in Table 5.3. In case of multiple targets, the captured TA signal at the detector is the summation of generated TA signal contributed by each target. The peaks of correlated TA signal agree with the peaks of captured TA signal when using the modulated Gaussian pulse excitation. The reconstructed images show the reconstructed target position, dimension, and number that relatively agree with their original geometries.

5.3 Thermo-Acoustic Signal Generation and Image Reconstruction in Convex Array Case

5.3.1 Variation of target positions

In this subsection, the numerical solution of TA signal generation in biological tissue with the modulated chirp pulse, as shown in Figure 5.1, and with the convex array detection is described. The dielectric properties of the biological tissue for the convex array detection case are presented in Table 4.6 and the acoustic properties of the tissue are presented Table 4.2. In this simulation, the position of a 3 mm radius target is varied along the vertical axis at $y = 1.4$ cm, 1.7 cm, and 2.0 cm. The geometries and their corresponding FEM meshes for the simulation was illustrated in Figure 4.11. The location of a point radiation of the modulated chirp pulse is fixed and located at $x = 0$ cm, $y = 0$ cm. The results of captured TA signals and the correlated TA signals are presented in Figure 5.8 and their corresponding reconstructed images are presented in Figure 5.9.

Table 5.4: Negative peak positions of correlated TA signals of biological tissue excited by modulated chirp pulse and detected by convex array detector with variation of target position.

	Negative peak position (μs) at detector				
Target position	A	B	C	D	E
$x = 0$ cm, $y = 1.4$ cm	2.44	5.60	11.00	13.96	15.32
$x = 0$ cm, $y = 1.7$ cm	4.36	7.08	12.68	15.68	17.28
$x = 0$ cm, $y = 2.0$ cm	6.40	8.80	14.36	17.68	19.12

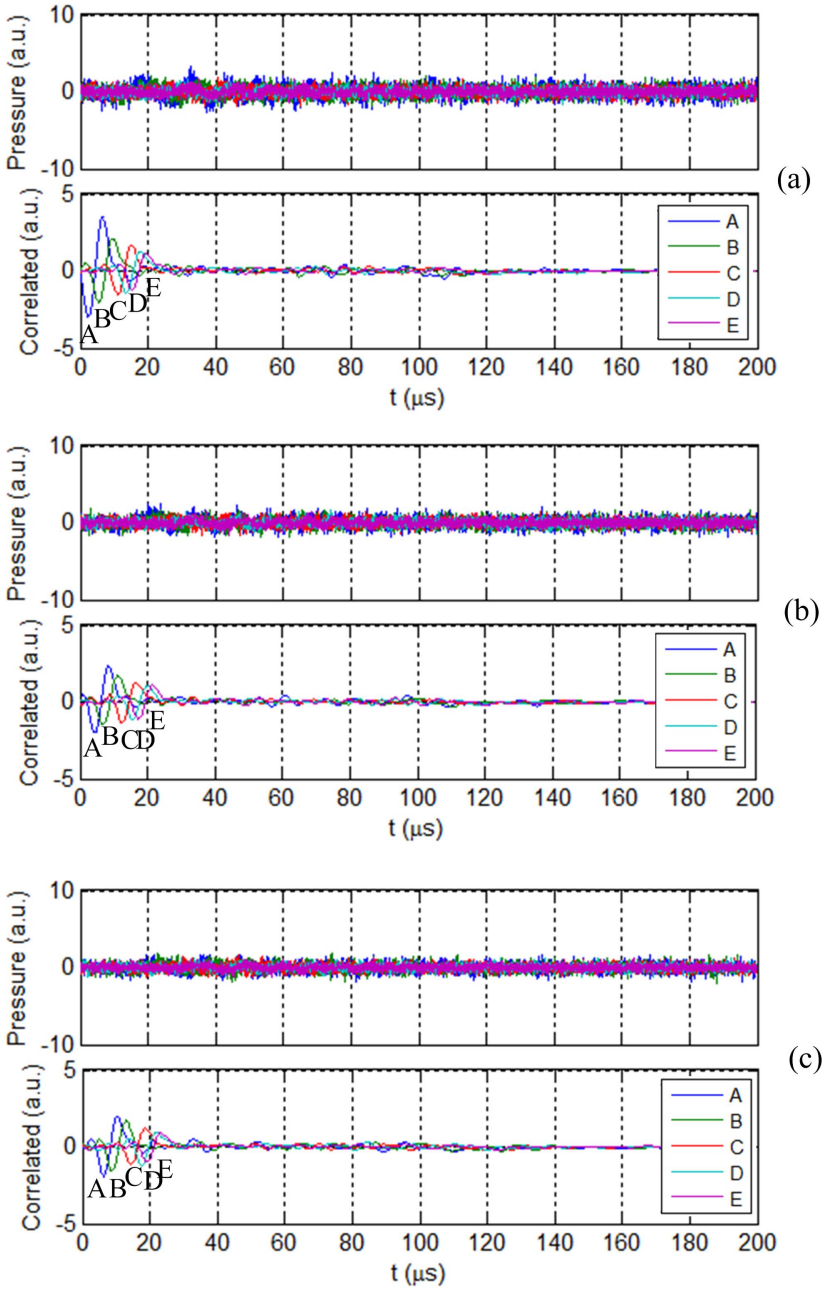

Figure 5.8: Thermo-acoustic signals and their corresponding correlated signals of biological tissue excited by modulated chirp pulse and detected by convex array detector for a target located at: (a) $y = 1.4$ cm, (b) $y = 1.7$ cm, and (c) $y = 2.0$ cm.

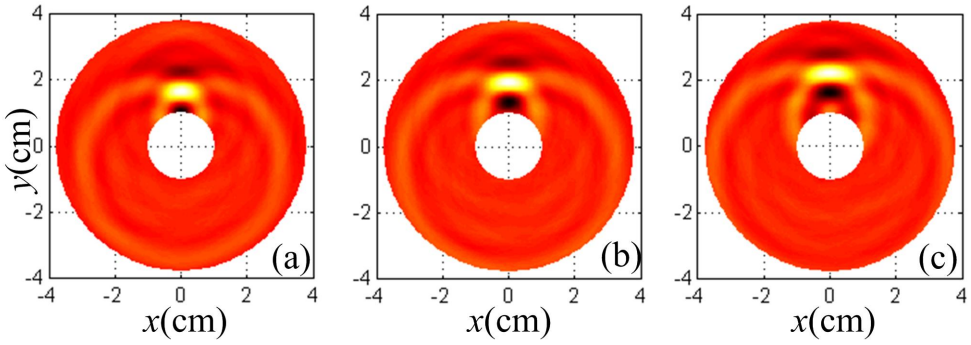

Figure 5.9: Reconstructed images of biological tissue excited by modulated chirp pulse and detected by convex array detector for a target located at: (a) $y = 1.4$ cm, (b) $y = 1.7$ cm, and (c) $y = 2.0$ cm.

The peak positions of the correlated TA signals presented in Figure 5.8 at detector labeled A, B, C, D, and E for three target positions can be shown in Table 5.4. The negative peak of correlated signals agree with the negative peak of TA signals that generated using the modulated Gaussian pulse. In the reconstructed images, the artifacts of "spreading" and "wings" are generated in the reconstructed images. In convex detection geometry, the imaging domain is outside the array contour and this may be the cause of this artifact. It can be seen that the longer distance between target and the detector array can cause the more spreading. However, the reconstructed images show the reconstructed target position that relatively agree with their original target positions.

5.3.2 Variation of target dimensions

In this subsection, the numerical solution of TA signal generation in biological tissue with the modulated chirp pulse, as shown in Figure 5.1, and with the convex array detection is described. The dielectric properties of the biological tissue for the convex array detection case are presented in Table 4.6 and the acoustic properties of the

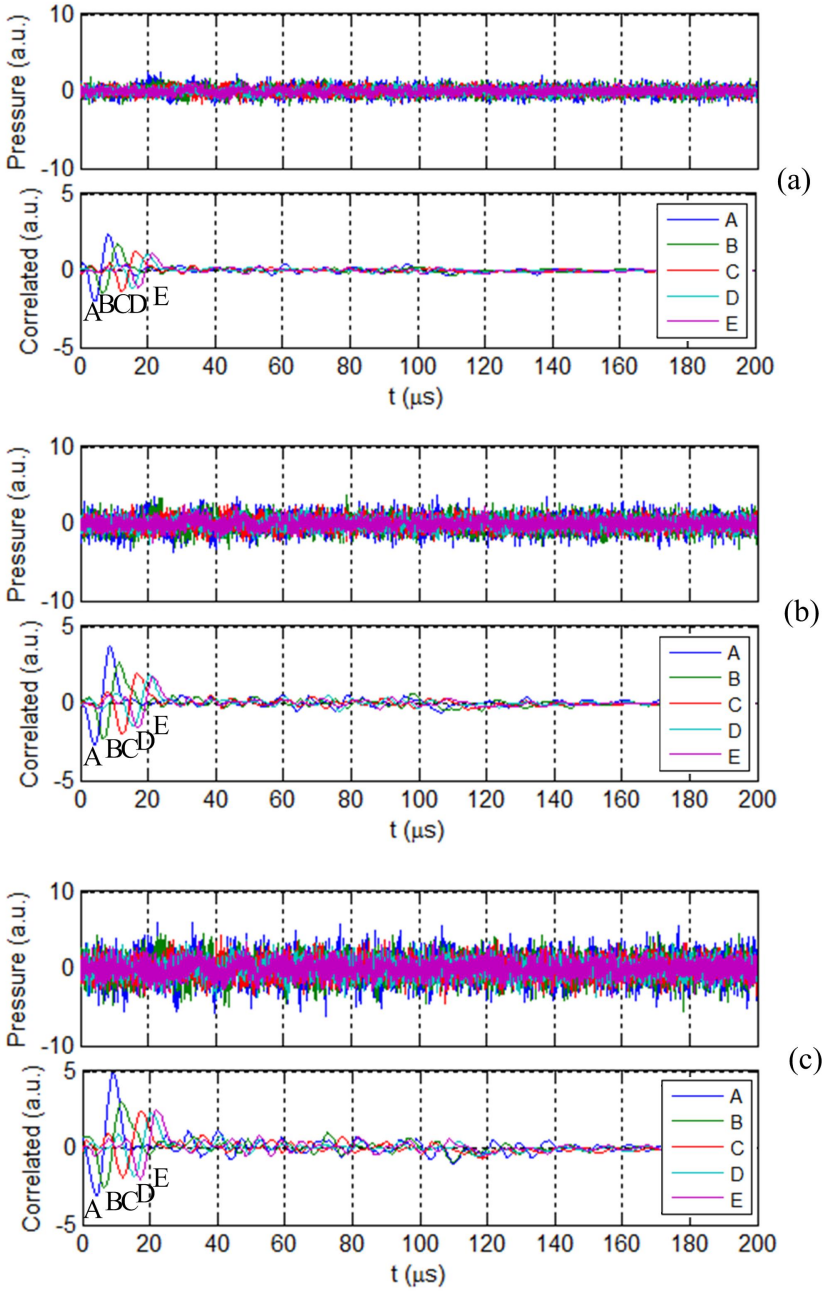

Figure 5.10: Thermo-acoustic signals and their corresponding correlated signals of biological tissue excited by modulated chirp pulse and detected by convex array detector for a target radius of: (a) 3 mm, (b) 4 mm, and (c) 5 mm.

tissue are presented Table 4.2. In this simulation, the radius of a target located at $x = 0$ cm, $y = 1.7$ cm is varied with three different radius of 3 mm, 4 mm, and 5 mm. The geometries and their corresponding FEM meshes for the simulation was illustrated in Figure 4.14. The location of a point radiation of the modulated chirp pulse is fixed and located at $x = 0$ cm, $y = 0$ cm. The results of captured TA signals and the correlated TA signals are presented in Figure 5.10 and their corresponding reconstructed images are presented in Figure 5.11.

Table 5.5: Negative peak positions of correlated TA signals of biological tissue excited by modulated chirp pulse and detected by convex array detector with variation of target dimension.

	Negative peak position (μs) at detector				
Target radius	A	B	C	D	E
3 mm	4.36	7.08	12.68	15.68	17.28
4 mm	4.12	7.04	12.40	15.60	17.00
5 mm	3.32	6.76	12.28	15.44	16.56

The peak positions of the correlated TA signals presented in Figure 5.10 at detector labeled A, B, C, D, and E for three target positions can be shown in Table 5.5. The negative peak of correlated signals agree with the negative peak of TA signals that generated using the modulated Gaussian pulse. In the reconstructed images, the artifacts of "spreading" and "wings" are generated in the reconstructed images. It can be seen that the bigger target dimension can cause the more spreading. However, the reconstructed images show the reconstructed target position and dimension that relatively agree with their original target positions.

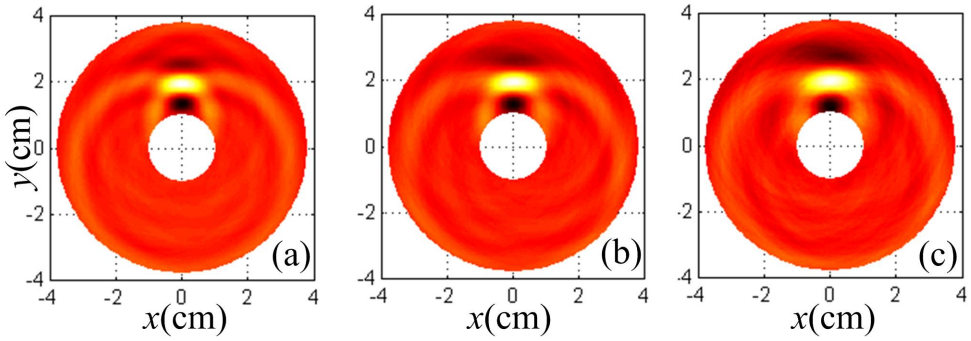

Figure 5.11: Reconstructed images of biological tissue excited by modulated chirp pulse and detected by convex array detector for a target radius of: (a) 3 mm, (b) 4 mm, and (c) 5 mm.

5.3.3 Variation of target numbers

In this subsection, the numerical solution of TA signal generation in biological tissue with the modulated chirp pulse, as shown in Figure 5.1, and with the convex array detection is described. The dielectric properties of the biological tissue for the convex array detection case are presented in Table 4.6 and the acoustic properties of the tissue are presented Table 4.2. In this simulation, the number of target is varied with three different cases: one target, two targets, and three targets. The geometries and their corresponding FEM meshes for the simulation was illustrated in Figure 4.17. The location of a point radiation of the modulated chirp pulse is fixed and located at $x = 0$ cm, $y = 0$ cm. The results of captured TA signals and the correlated TA signals are presented in Figure 5.12 and their corresponding reconstructed images are presented in Figure 5.13.

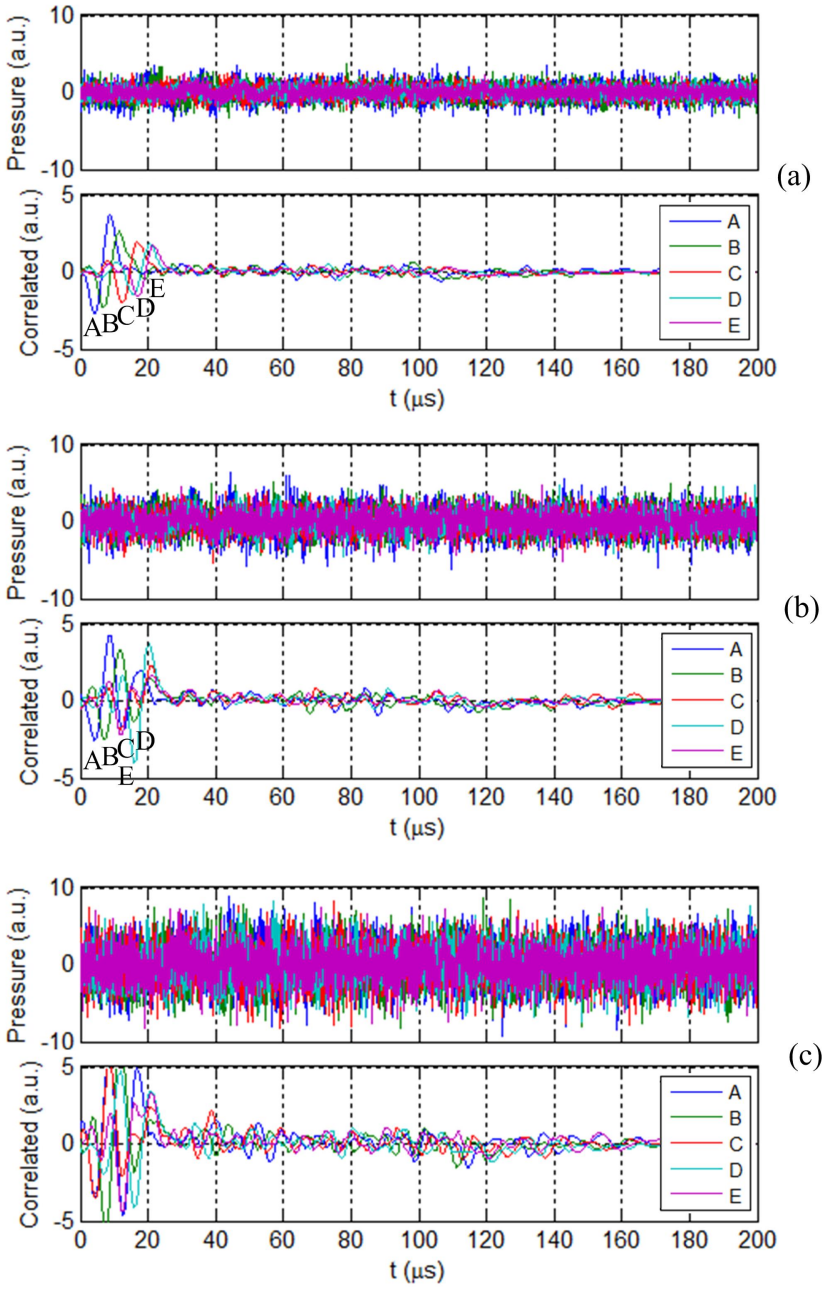

Figure 5.12: Thermo-acoustic signals and their corresponding correlated signals of biological tissue excited by modulated chirp pulse and detected by convex array detector for: (a) one target, (b) two targets, and (c) three targets.

Table 5.6: Negative peak positions of correlated TA signals of biological tissue excited by modulated chirp pulse and detected by convex array detector with variation of target number.

	Negative peak position (μs) at detector				
Target number	A	B	C	D	E
one target	4.36	7.08	12.68	15.68	17.28
two targets	4.52	7.08	12.48	16.16	12.24
three targets	12.76	7.60	4.44	15.76	12.44

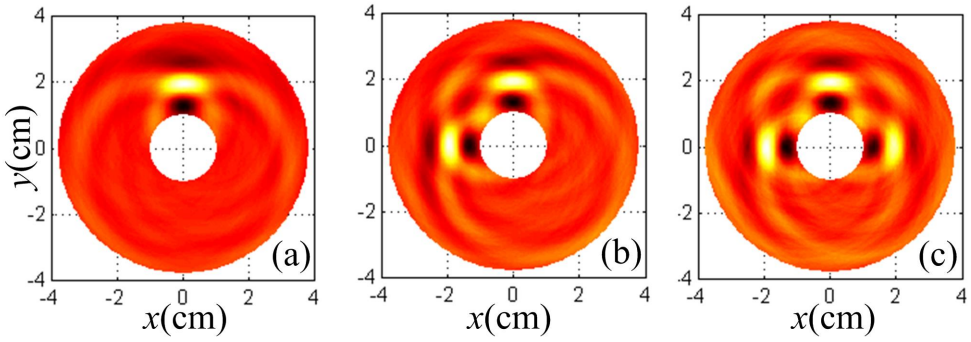

Figure 5.13: Reconstructed images of biological tissue excited by modulated chirp pulse and detected by convex array detector for: (a) one target, (b) two targets, and (c) three targets.

The peak positions of the correlated TA signals presented in Figure 5.12 at detector labeled A, B, C, D, and E for three target positions can be shown in Table 5.6. In the reconstructed images, the artifacts of "spreading" and "wings" are generated in the reconstructed images. It can be seen that the all the reconstructed targets at the same distance away from the detector array are distorted to about the same shape. However, the reconstructed images show the reconstructed target position, dimension, and number that relatively agree with their original target geometries.

5.4 Discussion

In this chapter, the modulated chirp pulse was used to excite the biological tissue to generate the TA signal and its corresponding cross-correlation output (called correlated signal) in various geometries. For the concave case, the solutions of calculated TA signal and correlated signal were presented in Figure 5.2 for variation of target positions, Figure 5.4 for variation of target dimensions, and Figure 5.6 for variation of target numbers, in which the solutions of reconstructed images to each one were presented in Figure 5.3, Figure 5.5, and Figure 5.7, respectively. For the convex case, the solutions of calculated TA signal and its correlated signal were presented in Figure 5.8 for variation of target positions, Figure 5.10 for variation of target dimensions, and Figure 5.12 for variation of target numbers, in which the solutions of reconstructed images to each one were presented in Figure 5.9, Figure 5.11, and Figure 5.13, respectively.

The reconstructed images for both concave and convex case showed ability of using the modulated chirp pulse in MITAT application. The target can be localized in the reconstructed image using the back-projection algorithm in various aspects of different positions, dimensions, and numbers. However, the artifacts of "spreading" and "wings" beside the target occurred in the cases of using the convex array detector

in both the modulated Gaussian pulse excitation and the modulated chirp pulse excitation. The peak-power reduction of using this technique and the artifact caused in the convex case will be analyzed and discussed in detail in Chapter 6.

5.5 Summary

This chapter presented the numerical solutions for the generated TA signal when the modulated chirp pulse was applied as an alternative microwave pulse excitation for microwave-induced thermo-acoustic tomography for biological tissue imaging in both concave and convex array detection and in various geometries of different target position, target dimensions, and target numbers. The corresponding reconstructed images using the proposed inverse step were depicted to show the ability of the time-domain numerical analysis for the problem of microwave-induced thermo-acoustic tomography with the modulated chirp pulse excitation. The results of generated TA signal and correlated signal were reasonable agreed with the characteristic of acoustic propagation in the tissue.

CHAPTER 6

ANALYSIS AND CHARACTERISTICS OF MITAT WITH MODULATED CHIRP PULSE EXCITATION

6.1 Introduction

This chapter presents the descriptive analysis and characteristics of the modulated chirp pulse and its application as an alternative microwave pulse in MITAT. The peak-power of the excitation pulse by using the modulated chirp pulse is compared to that of using the conventional modulated Gaussian pulse. The resolution for the image reconstruction by the correlated TA signal response in biological tissue excited by the modulated chirp pulse is also discussed. The influence of the difference in relative permittivity (ε_r) in biological tissue to the induced thermo-acoustic signal and its reconstructed image are described. Moreover, the artifacts in the reconstructed image of using convex array detection is described. The mechanical delay of TA signal generation by EM field excitation is also explained.

6.2 Peak-Power Reduction

The results of generated TA signals and reconstructed shown in Chapter 5 showed that the modulated chirp pulse can be used as an alternative microwave pulse shape for MITAT application. This section discusses the benefit of using this technique in

obtaining a reduction in the peak power microwave pulse. The instantaneous power loss density, $s(\mathbf{t}, t)$, of the electric field absorption in the tissue can be written as

$$s(\mathbf{r}, t) = \sigma(\mathbf{r})|E_z(\mathbf{r}, t)|^2. \tag{6.1}$$

Then, the mean power loss in the tissue is

$$P = \frac{1}{T}\int_0^T \int_{\mathbf{r}} s(\mathbf{r}, t) d\mathbf{r} dt, \tag{6.2}$$

where $\mathbf{r}$ is the spatial domain of the tissue. The mean power loss in the tissue of geometry in Figure 4.2(b) with the modulated chirp pulse excitation as shown in Figure 5.1 is 132.18 times higher than that of the conventional modulated Gaussian pulse excitation as shown in Figure 4.1. This ratio implies that the peak-power of a microwave transmitter in an MITAT system using the modulated chirp pulse can be lowered by 132.18 times. For a typical of energy per pulse of 10 mJ and with a short microwave pulse of 0.5 μs width [61], a microwave pulse transmitter with the peak power of 10 kW that is used for transmitting the conventional modulated Gaussian pulse can be reduced to only 76 W peak-power when the modulated chirp pulse of 100 μs chirp time is applied.

6.3 Range Resolution

In an analysis of range resolution where the modulated chirp pulse is used as an alternative microwave pulse excitation in an MITAT system, cross-correlation between filtered reference chirp (rectification of the modulated chirp pulse) and the unfiltered reference chirp is performed and is compared with the autocorrelation of a modulated rectangular pulse of the same pulse width and pulse period. Figure 6.1 presents the modulated rectangular pulse and the modulated chirp pulse which is equal in pulse

width and pulse period. The rectification of the modulated rectangular pulse and the modulated chirp pulse can be shown in Figure 6.2 where the filtered reference chirp between 20 kHz and 100 kHz is also presented.

The spectrum of the unfiltered and filtered reference chirp is presented in Figure 6.3(a) and (b) respectively. The reason that the cross-correlation of the unfiltered and filtered reference chirp is used for the calculation of range resolution is because the TA signal passes through the filter before the correlator process as shown in Figure 2.3. In this algorithm, the filter in the receiver has its function to remove the high frequency, low frequency and DC components of the induced TA response which represents the frequency response of acoustic detector or ultrasonic transducer.

The autocorrelation, $R_{gg}(\tau)$, of the reference signals, $g(t)$, which is a measure of the similarity of the signals separated in time by an amount of τ can be written as [62]

$$R_{gg}(\tau) = \int_{-\infty}^{\infty} g(t)g(t+\tau)dt. \tag{6.3}$$

In our case, $g(t)$ will be replaced with the modulated rectangular pulse function.

The cross-correlation, $(f \star g)(\tau)$, of the filtered reference signal, $f(t)$, and unfiltered reference signal, $g(t)$, can be written as

$$(f \star g)(\tau) = \int_{\infty}^{\infty} f^*(t)g(t+\tau)dt. \tag{6.4}$$

where * denotes the complex conjugate operation. The numerical results for the autocorrelation of the rectangular reference pulse and the cross-correlation of the filtered and unfilterd reference chirp is shown in Figure 6.4.

Equation (6.5) [62] represents the time resolution constant, T_{res}, in term of the

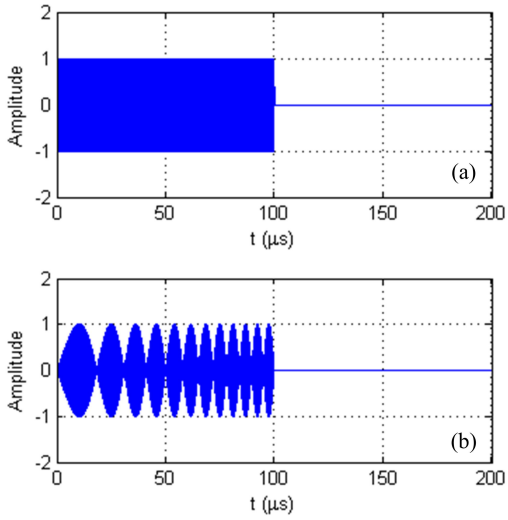

Figure 6.1: (a) Modulated rectangular pulse and (b) Modulated chirp pulse.

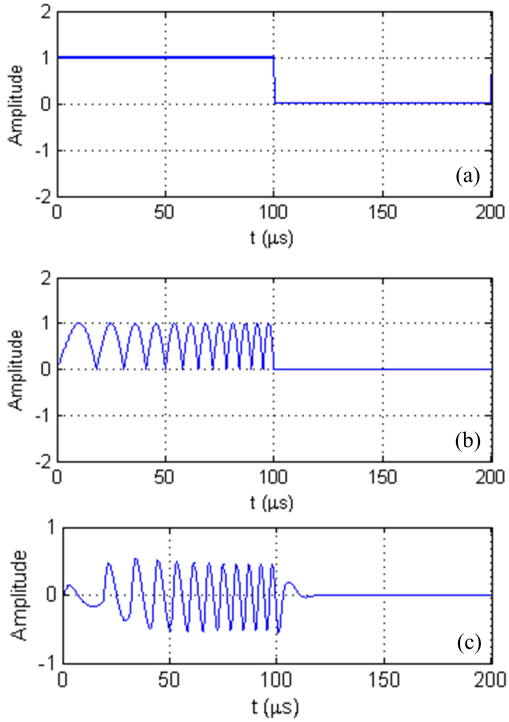

Figure 6.2: (a) Rectification signal of the modulated rectangular pulse, (b) Rectification signal of the modulated chirp pulse or the reference chirp, (c) Filtered reference chirp.

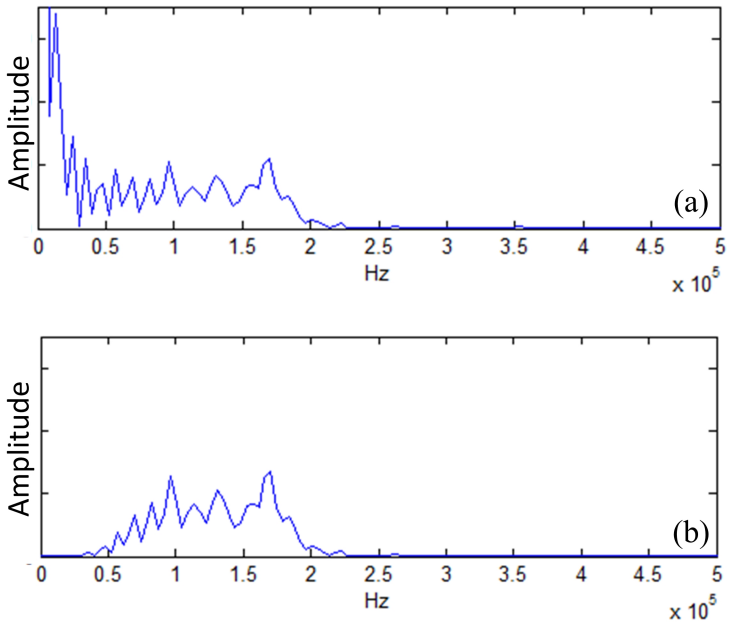

Figure 6.3: Spectrum of (a) unfiltered reference chirp and (b) filtered reference chirp.

autocorrelation function, $R_{gg}(\tau)$, which can be written as

$$T_{\text{res}} = \frac{\int_{-\infty}^{\infty} |R_{gg}(\tau)|^2 d\tau}{[R_{gg}(0)]^2} = \frac{\int_{-\infty}^{\infty} |R_{gg}(\tau)|^2 d\tau}{E_g^2}, \tag{6.5}$$

where E_g is the energy of the pulse and $R_{gg}(0)$ is the autocorrelation function at $\tau = 0$. The range resolution can be obtained by multiplying the time resolution constant by the speed of wave (1500 m/s in tissue). In the case of calculation of the range resolution where the modulated chirp pulse is used and with the inverse step presented in Figure 2.3, the autocorrelation $R_{gg}(\tau)$ will be replaced by the cross-correlation $(f \star g)(\tau)$ because the input to the inverse step is filtered. The numerical solution for the time resolution constant for the modulated rectangular pulse case is 66.66 μs, the effective bandwidth $B_{\text{eff}} = 1/T_{\text{res}} = 15.00$ kHz, and the range resolution is 10 cm at the acoustic speed of 1,500 m/s. While using the modulated chirp pulse, the numerical solution for the time resolution constant is 7.2 μs, the effective bandwidth is 138.85 kHz, and the range resolution is 1.08 cm. This results show the ability to

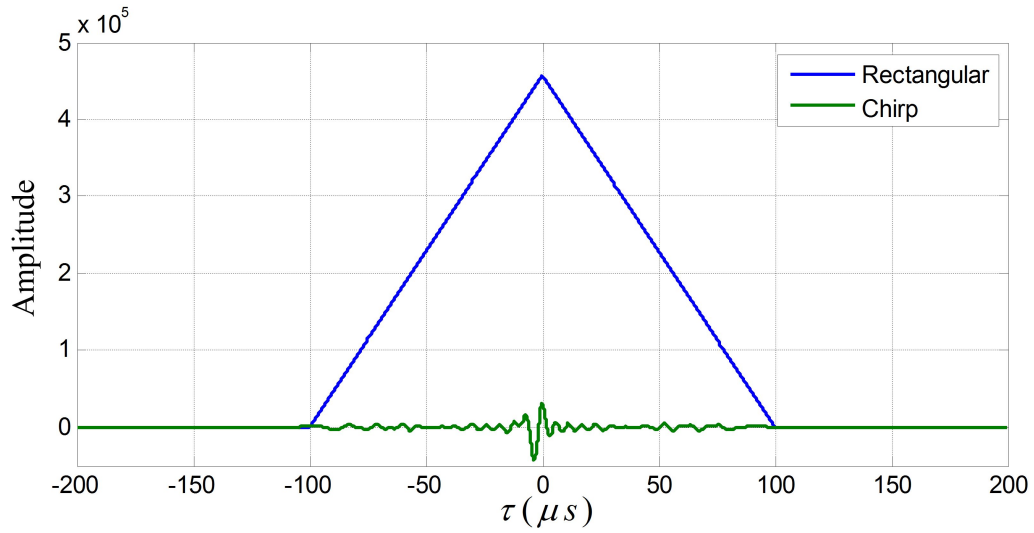

Figure 6.4: Autocorrelation of the rectangular reference pulse and cross-correlation between the filtered and unfiltered reference chirp.

reduce range resolution of the MITAT system using the modulated chirp pulse by 89.2% compared to the modulated rectangular pulse with the same pulse width and pulse period.

To demonstrate the ability of using the modulated chirp pulse compared with the modulated rectangular pulse in a MITAT system, the modulated rectangular pulse and the modulated chirp pulse are used to excite the biological tissue with the geometry in Figure 4.2(b). The results of correlated TA signals at 5 detect locations labeled A, B, C, D, and E and reconstructed images can be compared and shown in Figure 6.5 and Figure 6.6, respectively. The reconstructed image of using the modulated rectangular pulse shown in Figure 6.6(a) is clearly seen that it is distorted by an artifact on the background and blurred on and around the target in which it reasonable agrees with the calculated time resolution constant. The reconstructed image of using the modulated chirp pulse in Figure 6.6(b) shows the reconstructed target that is more sharp and the background is clear.

In comparison of signal-to-noise ratio (SNR) for each microwave pulse excitation (modulated Gaussian pulse, modulated rectangular pulse and modulated chirp pulse)

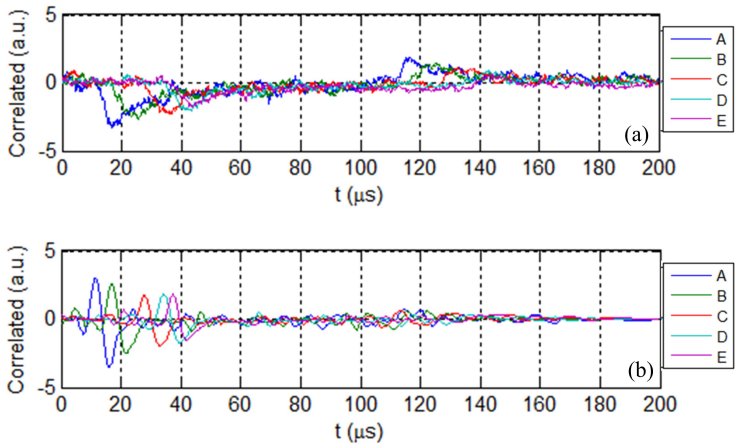

Figure 6.5: Comparison of correlated TA signal from the captured TA signal at 5 detector locations labeled A, B, C, D, and E between (a) modulated rectangular pulse excitation and (b) modulated chirp pulse excitation.

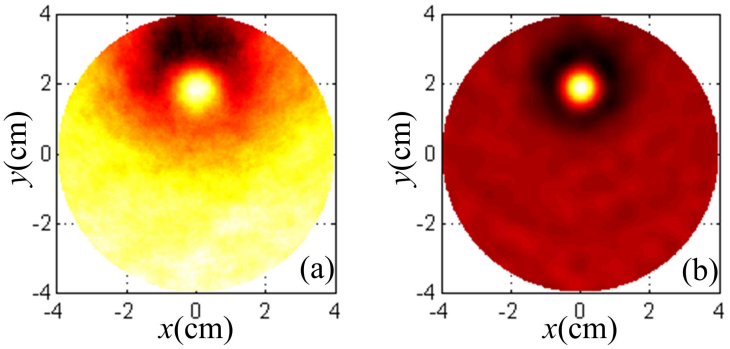

Figure 6.6: Comparison of the reconstructed images of using (a) modulated rectangular pulse excitation and (b) modulated chirp pulse excitation.

for the same total energy dissipated in the tissue, we assume the same antenna for radiating microwave energy on the tissue, so that the SNR can be calculated directly from the pulse shape where the white Gaussian noise power is fixed for all types of microwave pulse. The dissipated power of each microwave pulse is equalized by adjusting the peak value of each pulse. Then the SNR is the ratio of the pulse power to the noise power. Table 6.1 compares the SNR in dB, peak dissipated power, and total dissipated energy for each microwave pulse.

Table 6.1: Comparison of peak value, total dissipated energy, and signal-to-noise ratio for the same peak dissipated power for modulated Gaussian pulse, modulated rectangular pulse, and modulated chirp pulse.

Microwave pulse	Peak value	Total dissipated energy (J)	SNR (dB)
Modulated Gaussian pulse	1	0.3444	10
Modulated rectangular pulse	0.061	0.3517	9.95
Modulated chirp pulse	0.088	0.3525	10.10

Even though the range resolution is improved when the modulated chirp pulse is applied as a microwave pulse compared to conventional modulated Gaussian pulse for the MITAT system. It should be commented that by using the modulated chirp pulse, the signal-to-noise ratio is a bit higher than that of by using the modulated rectangular pulse or the modulated Gaussian pulse for the same total energy dissipated in the tissue. But the applying of the modulated chirp pulse will benefit of getting a fine resolution for a lower peak power.

6.4 Influence of Difference in Relative Permittivity

Based on the assumption that the electrical absorption property of biological tissue at microwave frequency depends on the electrical conductivity (σ) and the dielectric permittivity ($\varepsilon = \varepsilon_r \cdot \varepsilon_0$). This electrical absorption may affect the generation of TA signal. The variation of the relative permittivity (ε_r) of the target is considered instead of only the variation in electrical conductivity (σ) that was used to distinguish between the healthy tissue and the malignant tissue in this numerical study. The change of the relative permittivity of the target was performed with the geometry as shown in Figure 4.2(b) and the modulated chirp pulse was used to excite the tissue. The relative permittivity of the target was changed from 80 to 40, 160 and 240 while

the electrical conductivity was the same at 0.3 S/m. The relative permittivity and the electrical conductivity of the background were not changed. The generated TA signals were captured and the correlated TA signal were calculated. These correlated TA signal were used to reconstruct the image represent the local microwave absorption using the inverse step as shown in Figure 2.3. The results of reconstructed images were not significantly different. All the reconstructed images looked about the same. This situation may be from the fact that the inverse step with the back-projection algorithm is not a quantitative reconstruction technique. However, the reconstructed images showed that with different relative permittivity but equal in electrical conductivity, the target can be detected at the correct position and dimension.

6.5 Reconstruction Artifacts

In the detection by convex array for internal imaging as shown in Figure 6.7(a), it can be noticed that the reconstructed images as shown in Figure 4.13, 4.16, and 4.19 for the modulated Gaussian pulse excitation and in Figure 5.9, 5.11, and 5.13 for the modulated chirp pulse excitation had the artifact of "spreading" and "wings" on the target as shown in Figure 6.7(b).

The cause of the artifact can be explained as the effect of field of view of the detector, as shown in Figure 6.8(a), to the target. From a cursory examination of the targeted region, it can be seen that not all the detectors can see the target as shown in the shading area and the dash-line B and C but only the detector on dash-line A can. Also, there are no detectors that can see at the back of the target. On the other hand, with its reciprocal as shown in Figure 6.8(b), the target can not see all the detectors beyond the shading area between the point 1 and 2. It is plausible to suggest that the effect of incomplete information surrounding the target may result in the causing of the artifact comparing with the concave detection case that all detectors on the array contour surround the target.

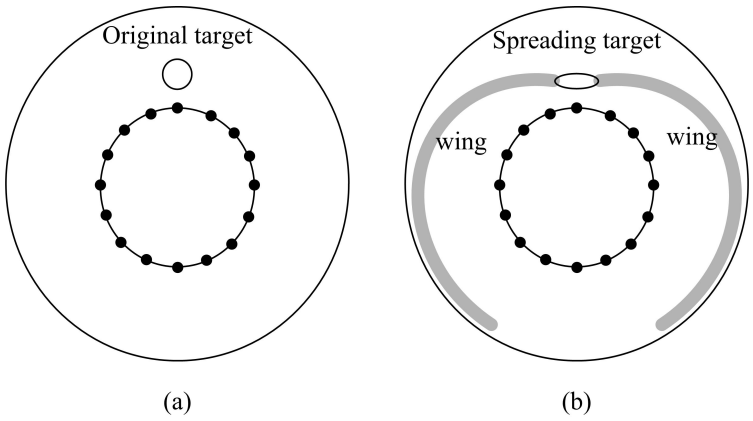

Figure 6.7: Artifacts of "spreading" and "wings" from image reconstruction in convex array (a) original target in convex array detection and (b) "spreading" and "wings" of reconstructed image.

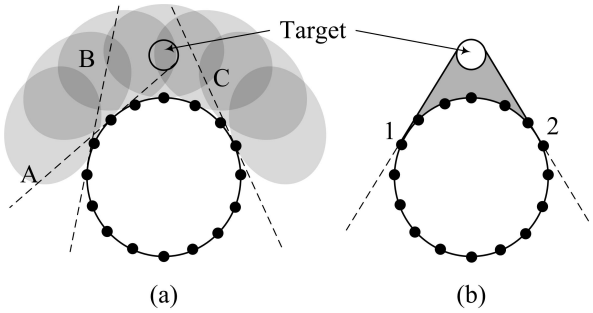

Figure 6.8: Field of view from (a) detector to target and (b) target to detector, in the configuration of convex array detection.

6.6 Mechanical Delay of Pressure Generation

In generation of the TA signal in biological tissue by microwave pulse excitation, the governing equations were presented in Eq.(2.1) and Eq.(2.7). The delay for the generation of TA signal while the microwave pulse is emitted from the antenna is equal the traveling time of EM field propagate from the antenna to the local absorption position (target) inside the tissue which is very short and can be neglected. When the target absorbs the EM field, the process of Joule heating occurs instantaneously in which the thermo-elastic process is also occurred instantly as well. The TA signal is generated at the same time when the microwave pulse absorption happens in the

tissue but it can not be detected because the acoustic detector is located on the boundary of the imaging domain (for convex array detection). After that, the time that the acoustic detector array receives the generated TA signal is equal the time of TA signal propagation from the local heat source to the detector.

6.7 Influence of Chirp Period to Image Contrast

In this section, the relation of the chirp period to the reconstructed image contrast is considered and described. The contrast or contrast ratio can be defined as the difference or the ratio between the maximum and minimum values of any property in interesting domain. For example, in image processing, the image contrast can be considered as the ratio between the luminance of the brightest white and the darkest black of the image. In this work, the electrical conductivity contrast of the original image is the ratio between the maximum and minimum electrical conductivities of the biological tissue. However, the reconstructed image contrast is the ratio between the maximum and minimum luminance of reconstructed image.

A numerical simulation for the generation of TA signals in the biological tissue with a modulated chirp pulse excitation of different chirp periods is performed using the TDFEM. The reconstructed image is generated using the inverse step as presented in Section 2.4. The geometry for the generation of TA signals is the geometry in concave array detection with a 5 mm radius target located at $x = 0$ cm, $y = 2.0$ cm, was shown in Figure 4.2(b). The modulated chirp pulsed with the variation of chirp period at 20 μs, 40 μs, 60 μs, 80 μs, and 100 μs and with the same pulse period of 200 μs are applied as the microwave pulse excitation and can be shown in Figure 6.9(a1), (a2), (a3), (a4), and (a5). The results of correlated TA signal at 5 detector locations labeled A, B, C, D, and E is presented in Figure 6.9(b1), (b2), (b3), (b4), and (b5) for the different chirp period. The results of reconstructed images can be shown in Figure 6.9(c1), (c2), (c3), (c4), and (c5) for the corresponding chirp period at 20 μs,

40 μs, 60 μs, 80 μs, and 100 μs, respectively.

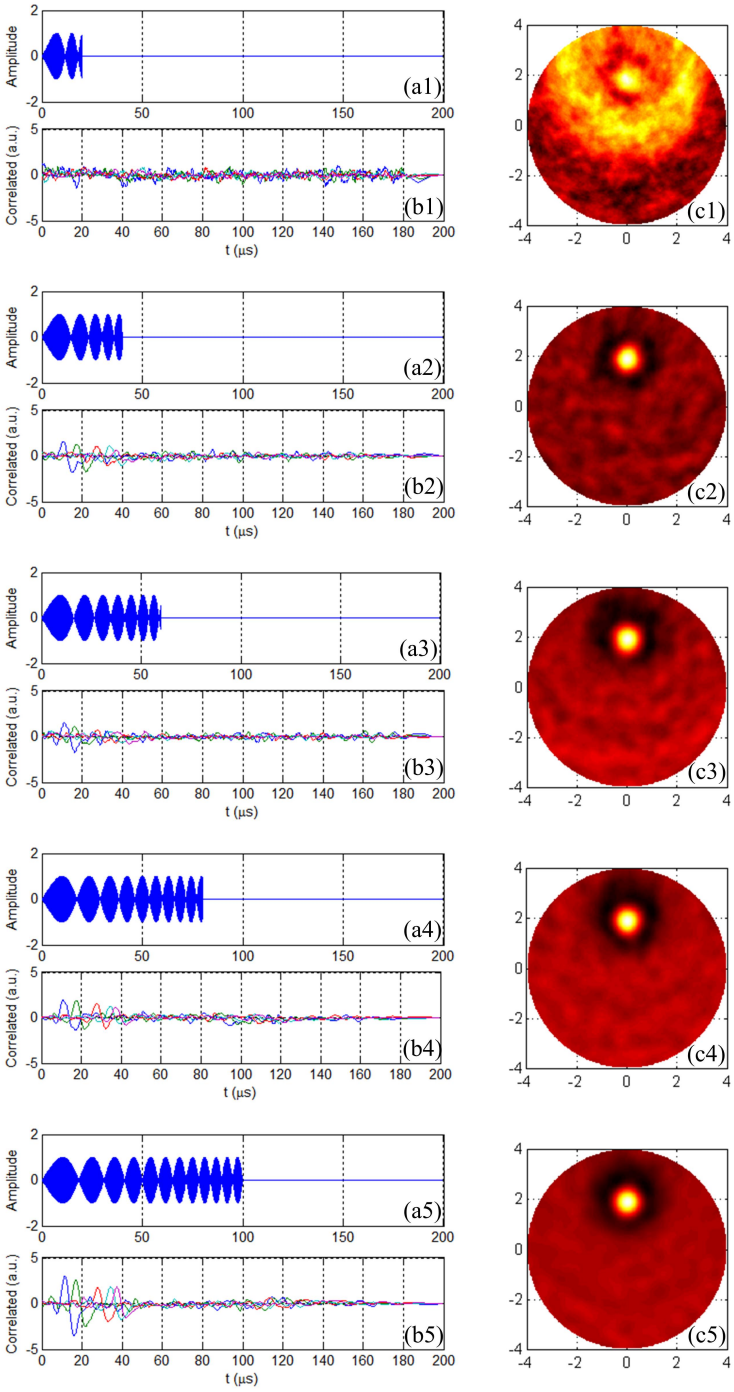

Figure 6.9: Modulated chirp pulses, their corresponding correlated TA signals, and their corresponding reconstructed images for the variation of chirp pulse of 20 μs, 40 μs, 60 μs, 80 μs, and 100 μs.

In the reconstructed images in Figure 6.9, it can be clearly seen that the quality of the reconstructed image is degraded when the chirp period is shortened. In this case, we define the quality of the reconstructed image is the correctness of reconstructed image which indicates the correct position, dimension, and number of target compared to its original local conductivity distribution inside the imaging domain. The correctness of reconstructed image means that the image shows no major artifact that makes wrong interpretation for target and background.

In this case, the electrical conductivity of the target and background is 0.3 S/m and 0.1 S/m, respectively corresponding to a contrast ratio of 3. However, in the inverse step of MITAT in this study applies the back-projection algorithm as the image reconstruction algorithm. The results of reconstructed images will be normalized in amplitude before they are plotted. With this approach the output of the reconstructed image will have the maximum value of 1 and the minimum value of 0. Therefore, the contrast of the reconstructed image is considered as 1. However, some artifacts on background are boosted up (or amplified) as a result of normalization in the case of low contrast between background and target. With this assumption and the numerical results in Figure 6.9, it can be concluded that the longer of chirp period will not be affected in the reconstructed image contrast but longer chirp pulse give a higher reconstructed image quality.

6.8 Assumptions and Limitations

This section describes the assumption and the limitation of the proposed technique. In this proposed technique, the modulated chirp pulse is applied as an alternative microwave pulse excitation. This application assumes that the longer duration microwave pulse can deliver more energy to the tissue. Then the peak-power of the microwave pulse transmitter can be reduced. With the wide microwave pulse, the induced TA signal can not be used to detect the location of the target because the

wider induced TA pulse will be larger wavelength in the tissue.

One of the limitations to this technique is the limitation of the back-projection algorithm. The back-projection algorithm assumes that the acoustic speed inside the imaging domain is constant. If the acoustic speed is not constant throughout the imaging domain, this technique cannot be applied or may cause an artifact in reconstructed image.

6.9 Summary

This chapter presented the analysis and characteristic of MITAT system with the modulated chirp pulse excitation. The analysis included the power loss in the tissue that was used for the analysis of peak-power reduction. The total power loss was presented and was used to compare the total power loss in the tissue between the use of the modulated chirp pulse and the modulated Gaussian pulse in which power loss in tissue was directly proportional to the energy per pulse at the aperture of the transmitting antenna. The autocorrelation of the reference signal, the resolution time, and the range resolution was presented for the this proposed technique of using the modulated chirp pulse. The influence of difference in relative permittivity, reconstruction artifact, and mechanical delay for TA signal generation were also analyzed.

CHAPTER 7

CONCLUSIONS

7.1 Contributions of the Work

In this study, the modulated chirp pulse was applied as an alternative microwave pulse excitation for the first time for the microwave-induced thermo-acoustic tomography system with concave and convex array detection. The modulated chirp pulse can be applied for a MITAT system with a significantly reduce the peak-power requirement. The model of a MITAT system was described as the forward step for TA signal generation in biological tissue and the inverse step for TA signal detection and image reconstruction.

In the forward step, the numerical analysis of MITAT with the modulated chirp pulse excitation using the time-domain finite element method (TDFEM) was explored for the first time and was used for the calculation of both time-varying electric field and pressure field generation in biological tissue. This time-domain numerical procedure formed the generation of time-varying thermo-acoustic signal for a non-conventional microwave pulse. The numerical solutions of thermo-acoustic signal generation in the biological tissue from the microwave pulse excitation of both the conventional modulated Gaussian pulse and the modulated chirp pulse were shown in which they can be used to reconstruct the image representing the microwave absorption distribution inside the tissue. The model of biological tissue for thermo-acoustic

signal generation was introduced by the combination of dielectric and acoustic properties of soft tissue.

In the inverse step, the inverse model for MITAT system with the modulated chirp pulse excitation including the acoustic detection, cross-correlation, and image reconstruction was introduced. In the acoustic detection, the acoustic detector was considered to have the band-limitation and noise addition. In the cross-correlation, the rectification of the modulated chirp pulse was used as a reference signal to cross-correlate with the captured TA signal at the acoustic detector location to acquire the cross-correlated signal of the captured TA signal in which it represented the propagation (delay) time from the position of generated TA signal to the acoustic detector location. In image reconstruction, a simple back-projection was used to reconstruct an image represented the microwave absorption distribution of the imaging domain from the cross-correlated TA signal.

The numerical results of TA signal generation were presented for biological tissue with the configuration of acoustic array detection of concave and convex array. The biological tissue geometries with variations of target positions, target dimensions, and target numbers were presented and used for generation of TA signal with both the modulated Gaussian pulse and the modulated chirp pulse at the carrier frequency of 915 MHz. The results of TA signal reasonably agreed with the characteristic of acoustic propagation in the tissue and their corresponding reconstructed images showed had the correct position, dimension, and number of targets inside the tissue. The artifacts of reconstructed image occurred for all the case of convex array detection showed the "spreading" and "wings". It is suggested that these artifacts are due to incomplete target coverage in the convex detector configuration.

The analysis and characteristic of MITAT system with the modulated chirp pulse excitation was presented. The peak-power reduction was presented where it compared the total power loss in the tissue between the use of the modulated chirp pulse and

the modulated Gaussian pulse in which power loss in tissue was directly proportional to the energy per pulse at the aperture of the transmitting antenna. As a result of peak-power reduction when applying the modulated chirp pulse as a microwave pulse excitation in MITAT system while compared to the use of the modulated Gaussian pulse, the peak-power of microwave pulse transmitter can be reduced by 132.18.

The range resolution was analyzed for the applying of this microwave pulse compared to the modulated rectangular pulse of the same pulse period. The range resolution with this technique can be reduced by 33.8% of the range resolution when using the rectangular pulse. The influence of difference in relative permittivity was also described. In tissues with a target of the same electrical conductivity but difference in relative permittivity, there was obviously no difference between those reconstructed images using the back-projection algorithm. The mechanical delay for TA signal generation was also analyzed and described.

7.2 Future Direction

In this numerical study, applying the modulated chirp pulse in MITAT system showed the results of gaining more efficient power of the microwave pulse transmitter. An experimental verification for the generation of TA signal in biological tissue using the modulated chirp pulse would be helpful to this numerical study.

A measurement plan that is shown in Figure 7.1 is a plan for future study. In this diagram, a piece of chicken breast will be used as a target in which it will be immersed in the mineral oil. The mineral oil will act as a coupling medium for TA wave propagation in which it will be matched in acoustic properties and have lower conduction loss than that of using water. A microwave pulse transmitter at the carrier frequency of 1 GHz is intensity modulated with the chirp pulse to form a modulated chirp pulse and will be used as an alternative microwave pulse excitation. This pulse will be radiated through an horn antenna in which it direction will be directly pointed

to the target. An ultrasonic transducer will be used as an acoustic detector in which it will capture the generated TA signal. A scanning system may be used to provide a form of concave or convex array detector for an image reconstruction. The captured TA signal from the ultrasonic transducer which will be affected of noise addition and the band-limitation will be passed through a low-noise amplifier and then recorded by an oscilloscope. This captured TA signal will be recorded in a computer then the process of cross-correlation and back-projection algorithm will be used by signal processing inside the computer through computer programming.

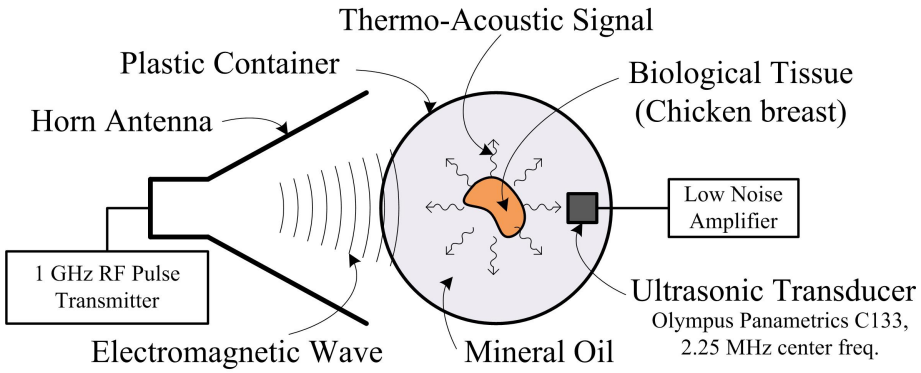

Figure 7.1: Diagram of experimental setup for a generation of thermo-acoustic signal in biological tissue.

A preliminary experiment was performed in an anechoic chamber. A picture of the experiment can be shown in Figure 7.2. A chirp pulse with the pulse period of 200 μs and the chirp width of 100 μs and the starting and stopping frequency of 20 kHz and 100 kHz as shown in Figure 7.3 was generated by Agilent 33220A arbitrary waveform generator and used to modulated with the microwave frequency carrier 1 GHz.

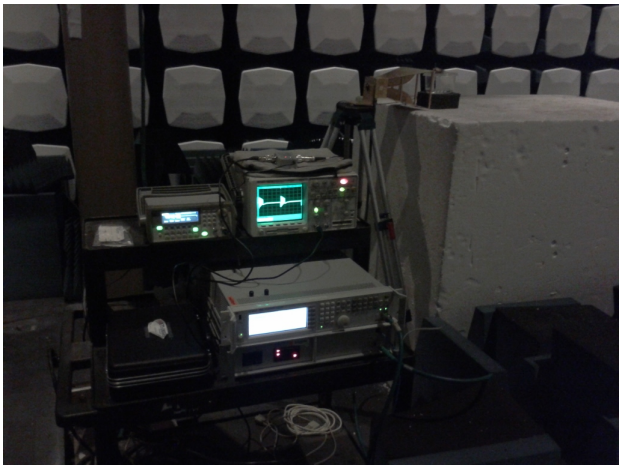

Figure 7.2: A preliminary experiment setup for a generation of thermo-acoustic signal.

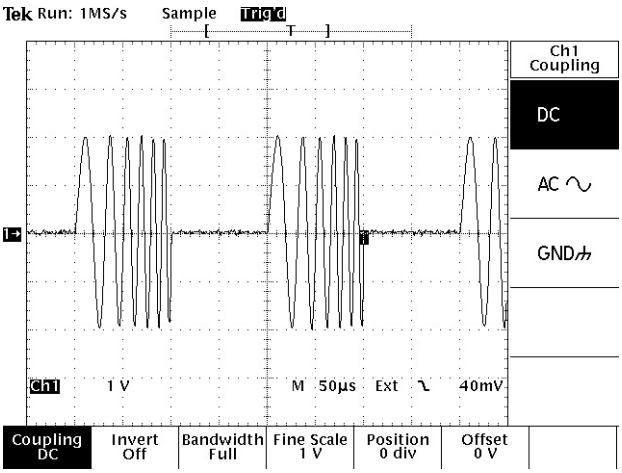

Figure 7.3: Chirp pulse generated by Agilent 33220A arbitrary waveform generator.

The modulated chirp pulse was fed to the horn antenna. The sample was a piece of chicken breast (1 cm×2 cm) immersed in mineral oil in plastic container which can be shown in Figure 7.4. An ultrasonic transducer of model C133 from Olympus Panametrices was applied as the acoustic detector and a low noise amplifier (EMCO model 7405 broadband amplifier) was used to amplifier the signal output of the ultrasonic transducer. The preliminary captured TA signal at the output of the low noise amplifier can be shown in Figure 7.5. Future experiment with a scanning system for rotating the sample will be helpful in the demonstration of reconstructed image.

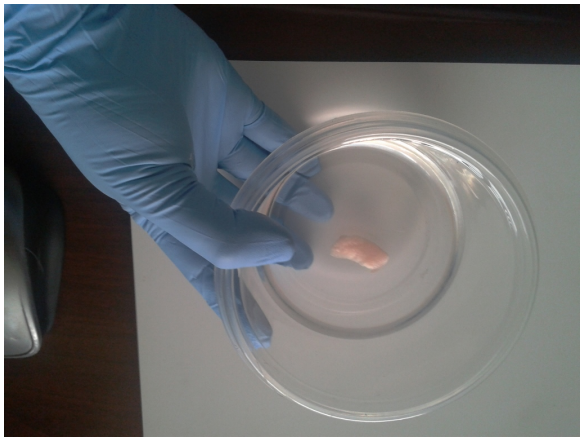

Figure 7.4: Chicken sample immersed in mineral oil.

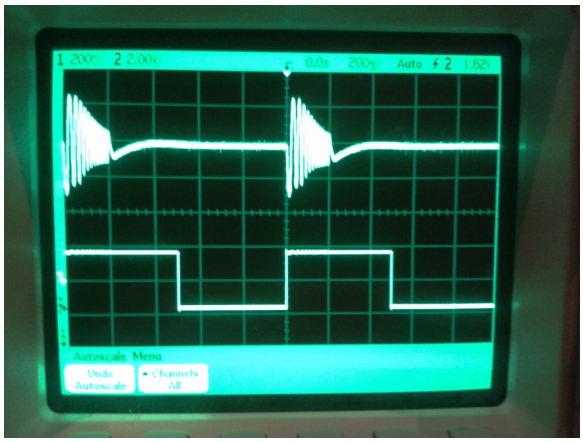

Figure 7.5: Measured TA signal output from the low noise amplifier.

REFERENCES

[1] B. W. Stewart and C. P. Wild, *World Cancer Report 2014*. International Agency for Research on Cancer (IARC), World Health Organization, 2014.

[2] Cancer Research UK, "World cancer factsheet," International Agency for Research on Cancer (IARC), World Health Organization, Tech. Rep., 2014.

[3] F. Ritter, T. Boskamp, A. Homeyer, H. Laue, M. Schwier, F. Link, and H. O. Peitgen, "Medical image analysis," *IEEE Pulse*, vol. 2, no. 6, pp. 60–70, 2011.

[4] L. Mertz, "Medical imaging: Just what the doctor (and the researcher) ordered: New applications for medical imaging technology," *IEEE Pulse*, vol. 4, no. 1, pp. 12–17, 2013.

[5] T. U. Grbz, B. Aslanyrek, A. Yapar, H. ahintrk, and I. Akduman, "A nonlinear microwave breast cancer imaging approach through realistic body - breast modeling," *IEEE Trans. Antennas Propagat.*, vol. 62, no. 5, pp. 2596–2605, 2014.

[6] D. Piao, K. E. Bartels, J. Zhen, G. R. Holyoak, J. W. Ritchey, G. Xu, C. F. Bunting, and G. F. Slobodov, "Alternative transrectal prostate imaging: A diffuse optical tomography method," *IEEE J. Sel. Topics Quantum Electron.*, vol. 16, no. 4, pp. 715–729, 2010.

[7] G. Ku, B. D. Fornage, X. Jin, M. Xu, K. K. Hunt, and L. V. Wang, "Thermoacoustic and photoacoustic tomography of thick biological tissues toward breast imaging," *Technology in Cancer Research & Treatment*, vol. 4, no. 5, pp. 559–565, 2005.

[8] L. V. Wang, "Prospects of photoacoustic tomography," *Med. Phys.*, vol. 35, no. 12, pp. 5758–5767, 2008.

[9] M. Xu and L. V. Wang, "Pulsed-microwave-induced thermoacoustic tomography: Filtered backprojection in a circular measurement configuration," *Med. Phys.*, vol. 29, no. 8, pp. 1661–1669, 2002.

[10] R. A. Kruger, K. Stantz, and J. W. L. Kiser, "Thermoacoustic ct of the breast," in *Proc. SPIE 4682, Medical Imaging 2002: Physics of Medical Imaging*, vol. 4682, pp. 521–525, 10.1117/12.465596.

[11] L. Nie, D. Xing, Q. Zhou, D. Yang, and H. Guo, "Microwave-induced thermoacoustic scanning ct for high-contrast and noninvasive breast cancer imaging," *Med. Phys.*, vol. 35, no. 9, pp. 4026–4032, 2008.

[12] X. Zhu, Z. Zhao, K. Yang, Z. Nie, and Q. Liu, "A prototype system of microwave induced thermo-acoustic tomography for breast tumor," in *Engineering in Medicine and Biology Society (EMBC), 2012 Annual International Conference of the IEEE*, pp. 464–467.

[13] Y. Fu, Z. Ji, W. Ding, F. Ye, and C. Lou, "Thermoacoustic imaging over large field of view for three-dimensional breast tumor localization: A phantom study," *Med. Phys.*, vol. 41, no. 11, p. 110701, 2014.

[14] S. Mukherjee, C. F. Bunting, and D. Piao, "Finite-element-method based reconstruction of heterogeneous conductivity distribution under point-illumination in trans-rectal imaging geometry for thermo-acoustic tomography," in *Proceeding of Biomedical Optics*, ser. OSA Technical Digest. Optical Society of America, p. BSu3A.44.

[15] R. Pethig, "Dielectric properties of body tissues," *Clinical Physics and Physiological Measurement*, vol. 8, no. 4A, pp. 5–12, 1987.

[16] W. T. Joines, Y. Zhang, C. Li, and R. L. Jirtle, "The measured electrical properties of normal and malignant human tissues from 50 to 900 mhz," *Med. Phys.*, vol. 21, no. 4, pp. 547–550, 1994.

[17] B. Guo, J. Li, H. Zmuda, and M. Sheplak, "Multifrequency microwave-induced thermal acoustic imaging for breast cancer detection," *IEEE Trans. Biomed. Eng.*, vol. 54, no. 11, pp. 2000–2010, 2007.

[18] F. Gao and Y. Zheng, "A correlated microwave-acoustic imaging method for early-stage cancer detection," in *Proc. Annual International Conference of the IEEE Engineering in Medicine and Biology Society (EMBC)*, pp. 480–483.

[19] Z. Ji, C. Lou, S. Yang, and D. Xing, "Three-dimensional thermoacoustic imaging for early breast cancer detection," *Med. Phys.*, vol. 39, no. 11, pp. 6738–6744, 2012.

[20] Z. Ji, Y. Fu, and S. Yang, "Microwave-induced thermoacoustic imaging for early breast cancer detection," *J. Innovative Opt. Health Sci.*, vol. 6, no. 1, p. 1350001, 2013.

[21] X. Wang, D. R. Bauer, R. Witte, and H. Xin, "Microwave-induced thermoacoustic imaging model for potential breast cancer detection," *IEEE Trans. Biomed. Eng.*, vol. 59, no. 10, pp. 2782–2791, 2012.

[22] X. Jin, C. Li, and L. V. Wang, "Effects of acoustic heterogeneities on transcranial brain imaging with microwave-induced thermoacoustic tomography," *Med. Phys.*, vol. 35, no. 7, pp. 3205–3214, 2008.

[23] Z. Liu, L. Liu, Y. Xu, and L. V. Wang, "Transcranial thermoacoustic tomography: A comparison of two imaging algorithms," *IEEE Trans. Med. Imag.*, vol. 32, no. 2, pp. 289–294, 2013.

[24] S. Mukherjee, C. F. Bunting, and D. Piao, "Trans-rectal thermo-acoustic computed tomography: an initial in silico study," *X Acoust. Imaging Sens.*, vol. 1, no. 1, pp. 1–17, 2014.

[25] L. Nie, D. Xing, and S. Yang, "In vivo detection and imaging of low-density foreign body with microwave-induced thermoacoustic tomography," *Med. Phys.*, vol. 36, no. 8, pp. 3429–3437, 2009.

[26] S. Kellnberger, A. Hajiaboli, D. Razansky, and V. Ntziachristos, "Near-field thermoacoustic tomography of small animals," *Phys. Med. Biol.*, vol. 56, pp. 3433–3444, 2011.

[27] A. G. Bell, "On the production and reproduction of sound by light," *Am. J. Sci.*, vol. 20, no. 118, pp. 305–324, 1880.

[28] J. C. Lin, "On microwave-induced hearing sensation," *IEEE Trans. Microwave Theory Tech.*, vol. 25, no. 7, pp. 605–613, 1977.

[29] T. Bowen, "Radiation-induced thermoacoustic soft tissue imaging," in *Proc. IEEE Ultrasonics Symposium*, pp. 817–822.

[30] T. Bowen, R. L. Nasoni, A. E. Pifer, and G. H. Sembroski, "Some experimental results on the thermoacoustic imaging of tissue equivalent phantom materials," in *Proc. IEEE Ultrasonics Symposium*, pp. 823–827.

[31] C. Gabriel, S. Gabriel, and E. Corthout, "The dielectric properties of biological tissues: I. literature survey," *Phys. Med. Biol.*, vol. 41, no. 11, pp. 2231–2249, 1996.

[32] S. Gabriel, R. W. Lau, and C. Gabriel, "The dielectric properties of biological tissues: Ii. measurements in the frequency range 10 hz to 20 ghz," *Phys. Med. Biol.*, vol. 41, no. 11, pp. 2251–2269, 1996.

[33] ——, "The dielectric properties of biological tissues: Iii. parametric models for the dielectric spectrum of tissues," *Phys. Med. Biol.*, vol. 41, no. 11, pp. 2271–2293, 1996.

[34] R. A. Kruger, "Thermoacoustic computed tomography-technical considerations," *Med. Phys.*, vol. 26, no. 9, pp. 1832–1837, 1999.

[35] R. A. Kruger, J. W. L. Kiser, A. P. Romilly, and P. Scmidt, "Thermoacoustic ct of the breast: pilot study observations," in *Proc. SPIE 4256, Biomedical Optoacoustics II*, vol. 4256, pp. 1–5, 10.1117/12.429292.

[36] L. V. Wang, X. Zhao, H. Sun, and G. Ku, "Microwave-induced acoustic imaging of biological tissues," *Rev. Sci. Instrum.*, vol. 70, no. 9, pp. 3744–3748, 1999.

[37] M. Xu and L. V. Wang, "Time-domain reconstruction for thermoacoustic tomography in a spherical geometry," *IEEE Trans. Med. Imag.*, vol. 21, no. 7, pp. 814–822, 2002.

[38] Y. Xu, D. Feng, and L. V. Wang, "Exact frequency-domain reconstruction for thermoacoustic tomography: I. planar geometry," *IEEE Trans. Med. Imag.*, vol. 21, no. 7, pp. 823–828, 2002.

[39] Y. Xu, M. Xu, and L. V. Wang, "Exact frequency-domain reconstruction for thermoacoustic tomography. ii. cylindrical geometry," *IEEE Trans. Med. Imag.*, vol. 21, no. 7, pp. 829–833, 2002.

[40] P. Stefanov and G. Uhlmann, "Thermoacoustic tomography arising in brain imaging," *Inverse Problems*, vol. 27, no. 4, p. 045004, 2011.

[41] G. Zhu, M. Popovic, and Q. Fang, "Microwave-induced thermoacoustics: Assisting microwave tomography," *IEEE Trans. Magn.*, vol. 45, no. 3, pp. 1654–1657, 2009.

[42] X. Wang, D. R. Bauer, J. L. Vollin, D. G. Manzi, R. S. Witte, and X. Hao, "Impact of microwave pulses on thermoacoustic imaging applications," *IEEE Antennas Wireless Propag. Lett.*, vol. 11, 2012.

[43] L. Yao, G. Guo, and H. Jiang, "Quantitative microwave-induced thermoacoustic tomography," *Med. Phys.*, vol. 37, no. 7, pp. 3752–3759, 2010.

[44] N. A. Rejesh and M. Pramanik, "Photoacoustic and thermoacoustic signal characteristics study," in *Proc. SPIE 8800, Opto-Acoustic Methods and Applications*, vol. 8800, pp. 88 000G–88 000G–6, 10.1117/12.2031963.

[45] S. A. Telenkov and A. Mandelis, "Fourier-domain biophotoacoustic subsurface depth selective amplitude and phase imaging of turbid phantoms and biological tissue," *J. Biomed. Optics*, vol. 11, no. 4, pp. 044 006–044 006–10, 2006.

[46] S. Telenkov and A. Mandelis, "Signal-to-noise analysis of biomedical photoacoustic measurements in time and frequency domains," *Rev. Sci. Instrum.*, vol. 81, no. 12, p. 124901, 2010.

[47] H. Nan and A. Arbabian, "Stepped-frequency continuous-wave microwave-induced thermoacoustic imaging," *Appl. Phys. Lett.*, vol. 104, no. 22, pp. –, 2014.

[48] C. Lou, L. Nie, and D. Xu, "Effect of excitation pulse width on thermoacoustic signal characteristics and the corresponding algorithm for optimization of imaging resolution," *J. Appl. Phys.*, vol. 110, no. 8, p. 083101, 2011.

[49] M. Xu, G. Ku, and L. V. Wang, "Microwave-induced thermoacoustic tomography using multi-sector scanning," *Med. Phys.*, vol. 28, no. 9, pp. 1958–1963, 2001.

[50] D. R. Bauer, X. Wang, J. Vollin, H. Xin, and R. S. Witte, "Spectroscopic thermoacoustic imaging of water and fat composition," *Appl. Phys. Lett.*, vol. 101, no. 3, pp. 033 705–4, 2012.

[51] C. Lou, S. Yang, Z. Ji, Q. Chen, and D. Xing, "Ultrashort microwave-induced thermoacoustic imaging: A breakthrough in excitation efficiency and spatial resolution," *Phys. Rev. Lett.*, vol. 109, no. 218101, 2012.

[52] A. T. Eckhart, R. T. Balmer, W. A. See, and S. K. Patch, "Ex vivo thermoacoustic imaging over large fields of view with 108 mhz irradiation," *IEEE Trans. Biomed. Eng.*, vol. 58, no. 8, pp. 2238–2246, 2011.

[53] L. Huang, L. Yao, L. Liu, J. Rong, and H. Jiang, "Quantitative thermoacoustic tomography: Recovery of conductivity maps of heterogeneous media," *Appl. Phys. Lett.*, vol. 101, no. 24, p. 244106, 2012.

[54] Z. Zhao, J. Song, X. Zhu, J. Wang, J. Wu, Y. Liu, Z. Nie, and Q. Liu, "System development of microwave induced thermo-acoustic tomography and experiments on breast tumor," *Progress In Electromagnetics Research*, vol. 134, pp. 323–336, 2013.

[55] S. Kellnberger, A. Hajiaboli, G. Sergiadis, D. Razansky, and V. Ntziachristos, "High resolution imaging with impulse based thermoacoustic tomography," in *Proc. SPIE-OSA Biomed. Optics*, ser. Proceedings of SPIE-OSA Biomedical Optics, C. Lin and V. Ntziachristos, Eds., vol. 8089. Optical Society of America, p. 808905.

[56] M. Omar, S. Kellnberger, G. Sergiadis, D. Razansky, and V. Ntziachristos, "Near-field thermoacoustic imaging with transmission line pulsers," *Med. Phys.*, vol. 39, no. 7, pp. 4460–4466, 2012, omar, Murad Kellnberger, Stephan Sergiadis,

George Razansky, Daniel Ntziachristos, Vasilis eng 2012/07/27 06:00 Med Phys. 2012 Jul;39(7):4460-6. doi: 10.1118/1.4729710.

[57] P. Jariyatantiwait, C. F. Bunting, and D. Piao, "An in-silico study of microwave-induced thermo-acoustic tomography: Modulated chirp pulse excitation for peak-power reduction," *Med. Phys.*, sumitted for publication, 2015.

[58] S. Mukherjee, "An in-silico study of thermo-acoustic computed tomography for external and internal imaging geometry," Ph.D. dissertation, Oklahoma State University, Stillwater, Oklahoma, 2013.

[59] J.-M. Jin, *The Finite Element Method in Electromagnetics*, 2nd ed. New York: John Wiley & Sons, Inc., 2002.

[60] A. F. Peterson, S. L. Ray, and R. Mittra, *Computational Methods for Electromagnetics*. Piscataway, NJ: IEEE Press, 1998.

[61] M. Xu and L. V. Wang, "Rf-induced thermoacoustic tomography," in *Engineering in Medicine and Biology, 2002. 24th Annual Conference and the Annual Fall Meeting of the Biomedical Engineering Society EMBS/BMES Conference, 2002. Proceedings of the Second Joint*, vol. 2, pp. 1211–1212 vol.2.

[62] P. Z. Peebles, *Radar Principles*. New York: John Wiley & Sons, Inc., 1998.

APPENDICES

In this numerical study, Matlab® is used for the simulation. The source codes programmed in Matlab® are shown as follows:

A Main Codes for the Simulations

```
%% Start New Simulation --- Clear Everything
close all;                                  % Close all the open figs
clear all;                                  % Clear all variables
clc;                                        % Clear command window
%% Defining Constants
% Fundamental physic constants
ep0  = 8.854e-12;                           % Freespace permittivity (F/m)
mu0  = 4.0e-7*pi;                           % Freespace permeability (H/m)
c0   = 1/sqrt(ep0*mu0);                     % Freespace wave speed (m/s)
% Material properties (non-homo)
SigC1 = 00.100; SigB1 = 00.100; SigH1 = 00.100; SigT1 = 00.300; % concave
EprC1 = 80.000; EprB1 = 80.000; EprH1 = 80.000; EprT1 = 80.000; % concave
SigC2 = 01.216; SigB2 = 01.216; SigH2 = 00.000; SigT2 = 00.608; % convex
EprC2 = 60.500; EprB2 = 60.500; EprH2 = 01.000; EprT2 = 60.500; % convex
% Material properties (homo)
Mur  = 1.00e+0;                             % Relative permeability
Bee  = 4.00e-4;                             % Thermal expansion coeff.
Cpp  = 4.00e+3;                             % Heat capacity
Vss  = 1.50e+3;                             % Acoustic velocity
Rho  = 1.00e+3;                             % Mass density
% Units (for plotting)
unit.l  = {1e-2,'cm'};                      % Unit of length
unit.t  = {1e-6,'\mus'};                    % Unit of time
unit.p  = {1e-6,'\muPa'};                   % Unit of pressure
% Constants for ploting --- Colorbar
RED   = gray(50); RED(:,1)  = 1;            % Red for positive values
BLUE  = gray(50); BLUE(:,3) = 1;            % Blue for negative values
RB    = [BLUE;flipud(RED)];                 % Generate custom colormap
Scale = [-0.5 0.5];                         % Axis scale
%% Loading Mesh and Initializing Domains
% Mesh #4 ------------------------------------------------------------------
[Mesh.node Mesh.edge Mesh.elem] = get_mesh2D('internal_4.mphtxt'); % 0d
Edge.scat = [1 2 9 16];                     % Boundary of scattering
```

```
Edge.bgnd = [3  4  10  15];                    % Boundary of tissue bgnd
Edge.hole = [5  6  11  12];                    % Boundary of hole (rectum)
Edge.tag1 = [7  8  13  14];                    % Boundary of target 1
Elem.coup = 1;                                 % Region of coupling
Elem.bgnd = 2;                                 % Region of background
Elem.hole = 3;                                 % Region of hole (rectum)
Elem.tagA = 4;                                 % Region of target A
%-------------------------------------------------------------------------
% Interpretation of loaded mesh
Nnode = size(Mesh.node,2);                     % Number of nodes
Nedge = size(Mesh.edge,2);                     % Number of edges
Nelem = size(Mesh.elem,2);                     % Number of elements
Rnode = sqrt((Mesh.node(1,:)).^2+...
             (Mesh.node(2,:)).^2);             % Radius of node
Redge = mean([Rnode(Mesh.edge(1,:));
              Rnode(Mesh.edge(2,:))]);         % Radius of edge
Relem = mean([Rnode(Mesh.elem(1,:));
              Rnode(Mesh.elem(2,:));
              Rnode(Mesh.elem(3,:))]);         % Radius of elem
minx = min(Mesh.node(1,:));                    % Minimum of geometry in x
maxx = max(Mesh.node(1,:));                    % Maximum of geometry in x
miny = min(Mesh.node(2,:));                    % Minimum of geometry in y
maxy = max(Mesh.node(2,:));                    % Maximum of geometry in y
lenx = maxx - minx;                            % Length of geometry in x
leny = maxy - miny;                            % Length of geometry in y
px   = 10^-floor(log10(abs(lenx/10)));
py   = 10^-floor(log10(abs(leny/10)));
tickx = (floor(px*minx):round(px*lenx)/6:ceil(px*maxx))/px;
ticky = (floor(py*miny):round(py*leny)/6:ceil(py*maxy))/py;
% Part of Edge
EdgeName = fieldnames(Edge);
for i = 1:length(EdgeName);
    [edge.(EdgeName{i}) ~] = part(Mesh.edge,Edge.(EdgeName{i}));
end
% Part of Elem
ElemName = fieldnames(Elem);
for i = 1:length(ElemName);
    [elem.(ElemName{i}) ~] = part(Mesh.elem,Elem.(ElemName{i}));
end
%% Defining Material Properties for Each Domain
Material.DMN = {'coup','bgnd','hole','tagA','tagB'};
Material.SIG = [ SigC    SigB    SigH    SigT    SigT ];
Material.EPR = [ EprC    EprB    EprH    EprT    EprT ];
Material.MUR = [ Mur     Mur     Mur     Mur     Mur  ];
Material.BEE = [ Bee     Bee     Bee     Bee     Bee  ];
Material.CPP = [ Cpp     Cpp     Cpp     Cpp     Cpp  ];
Material.VSS = [ Vss     Vss     Vss     Vss     Vss  ];
Material.RHO = [ Rho     Rho     Rho     Rho     Rho  ];

epr = zeros(1,Nelem);                          % Initializing epsilon_r
mur = zeros(1,Nelem);                          % Initializing mu_r
sig = zeros(1,Nelem);                          % Initializing sigma
```

```
bee = zeros(1,Nelem);                          % Initializing beta_e
cpp = zeros(1,Nelem);                          % Initializing C_p
vss = zeros(1,Nelem);                          % Initializing v_s
rho = zeros(1,Nelem);                          % Initializing rho

for i = 1:length(ElemName)
    Ei = zeros(size(Mesh.elem(4,:)));          % Clear index
    EN = ElemName{i};                          % Element Name
    for j = Elem.(EN)
        Ei = or(Ei,Mesh.elem(4,:)==j);         % Element index
    end
    Ri = strcmp(Material.DMN,EN);              % Region index
    epr(Ei) = Material.EPR(Ri);
    mur(Ei) = Material.MUR(Ri);
    sig(Ei) = Material.SIG(Ri);
    bee(Ei) = Material.BEE(Ri);
    cpp(Ei) = Material.CPP(Ri);
    vss(Ei) = Material.VSS(Ri);
    rho(Ei) = Material.RHO(Ri);
end
% PML of sig
sig_p = sig;                                   % Sigma for SAR calculation
PML.L = 8;
PML.T = mean(Rnode(1,edge.scat(1,:)))-mean(Rnode(1,edge.bgnd(1,:)));
PML.H = mean(Rnode(1,edge.bgnd(1,:)))+PML.T*(0:PML.L-1)/PML.L;
PML.S = 3.2*((1:PML.L)/PML.L).^2;

for i = 1:PML.L
    sig_coup = Material.SIG(strcmp(Material.DMN,'coup'));
    sig(Relem > PML.H(i)) = sig_coup + PML.S(i);
end
%% Generating Excitation Signal

% Pulse Properties
Signal.freq  = 915.0e+6;                       % Frequency (Hz)
Signal.tr    = 200.00e-6;                      % Repetition period (s)
Signal.rep   = 1;                              % # of repetition
Signal.step  = 5000;                           % # of step for storing
Signal.Gauss = {0.5e-6,1e-6};                  % {FWHM,delay}
Signal.Chirp = {20e3,100e3,Signal.tr/2};       % {fa,fb,tc}
% Discrete time variables
dt   = 1/Signal.freq/10;                       % Stepping time (s)
N    = round(Signal.tr/dt);                    % # Time step for 1 rep
t    = (0:N-1)*dt;                             % Vector of time (s)
% GP, Gaussian Pulse ------------------------------------------------------
FWHM  = Signal.Gauss{1};
delay = Signal.Gauss{2};
std   = FWHM/(2*sqrt(2*log(2)));               % Standard deviation
GP    = exp(-(t-delay).^2/(2*std^2));
% CP, Chirp Pulse ---------------------------------------------------------
fa    = Signal.Chirp{1};
fb    = Signal.Chirp{2};
```

```
tc     = Signal.Chirp{3};
CP     = sin(2*pi*(fa*t+((fb-fa)/(tc)/2)*t.^2));
CP(round(tc/dt):end)=0;
% Modulation of Selected Pulse and Repetition ------------------------------
MPS    = CP.*cos(2*pi*Signal.freq*t);          % Modulated pulse
Signal.output = repmat(MPS,1,Signal.rep);    % repeating by rep
%% Plot Signal and Geomtry
%--------------------------------------------------------------------------
% Figure - Signal
%--------------------------------------------------------------------------
figure(1);
    W = 4;
    H = 4;
    pos = get(gcf, 'Position');
    set(gcf, 'Position', [pos(1) pos(2) W*100 H*100]);
    set(gcf, 'PaperUnits', 'points', 'PaperSize', [W*72,H*72]);
    set(gcf, 'renderer', 'zbuffer'); % comment this line for sharp
    set(gca, 'FontSize', 11, 'LineWidth',1);
    set(gcf, 'color', 'w');

    subplot(211); plot((0:(Signal.rep*N-1))*dt/unit.t{1},PS);
                  xlim([0 Signal.rep*N*dt/unit.t{1}]);
                  xlabel(['t (' unit.t{2} ')']);
                  ylabel('Amplitude');
                  grid on;

    subplot(212); plot((0:(Signal.rep*N-1))*dt/unit.t{1},Signal.output);
                  xlim([0 Signal.rep*N*dt/unit.t{1}]);
                  xlabel(['t (' unit.t{2} ')']);
                  ylabel('Amplitude');
                  grid on;
%--------------------------------------------------------------------------
% Figure - Geometry, Mesh
%--------------------------------------------------------------------------
figure(2);
    W = 2.5;
    H = 2.5;
    pos = get(gcf, 'Position');
    set(gcf, 'Position', [pos(1) pos(2) W*100 H*100]);
    set(gcf, 'PaperUnits', 'points', 'PaperSize', [W*72,H*72]);
    set(gcf, 'renderer', 'zbuffer'); % comment this line for sharp
    set(gca, 'FontSize', 11, 'LineWidth',1);
    set(gcf, 'color', 'w');

        pdesurf(Mesh.node/unit.l{1},Mesh.elem(1:3,:),sig_p);
        hold on;
        sig_bg = Material.SIG(strcmp(Material.DMN,'bgnd'));
        scatter3(Mesh.node(1,edge.detc(1,:))/unit.l{1},...
                 Mesh.node(2,edge.detc(1,:))/unit.l{1},...
                 sig_bg*ones(1,length(edge.detc))','o');
        %scatter3(xs/unit.l{1},ys/unit.l{1},sig_bg,'.');
        hold off;
```

```
        %box on;
        grid on;
        set(gca, 'xtick', tickx/unit.l{1});
        set(gca, 'ytick', ticky/unit.l{1});
        view(2);
        xlim([tickx(1) tickx(end)]);
        ylim([ticky(1) ticky(end)]);
        %axis([tickx(1) tickx(end) ticky(1) ticky(end)]/unit.l{1});
        axis equal tight;
        box on;
figure(3);
    W = 2.5;
    H = 2.5;
    pos = get(gcf, 'Position');
    set(gcf, 'Position', [pos(1) pos(2) W*100 H*100]);
    set(gcf, 'PaperUnits', 'points', 'PaperSize', [W*72,H*72]);
    set(gcf, 'renderer', 'zbuffer'); % comment this line for sharp
    set(gca, 'FontSize', 11, 'LineWidth',1);
    set(gcf, 'color', 'w');

        pdemesh(Mesh.node/unit.l{1},Mesh.edge,Mesh.elem);
        %box on;
        %grid on;
        %title('FEM Mesh');
        set(gca, 'xtick', tickx/unit.l{1});
        set(gca, 'ytick', ticky/unit.l{1});
        %xlabel(['x (' unit.l{2} ')']);
        %ylabel(['y (' unit.l{2} ')']);
        view(2);
        axis equal tight;

%% Generating FEM Matrices for Electric Field
%-----------------------------------------------------------------
% Bayliss-Turkel Radiation Bouondary Condition
R  = max(sqrt(Mesh.node(1,:).^2+Mesh.node(2,:).^2));  % maximum radius
Eb = Material.EPR(strcmp(Material.DMN,'coup')); % EPR scattering boundary
Sb = Material.SIG(strcmp(Material.DMN,'coup')); % SIG scattering boundary
kb = 2*pi*Signal.freq/c0*sqrt(Eb-1i*Sb/(2*pi*Signal.freq)/ep0); % k bnd
alpha = (-1j*kb-(3/(2*R))+(1j*3/(8*kb*R^2)))/(1-(1j/(kb*R)));
beta  = (-(1j/(2*kb*R^2)))/(1-(1j/(kb*R)));
theta = pi/2; % angle of incident uniform plane wave on the boundary
% FEM matrix
M = sparse(Nnode,Nnode);                    % Mass matrix
P = sparse(Nnode,Nnode);                    % Property matrix
S = sparse(Nnode,Nnode);                    % Stiffness matrix
I = sparse(Nnode,Nnode);                    % Boundary matrix
b = sparse(Nnode,1);                        % Load vector (boundary)
f = sparse(Nnode,1);                        % Load vector (internal)
% interior integration + imposing internal source
for i = 1:Nelem
    n = Mesh.elem(1:3,i);                   % node of element i
    x = Mesh.node(1,n);                     % x of each node of element i
```

```
    y = Mesh.node(2,n);                         % y of each node of element i
    A = polyarea(x,y);                          % area of element i (Jacobian)
    b_ = [y(2)-y(3); y(3)-y(1); y(1)-y(2)]/2/A;
    c_ = [x(3)-x(2); x(1)-x(3); x(2)-x(1)]/2/A;
    Me = epr(i)/c0^2*(A/12)*[2 1 1; 1 2 1; 1 1 2];
    Pe = sig(i)*mu0*(A/12)*[2 1 1; 1 2 1; 1 1 2];
    Se = (1/mur(i))*(b_*b_'+c_*c_')*A;
    %fe = A/3*J(i);
    M(n,n) = M(n,n) + Me;
    P(n,n) = P(n,n) + Pe;
    S(n,n) = S(n,n) + Se;
    %f(n)   = f(n)   + fe;
end
% boundary integration + imposing Bayliss-Turkel RBC + boundary source
for i = 1:length(edge.scat)
    n = edge.scat(1:2,i);                       % node of edge i
    x = Mesh.node(1,n);                         % x of each node of edge i
    y = Mesh.node(2,n);                         % y of each node of edge i
    L = norm([diff(x) diff(y)]);                % length of edge i (Jacobian)
    phi = atan3(y,x);                           % angle of each node
        % Orientation of phi (anti-clockwise, increasing order)
        if abs(diff(phi))>pi/2
            [vv,in] = min(phi);
            phi(in) = phi(in)+2*pi;
        end
        phi = sort(phi);
        w = diff(phi);                          % different angle
    R  = sqrt(mean(x)^2+mean(y)^2);             % radius of edge
    I1 = alpha*L/6*[2 1;1 2];
    I2 = beta*L*[1 -1;-1 1];
    b1 = source_term_test1(phi(1),phi(2),kb,theta,beta,alpha,R);
    b2 = source_term_test2(phi(1),phi(2),kb,theta,beta,alpha,R);
    Ie = I1-I2;
    I(n,n) = I(n,n) + Ie;
    b(n) = b(n) + [b1; b2];
end
elem_s = tsearchn(Mesh.node',Mesh.elem(1:3,:)',[xs,ys]);
f(Mesh.elem(1,elem_s)) = 1;
%f = b;
%S = S-I;

%% Generating FEM Matrices for Pressure Field
%-------------------------------------------------------------------------
T   = sparse(Nnode,Nnode);                      % Mass matrix
C   = sparse(Nnode,Nnode);                      % Boundary matrix
K1  = sparse(Nnode,Nnode);                      % Stiffness matrix 1
K2  = sparse(Nnode,Nnode);                      % Stiffness matrix 2
B0  = sparse(Nnode,Nnode);                      % Load matrix without SAR
Bp  = sparse(Nnode,1);                          % Load vector _orig
for i = 1:Nelem;
    n = Mesh.elem(1:3,i);                       % node of element i
    x = Mesh.node(1,n);                         % x of each node of element i
```

```
    y = Mesh.node(2,n);                         % y of each node of element i
    A = polyarea(x,y);                          % area of element i
    b_ = [y(2)-y(3); y(3)-y(1); y(1)-y(2)]/2/A;
    c_ = [x(3)-x(2); x(1)-x(3); x(2)-x(1)]/2/A;
    K1e = (b_*b_'+c_*c_')*A;
    Te = (1/vss(i))^2*(A/12)*[2 1 1; 1 2 1; 1 1 2];
    Bpe = (bee(i)/cpp(i))*(A/12)*([sig_p(n(1))*4;
                                   sig_p(n(2))*4;
                                   sig_p(n(3))*4]);
    B0e = (bee(i)/cpp(i))*(A/12)*[2 1 1; 1 2 1; 1 1 2];
    K1(n,n) = K1(n,n)+ K1e;
    T(n,n)  = T(n,n) + Te;
    B0(n,n) = B0(n,n)+ B0e;
    Bp(n)   = Bp(n)  + Bpe;                     % ignore .. use the above one
end
for i = 1:length(edge.scat)
    n = edge.scat(1:2,i);                       % node of edge i
    x = Mesh.node(1,n);                         % x of each node of edge i
    y = Mesh.node(2,n);                         % y of each node of edge i
    L = norm([diff(x) diff(y)]);                % length of edge i
    R  = sqrt(mean(x)^2+mean(y)^2);             % radius of edge i
    K2e = (1/2/R)*(L/6)*[2 1; 1 2];
    Ce  = (1/mean(vss(n)))*(L/6)*[2 1; 1 2];
    K2(n,n) = K2(n,n) + K2e;
    C(n,n)  = C(n,n) + Ce;
end
K = K1 + K2;

%% Loop of Time Stepping
Pr_a = zeros(length(edge.detc),Signal.step);% Pr at det w/ target
Pr_h = zeros(length(edge.detc),Signal.step);% Pr at det w/o target
Ez0=zeros(Nnode,1);                         % Ez
Ez1=zeros(Nnode,1);                         % Ez'
Ez2=zeros(Nnode,1);                         % Ez''
Pr0=zeros(Nnode,1);                         % Pr
Pr1=zeros(Nnode,1);                         % Pr'
Pr2=zeros(Nnode,1);                         % Pr''
Ph0=zeros(Nnode,1);                         % Pr   no target
Ph1=zeros(Nnode,1);                         % Pr'  no target
Ph2=zeros(Nnode,1);                         % Pr'' no target
sig_pA = sig_p;                             % sigma with target
sig_pH = sig_pA;
TagName = ElemName(strncmp(ElemName,'tag',3));
for i = 1:length(TagName)
    Ei = zeros(size(Mesh.elem(4,:)));       % Clear index
    TN = TagName{i};                        % Target Name
    for j = Elem.(TN)
        Ei = or(Ei,Mesh.elem(4,:)==j);      % Element Index
    end
    Ri = strncmp(Material.DMN,'tag',3);     % Region Index
    sig_pH(Ei) = Material.SIG(strcmp(Material.DMN,'bgnd'));
end
```

```
sig_pnA = pdeprtni(Mesh.node,Mesh.elem(1:3,:),sig_pA);
sig_pnH = pdeprtni(Mesh.node,Mesh.elem(1:3,:),sig_pH);
figure('units','normalized','outerposition',[0 0 1 1]);
set(gcf, 'renderer', 'zbuffer');
in_step = Signal.rep*N/Signal.step;          % Interval step
id = 1:length(edge.detc);
for i=1:Signal.step
    for n=1:in_step
    m = (i-1)*in_step+n                      % Show calculating step
    sn = Signal.output(m);
    %-------------------------------------------------------------------
    [Ez0 Ez1 Ez2] = Newmark1(M,P,S,f,sn,dt,0.25,0.5,Ez0,Ez1,Ez2);
              B1 = B0*(sig_pnA.*abs(Ez0).^2);
    [Pr0 Pr1 Pr2] = Newmark2(T,C,K,B1,1,0.5,dt,0.25,0.5,Pr0,Pr1,Pr2);
              B2 = B0*(sig_pnH.*abs(Ez0).^2);
    [Ph0 Ph1 Ph2] = Newmark3(T,C,K,B2,1,0.5,dt,0.25,0.5,Ph0,Ph1,Ph2);
    %-------------------------------------------------------------------
    Pr_a(id,i)    = Pr0(edge.detc(1,id)); % get Pr0 at detector node
    Pr_h(id,i)    = Ph0(edge.detc(1,id)); % get Ph0 at detector node
    end
end
%% Saving Raw Results
DT = datestr(now,'yy-mm-dd-HH-MM'); % String of date and time
save(['EXP-',DT,'.mat'],'Mesh','Edge','Elem','xs','ys',...
      'Material','Signal','Pr_a','Pr_h','unit');
%% Post Processing
% Extract variables
ep0  = 8.854e-12;                            % Freespace permittivity (F/m)
mu0  = 4.0e-7*pi;                            % Freespace permeability (H/m)
c0   = 1/sqrt(ep0*mu0);                      % Freespace Wave speed (m/s)
dt   = 1/Signal.freq/10;                     % Time step (s)

N    = round(Signal.tr/dt);                  % # time step for 1 rep
t    = (0:N-1)*dt;                           % Vector of time (s)
in_step = Signal.rep*N/Signal.step;          % Number of interval steps

% Different Pressure
Pr   = Pr_a - Pr_h;                          % Pressure at transducer

% Edge Part
EdgeName = fieldnames(Edge);
for i = 1:length(EdgeName);
    [edge.(EdgeName{i}) ~] = part(Mesh.edge,Edge.(EdgeName{i}));
end

% Elem Part
ElemName = fieldnames(Elem);
for i = 1:length(ElemName);
    [elem.(ElemName{i}) ~] = part(Mesh.elem,Elem.(ElemName{i}));
end

minx = min(Mesh.node(1,:));                  % Minimum of geometry in x
```

```
maxx = max(Mesh.node(1,:));                    % Maximum of geometry in x
miny = min(Mesh.node(2,:));                    % Minimum of geometry in y
maxy = max(Mesh.node(2,:));                    % Maximum of geometry in y
lenx = maxx - minx;                            % Length of geometry in x
leny = maxy - miny;                            % Length of geometry in y
px   = 10^-floor(log10(abs(lenx/10)));
py   = 10^-floor(log10(abs(leny/10)));
tickx = (floor(px*minx):round(px*lenx)/6:ceil(px*maxx))/px;
ticky = (floor(py*miny):round(py*leny)/6:ceil(py*maxy))/py;
%-------------------------------------------------------------------------
% Noise and Filter
%-------------------------------------------------------------------------
SNRdB = 10;
Ppr  = zeros(1,length(edge.detc));
Pr_n = zeros(size(Pr));
Pr_tn = zeros(size(Pr)); % pressure received by transducer
for i = 1:length(edge.detc)
    Ppr(i) = mean(Pr(i,:).^2);       % Power of Pressure at each sensor
    Pr_n(i,1:Signal.step) = Pr(i,1:Signal.step)+...
                    wgn(1,Signal.step,10*log10(Ppr(i)/(10^(SNRdB/10))));
    % [bb,aa] = butter(2, 2*pi*[Signal.fa Signal.fb]*dt, 'bandpass');
    [bb,aa] = butter(2, 2*pi*[20e3 2000e3]*in_step*dt, 'bandpass');
    Pr_tn(i,1:Signal.step) = filter(bb,aa,(Pr_n(i,1:Signal.step)));
end
%-------------------------------------------------------------------------
% Select detectors at any angle for showing pressure
%-------------------------------------------------------------------------
%angle_pick=[90 45 0 -45 -90];
angle_pick=[90];
%angle_pick=[0 90 180 -90];
ed_pick = zeros(1,length(angle_pick));
ed_angle= zeros(1,length(edge.detc));

% Finding angle at each Detector
for i = 1:length(edge.detc)
    ed_angle(i)=atan2(Mesh.node(2,edge.detc(1,i)),...
                    Mesh.node(1,edge.detc(1,i)))*180/pi;
end

% Selecting Detector that close to the angle_pick
for i = 1:length(angle_pick)
    [val ed_pick(i)]=min(abs(ed_angle-angle_pick(i)));
end
%-------------------------------------------------------------------------
% Figure - Geometry and selected detectors for plotting pressure
%-------------------------------------------------------------------------
figure(5);
    W = 2.5;
    H = 2.5;
    pos = get(gcf, 'Position');
    set(gcf, 'Position', [pos(1) pos(2) W*100 H*100]);
    set(gcf, 'PaperUnits', 'points', 'PaperSize', [W*72,H*72]);
```

```
    set(gcf, 'renderer', 'zbuffer'); % comment this line for sharp
    set(gca, 'FontSize', 11, 'LineWidth',1);
    set(gcf, 'color', 'w');

    pdemesh(Mesh.node/unit.l{1},Mesh.edge,[]);
    set(gca, 'xtick', tickx/unit.l{1});
    set(gca, 'ytick', ticky/unit.l{1});
    %xlabel(['x (' unit.l{2} ')']);
    %ylabel(['y (' unit.l{2} ')']);
    view(2);
    axis equal tight;
%-------------------------------------------------------------------------
% Figure - Excitation Electrical Signal and Pressure Induce Output
%-------------------------------------------------------------------------
figure(6);
    W = 5.5;
    H = 1.5;
    pos = get(gcf, 'Position');
    set(gcf, 'Position', [pos(1) pos(2) W*100 H*100]);
    set(gcf, 'PaperUnits', 'points', 'PaperSize', [W*72,H*72]);
    %set(gcf, 'renderer', 'zbuffer'); % comment this line for sharp
    set(gca, 'FontSize', 11, 'LineWidth',1);
    set(gcf, 'color', 'w');
        po = floor(log10((max(max(Pr_tn(:,:))))));
        plot((0:(Signal.step-1))*in_step*dt/unit.t{1},...
            Pr_tn(ed_pick,:)*10^-po);
        xlabel(['t (' unit.t{2} ')']);
        ylabel('Pressure (a.u.)');
        %xlim([0 60]);
        set(gca, 'xtick', 0:20:round(Signal.rep*N*dt/1e-6)); grid on;
        box on; grid on;
        %legend('A','B','C','D');
%-------------------------------------------------------------------------
% Calculating and Plotting cross correlation
%-------------------------------------------------------------------------
Pr_peak = zeros(length(edge.detc),2);
flipmatched = zeros(length(edge.detc),Signal.step);

envelope = abs(hilbert(Signal.output));
envelope = envelope(1:in_step:Signal.rep*N);
envelope_f = filter(bb,aa,(envelope(1:Signal.step)));
%ref = CP(1:2:end);
ref = envelope;

for i = 1:length(edge.detc)
    det_node = i;
    received = Pr_tn(i,1:Signal.step);
    matched  = xcorr(ref,received);
    flipmatched(i,:) = fliplr(matched(1:(length(matched)+1)/2));
    [val pos] = max(flipmatched(i,:));
    Pr_peak(i,1)=val;
    Pr_peak(i,2)=pos*dt;
```

```
end
%-------------------------------------------------------------------------
% Figure - Cross-Correlation Detection Output
%-------------------------------------------------------------------------
figure(7);
    W = 5.5;
    H = 1.5;
    pos = get(gcf, 'Position');
    set(gcf, 'Position', [pos(1) pos(2) W*100 H*100]);
    set(gcf, 'PaperUnits', 'points', 'PaperSize', [W*72,H*72]);
    %set(gcf, 'renderer', 'zbuffer'); % comment this line for sharp
    set(gca, 'FontSize', 11, 'LineWidth',1);
    set(gcf, 'color', 'w');
        fo = floor(log10((max(max(flipmatched(:,:))))));
        plot((0:(Signal.step-1))*in_step*dt/unit.t{1},...
            flipmatched(ed_pick,:)*10^-fo);
        xlabel(['t (' unit.t{2} ')']);
        ylabel('Correlated (a.u.)');
        %xlim([0 60]);
        set(gca, 'xtick', 0:20:round(Signal.rep*N*dt/1e-6)); grid on;
        box on; grid on;
        %legend('A','B','C','D');
% -------------------------------------------------------------------------
% Image Reconstruction
% -------------------------------------------------------------------------
dtr = in_step*dt;
%scope = [minx maxx miny maxy];
scope = [-0.04 0.04 -0.04 0.04];

DetcCoord = Mesh.node(:,edge.detc(1,:));

%[irec xx yy]= bp(Pr,dtr,DetcCoord,scope,4300,0.5e-6);
%[irec xx yy]= bp(diff(Pr,1,2),dtr,DetcCoord,scope,4300,0.5e-6);

%[irec xx yy]= bp(Pr_t,dtr,DetcCoord,scope,4300,0.5e-6);
%[irec xx yy]= bp(diff(Pr_t,1,2),dtr,DetcCoord,scope,4300,0.5e-6);

%[irec xx yy]= bp(Pr_tn,dtr,DetcCoord,scope,4300,0.5e-6);
%[irecd xx yy]= bp(diff(Pr_tn,1,2),dtr,DetcCoord,scope,4300,0.5e-6);

[irec xx yy]= bp(flipmatched,dtr,DetcCoord,scope,4300,0e-6);
[irecd xx yy]= bp(diff(flipmatched,1,2),dtr,DetcCoord,scope,4300,0e-6);
%-------------------------------------------------------------------------
% Figure - Reconstructed Image
%-------------------------------------------------------------------------
figure(8);
    W = 2.5;
    H = 2.5;
    pos = get(gcf, 'Position');
    set(gcf, 'Position', [pos(1) pos(2) W*100 H*100]);
    set(gcf, 'PaperUnits', 'points', 'PaperSize', [W*72,H*72]);
    set(gcf, 'renderer', 'zbuffer'); % comment this line for sharp
```

```
    set(gca, 'FontSize', 11, 'LineWidth',1);
    set(gcf, 'color', 'w');

    surf(xx/unit.l{1},yy/unit.l{1},irec/max(max(abs(irec))),...
        'EdgeColor','none');
    colormap gray;
    shading interp;
    box on;
    grid on;
    %title(' ');
    set(gca, 'xtick', tickx/unit.l{1});
    set(gca, 'ytick', ticky/unit.l{1});
    %xlabel(['x (' unit.l{2} ')']);
    %ylabel(['y (' unit.l{2} ')']);
    view(2);
    axis equal tight;
%-------------------------------------------------------------------------
% Figure - Reconstructed Image
%-------------------------------------------------------------------------
figure(9);
    W = 2.5;
    H = 2.5;
    pos = get(gcf, 'Position');
    set(gcf, 'Position', [pos(1) pos(2) W*100 H*100]);
    set(gcf, 'PaperUnits', 'points', 'PaperSize', [W*72,H*72]);
    set(gcf, 'renderer', 'zbuffer'); % comment this line for sharp
    set(gca, 'FontSize', 11, 'LineWidth',1);
    set(gcf, 'color', 'w');

    surf(xx/unit.l{1},yy/unit.l{1},irecd/max(max(abs(irecd))),...
        'EdgeColor','none');
    colormap gray;
    shading interp;
    box on;
    grid on;
    %title(' ');
    set(gca, 'xtick', tickx/unit.l{1});
    set(gca, 'ytick', ticky/unit.l{1});
    %xlabel(['x (' unit.l{2} ')']);
    %ylabel(['y (' unit.l{2} ')']);
    view(2);
    axis equal tight;

%-------------------------------------------------------------------------
% Calculating Power and Energy
%-------------------------------------------------------------------------

Power  = mean(Pr_tn(1:Signal.step).^2)
Energy = Signal.tr*Power
```

B Subroutine for Importing FEM Mesh

```
function [node, edge, elem]=get_mesh2D(filename)
fid=fopen(filename);
    %-------------------------------------------------------------------------
    % get node
    %-------------------------------------------------------------------------
    start='# Mesh point coordinates';
    finish='';
    node=[];
    sta=0;%status flag
    i=1;
    while(not(feof(fid)))
        if sta==0
            line=fgetl(fid);
            if isequal(start,line)
                sta=1;
            end
        elseif sta==1
            line=fgetl(fid);
            if isequal(finish,line)
                sta=2;
            else
                node(:,i)=str2num(line);
                i=i+1;
            end
        elseif sta==2
            break;
        end
    end
    %-------------------------------------------------------------------------
    % get edge
    %-------------------------------------------------------------------------
    start1='2 # number of nodes per element';
    start2='# Elements';
    finish='';
    data1=[];
    i=1;
    status = 0;
    while(not(feof(fid)))
        if status == 0
            tline = fgetl(fid);
            if isequal(start1,tline)
                status = 1;
            end
        elseif status == 1
            tline = fgetl(fid);
            if isequal(start2,tline)
                status = 2;
            end
        elseif status == 2
            tline = fgetl(fid);
```

```
        if isequal(finish,tline)
            status = 3;
        else
            data1(:,i)=str2num(tline)+1;
            i=i+1;
        end
    elseif status == 3
        break;
    end
end
%-------------------------------------------------------------------------
% get edge sub-domain region
%-------------------------------------------------------------------------
start1=[num2str(i-1) ' # number of geometric entity indices'];
start2='# Geometric entity indices';
finish='';
data2=[];
i=1;
status = 0;
while(not(feof(fid)))
    if status == 0
        tline = fgetl(fid);
        if isequal(start1,tline)
            status = 1;
        end
    elseif status == 1
        tline = fgetl(fid);
        if isequal(start2,tline)
            status = 2;
        end
    elseif status == 2
        tline = fgetl(fid);
        if isequal(finish,tline)
            status = 3;
        else
            data2(:,i)=str2num(tline)+1;
            i=i+1;
        end
    elseif status == 3
        break;
    end
end
edge = [data1;data2];
%-------------------------------------------------------------------------
% get element
%-------------------------------------------------------------------------
start1='3 # number of nodes per element';
start2='# Elements';
finish='';
data3=[];
i=1;
status = 0;
```

```
while(not(feof(fid)))
    if status == 0
        tline = fgetl(fid);
        if isequal(start1,tline)
            status = 1;
        end
    elseif status == 1
        tline = fgetl(fid);
        if isequal(start2,tline)
            status = 2;
        end
    elseif status == 2
        tline = fgetl(fid);
        if isequal(finish,tline)
            status = 3;
        else
            data3(:,i)=str2num(tline)+1;
            i=i+1;
        end
    elseif status == 3
        break;
    end
end
%-------------------------------------------------------------------------
% get element sub-domain region
%-------------------------------------------------------------------------
start1=[num2str(i-1) ' # number of geometric entity indices'];
start2='# Geometric entity indices';
finish='';
data4=[];
i=1;
status = 0;
while(not(feof(fid)))
    if status == 0
        tline = fgetl(fid);
        if isequal(start1,tline)
            status = 1;
        end
    elseif status == 1
        tline = fgetl(fid);
        if isequal(start2,tline)
            status = 2;
        end
    elseif status == 2
        tline = fgetl(fid);
        if isequal(finish,tline)
            status = 3;
        else
            data4(:,i)=str2num(tline);
            i=i+1;
        end
    elseif status == 3
```

```
            break;
        end
    end
    elem = [data3;data4];
fclose(fid);
```

C Subroutine for Newmark Algorithm

```
function [u0_ u1_ u2_] = Newmark(A,B,C,Ds,dt,beta,gamma,u0,u1,u2)
    m1 = (1/beta/dt/dt)*A + (gamma/beta/dt)*B + beta*C;
    m2 = (1/beta/dt/dt)*u0 + (1/beta/dt)*u1 + (1/2/beta-1)*u2;
    m3 = (gamma/beta/dt)*u0 + (gamma/beta-1)*u1 + (gamma/2/beta-1)*dt*u2;
    D_ = Ds;
    u0_ = m1\(A*m2 + B*m3 + D_);
    u2_ = (1/beta/dt/dt)*(u0_-u0)-(1/beta/dt)*u1-((1/2/beta)-1)*u2;
    u1_ = u1 + (1-gamma)*dt*u2 + gamma*dt*u2_;
end
```

D Subroutine for Back-projection Algorithm

```
function [I,X,Y]=bp(P,dt,S,Iw,res,sync)
    Np = size(P,2);                         % size of pressure
    Ns = size(S,2);                         % Number of sensor
    Lx = Iw(2)-Iw(1);
    Ly = Iw(4)-Iw(3);
    Nx = round(Lx*res);
    Ny = round(Ly*res);
    I  = zeros(Ny,Nx);                      % Image
    X  = zeros(Ny,Nx);
    Y  = zeros(Ny,Nx);
    for i = 1:Nx
        x = Iw(1)+Lx*(i-1)/(Nx-1);
        for j = 1:Ny
            y = Iw(3)+Ly*(j-1)/(Ny-1);
            for k = 1:Ns
                dxy2S = sqrt((S(1,k)-x)^2+(S(2,k)-y)^2);
                Nxy2S = ceil(dxy2S/1500/dt)+round(sync/dt);
                X(j,i) = x;
                Y(j,i) = y;
                I(j,i) = I(j,i)+P(k,Nxy2S);
                if sqrt(x^2+y^2)>0.04
                    I(j,i) = nan;
                end
            end
        end
    end
end
```

VITA

Ponlakit Jariyatantiwait

Candidate for the Degree of

Doctor of Philosophy

Thesis: A COMPUTATIONAL STUDY OF MICROWAVE-INDUCED THERMO-ACOUSTIC TOMOGRAPHY BY TIME-DOMAIN FINITE ELEMENT METHOD

Major Field: Electrical Engineering

Biographical:

Education:

Completed the requirements for the degree of Doctor of Philosophy with a major in Electrical Engineering, Oklahoma State University in July, 2015.

Received the Master of Engineering in Electrical Engineering at King Mongkut University of Technology Thonburi, Bangkok, Thailand in 2000.

Received the Bachelor of Engineering in Telecommunication Engineering at King Mongkut Institute of Technology Ladkrabang, Bangkok, Thailand in 1998.

Experience:

Lecturer at the faculty of Engineering, Rajamangala University of Technology Phra-Nakhon, Bangkok, Thailand, 2002 - present.

Electronic Officer at the Signal Battalion, Directorate of Joint Communication, Royal Thai Armed Forces Headquarters, Bangkok, Thailand, 2000 - 2002.